

Mediterranean tephrostratigraphy and peri-Tyrrhenian explosive activity reevaluated in light of the 430-365 kyr record from Fucino Basin (central Italy)

Lorenzo Monaco^a, Danilo M. Palladino^a, Mario Gaeta^a, Fabrizio Marra^b, Gianluca Sottili^a, Niklas Leicher^c, Giorgio Mannella^d, Sébastien Nomade^e, Alison Pereira^f, Eleonora Regattieri^g, Bernd Wagner^c, Giovanni Zanchetta^{d,b,l}, Paul G. Albert^h, Ilenia Arienzoⁱ, Massimo D'Antonio^j, Paola Petrosino^j, Christina J. Manning^k, Biagio Giaccio^{l,*}

a Dipartimento di Scienze della Terra, Sapienza-Università di Roma, Rome, Italy

b Istituto Nazionale di Geofisica e Vulcanologia, Rome, Italy

c Institute of Geology and Mineralogy, University of Cologne, Cologne, Germany

d Dipartimento di Scienze della Terra, University of Pisa, Pisa, Italy

e Laboratoire de Sciences du Climat et de l'Environnement, UMR 8212, CEA-UVSQ, IPSL and Université de Paris-Saclay, Gif-sur-Yvette, France

f Université Paris-Saclay, CNRS, UMR 8148 GEOPS, Orsay, 91405, France

g Istituto di Geoscienze e Georisorse, IGG-CNR, Pisa, Italy

h Department of Geography, Swansea University, College of Science, Swansea, UK

i Istituto Nazionale di Geofisica e Vulcanologia, Osservatorio Vesuviano, Naples, Italy

j Dipartimento di Scienze della Terra, dell'Ambiente e delle Risorse, Università degli Studi di Napoli Federico II, Naples, Italy

k Department of Earth Sciences, Royal Holloway, University of London, Egham, Surrey, UK

l Istituto di Geologia Ambientale e Geoingegneria, IGAG-CNR, Rome, Italy

* Corresponding author: biagio.giaccio@cnr.it

ABSTRACT

Accurately reconstructing the scale and timing of dynamic processes, such as the Middle-Late Pleistocene explosive volcanism and rapid climatic change, must be underpinned by rigorous and independent chronological constraints. In this framework, the study of distal volcanic ash layers, or tephra, transported and deposited over wide regions during explosive volcanic eruptions, is increasingly being recognised as a fundamental chronostratigraphic tool for addressing these challenging issues. Here we present high-resolution distal tephra record preserved in the lacustrine sedimentary succession of the Fucino Basin, central Italy. The investigated record spans the 430-365 ka time interval, corresponding to the full Marine Isotope Stage 11 (MIS 11), and provides outstanding insights into peri-Tyrrhenian potassic explosive volcanism from sources located in central Italy against a backdrop of Mediterranean palaeoclimate records. The succession of ash fall events of this time interval are reconstructed through a detailed lithostratigraphic, geochemical and $^{40}\text{Ar}/^{39}\text{Ar}$ geochronological characterization of the deposits preserved as discrete layers in the Fucino F4-F5 sediment core. This work is complemented by similarly detailed characterization of selected proximal pyroclastic units from the peri-Tyrrhenian potassic volcanoes. Geochemical fingerprinting of the tephra deposits by means of their major, minor, trace elements and Sr isotope compositions indicates that all of the thirty-two investigated ash layers derived from the peri-Tyrrhenian potassic volcanoes. The stratigraphically continuous succession of the Fucino tephra layers allowed the development of a fully independent, $^{40}\text{Ar}/^{39}\text{Ar}$ age-constrained, Bayesian age-depth model for the investigated time interval. Importantly the age-model allows us to establish modelled ages for the within the succession that are not directly dated. The resulting dated tephra record clearly reveals a highly time resolved and previously unparalleled chronicle of explosive activity from the Vulsini, Vico, Sabatini, Colli Albani and Roccamonfina volcanic complexes. Our study provides a benchmark and valuable geochemical and geochronological dataset to be used as a reference for any future development and application of the tephrostratigraphic methods across the central Mediterranean area both during the investigated 430-365 kyr time interval, and deeper in time. This contribution underlines the importance of

51 integrating proximal and distal sedimentary records to more accurately establish long-term and comprehensive
52 volcanic eruption records.

54 1. Introduction

55 Reconstructing the history of explosive volcanism, including the dynamics, timing and recurrence intervals of
56 eruptions, is a fundamental requirement for understanding the temporal evolution of the volcanic systems and
57 for assessing the related hazards (e.g., [Gehrels et al., 2006](#)). The required stratigraphic, chronological and
58 volcanological data are commonly acquired in near-vent (proximal) volcanic areas, where the geological record
59 provides key data for evaluating eruptive and emplacement dynamics, as well as the evolution of the volcanic
60 edifices. Furthermore, the presence of coarse-grained K-rich crystals in proximal deposits from volcanoes fed
61 by highly potassic evolved magmas enables direct and precise radiometric dating using the $^{40}\text{Ar}/^{39}\text{Ar}$
62 technique. However, due to the intense volcano-tectonic and sedimentary processes occurring in near-source
63 volcanic regions, many proximal eruption deposits are often buried, inaccessible, or partially eroded. In
64 contrast, intermediate and distal archives, located usually downwind with respect to volcanic sources, can offer
65 a more continuous record of volcanic ash layers (or “tephra”) derived from explosive eruption columns and co-
66 ignimbrite ash clouds, thus enabling the reconstruction of the eruptive history and dynamics of individual
67 volcanic systems and regions (e.g., [Paterne et al., 1986, 1988](#); [Newnham et al., 1999](#); [de Fontaine et al., 2007](#);
68 [Dugmore et al., 2013](#); [Giaccio et al., 2014](#); [Leicher et al., 2016, 2019](#); [Albert et al., 2018, 2019](#); [Larsen et al.,](#)
69 [2020](#); [Wulf et al., 2020](#)).

70 The relevance of tephrostratigraphy extends beyond solely volcanological applications, as these
71 instantaneously deposited layers are also outstanding chronological, stratigraphic and correlation tools for
72 addressing numerous issues in Quaternary sciences (e.g., [Lowe et al., 2011](#)). Through diagnostic
73 geochemical, stratigraphic and chronological features, the volcanic ash, widely dispersed during explosive
74 eruptions and deposited on regional to global scale ([Ponomareva et al., 2015](#)), can be recognized and
75 correlated to eruptive events or distal tephra of known ages. This provides an effective and reliable way through
76 which sedimentary archives with co-located tephra can be accurately and precisely dated and correlated over
77 wide regions. Indeed, when combined with high-precision and accurate radiometric $^{40}\text{Ar}/^{39}\text{Ar}$ dating and
78 detailed multiproxy series, long and continuous distal tephra successions become the cornerstones for
79 reconstructing both the paleoclimatic change and the history of explosive volcanism (e.g., [Thorarinsson, 1981a,](#)
80 [b](#); [Paterne, 1986, 1988](#); [Dugmore, 1989](#); [Narcisi and Vezzoli, 1999](#); [Wastergard, 2002](#); [Wulf et al., 2004, 2008,](#)
81 [2012](#); [Lane et al., 2013](#); [Giaccio et al., 2015a](#); [Kousis et al., 2018](#); [Leicher et al., 2019](#); [Mannella et al., 2019](#);
82 [Regattieri et al., 2019](#)).

83 Tephrostratigraphy is most successfully applied when long and continuous sedimentary successions
84 containing well-preserved tephra layers are located in a suitable range of distance from sources of recurrent
85 explosive activity. These requirements are fulfilled in the Mediterranean area, particularly in central-southern
86 Italy. Indeed, the recurrent and continuous explosive activity of the peri-Tyrrhenian volcanism, fed by potassic
87 to ultrapotassic magmas (e.g., [Peccerillo, 2017](#)), as well as the presence of numerous Quaternary tectonic
88 basins hosting thick sedimentary successions, constitute a unique combination which has allowed the retrieval
89 of extremely rich tephra repositories and, consequently, eruption event stratigraphies. An increasing number
90 of studies on marine ([Keller et al., 1978](#); [Paterne et al., 2008](#); [Bourne et al., 2010, 2015](#); [Tamburrino et al.,](#)
91 [2012](#); [Insigna et al., 2014](#); [Morabito et al., 2014](#); [Matthews et al., 2015](#); [Petrosino et al., 2015, 2016](#); [D'Antonio](#)

92 et al., 2016), lacustrine (Wulf et al., 2008; Petrosino et al., 2014a; Giaccio et al., 2015a; Di Roberto et al., 2018;
93 Leicher et al., 2019; Regattieri et al., 2019) and sub-aerial (Giaccio et al., 2012a; Gatta et al., 2016; Donato et
94 al., 2016; Zanchetta et al., 2018; Bini et al., 2020) sedimentary environments of the Mediterranean region have
95 documented this potential. However, despite these recent advances, the teprostratigraphic framework of the
96 central Mediterranean area is still fragmentary and unexplored, especially for the Middle Pleistocene (~780-
97 130 ka).

98
10
11
12
13
14
15
16
17
18
19
20
21
22
23
24
25
26
27
28
29
30
31
32
33
34
35
36
37
38
39
40
41
42
43
44
45
46
47
48
49
50
51
52
53
54
55
56
57
58
59
60
61
62
63
64
65

1
2
3
4
5
6
7
8
9
10
11
12
13
14
15
16
17
18
19
20
21
22
23
24
25
26
27
28
29
30
31
32
33
34
35
36
37
38
39
40
41
42
43
44
45
46
47
48
49
50
51
52
53
54
55
56
57
58
59
60
61
62
63
64
65



Figure 1. Reference maps. **a)** The Fucino Basin and the peri-Tyrrhenian potassic volcanoes in the context of the Mediterranean Quaternary volcanism and the Middle Pleistocene tephrostratigraphic records (blue dots) cited in the text. **b)** Magnification of the area highlighted in **a)** showing in detail the location of Fucino Basin relative to the peri-Tyrrhenian potassic volcanic systems of central-southern Italy. **c)** DEM map of Fucino Basin highlighting the location of the F4-F5 core, along with other cores from this lacustrine basin.

105 Among the lacustrine successions hosted in the Pliocene-Quaternary inter-mountain tectonic basins of the
106 central-southern Apennines (Italy), Fucino's is the most continuous and temporally resolved, with ~900 m of
107 seemingly uninterrupted sedimentary infill, documenting the sediment accumulation since the Lower
108 Pleistocene up to historical times (Cavinato et al., et al., 2002; Giaccio et al., 2015b) and a rich tephra record
109 (Giaccio et al., 2017, 2019; Di Roberto et al., 2018; Mannella et al., 2019; Del Carlo et al., 2020). Three factors
110 make the Fucino Basin unique for reconstructing the eruptive history of the Italian peri-Tyrrhenian potassic to
111 ultra-potassic volcanic activity and improving the central Mediterranean Middle Pleistocene tephrostratigraphic
112 framework: (i) its relatively short distance from the peri-Tyrrhenian volcanoes of central Italy (~70 to ~150 km,
113 Fig. 1a); (ii) its downwind location with respect to these volcanoes, i.e., along the preferential ash dispersal
114 axes (Fig. 1b); (iii) the occurrence of crystals of K-rich minerals, which facilitates laser fusion single crystals
115 $^{40}\text{Ar}/^{39}\text{Ar}$ dating approach.

116 Recently, Giaccio et al. (2019) reported the presence of ~130 volcanic ash layers in a composite ~98 m-long
117 sediment core (F4-F5) from Fucino Basin spanning the last 430 kyr (Fig. 2) confirming the great potential of
118 this succession to become one of the cornerstones in the tephrostratigraphic network of the entire
119 Mediterranean region. However, so far, less than a quarter of these ~130 tephra layers have been
120 stratigraphically, geochemically and chronologically characterized (Giaccio et al., 2017; 2019). In this paper,
121 we present a detailed lithostratigraphic, geochemical and chronological data for the lowermost 28 tephra
122 layers from the F4-F5 core, along with proximal deposits from 5 selected volcanic units of the peri-Tyrrhenian
123 volcanoes, all constrained within the Marine Isotope Stage (MIS) 11 period (i.e., ~430-365 ka). The MIS 11
124 period is particularly relevant in terms of both volcanological and tephrochronological investigations, as it
125 marks the onset of the Vico volcano activity (e.g., Perini et al., 2004; Pereira et al., 2020), thus adding a further
126 volcanic source to the already rich central Mediterranean Middle Pleistocene tephrostratigraphic framework
127 (Fig. 3). Furthermore, currently only few tephrostratigraphic records spanning the MIS 11 period in the
128 Mediterranean region have been investigated (Leicher et al., 2019; Vakhrameeva et al., 2018; 2021; Fig. 1a).
129 The results of this study are discussed in the general context of the Middle Pleistocene Mediterranean
130 tephrostratigraphy and of the central Italy peri-Tyrrhenian explosive volcanism, providing a major contribution
131 towards improved framework of the regional to extra-regional tephrochronology and of the explosive volcanism
132 history. They also provide the basis for developing a robust and independent age-model for the multi-proxy
133 paleoclimate information of the Fucino succession during MIS 11, a key period in the Late Quaternary climatic
134 history, whose analogies with the Holocene have long been debated (e.g., McManus et al., 2003; Tzedakis,
135 2010).

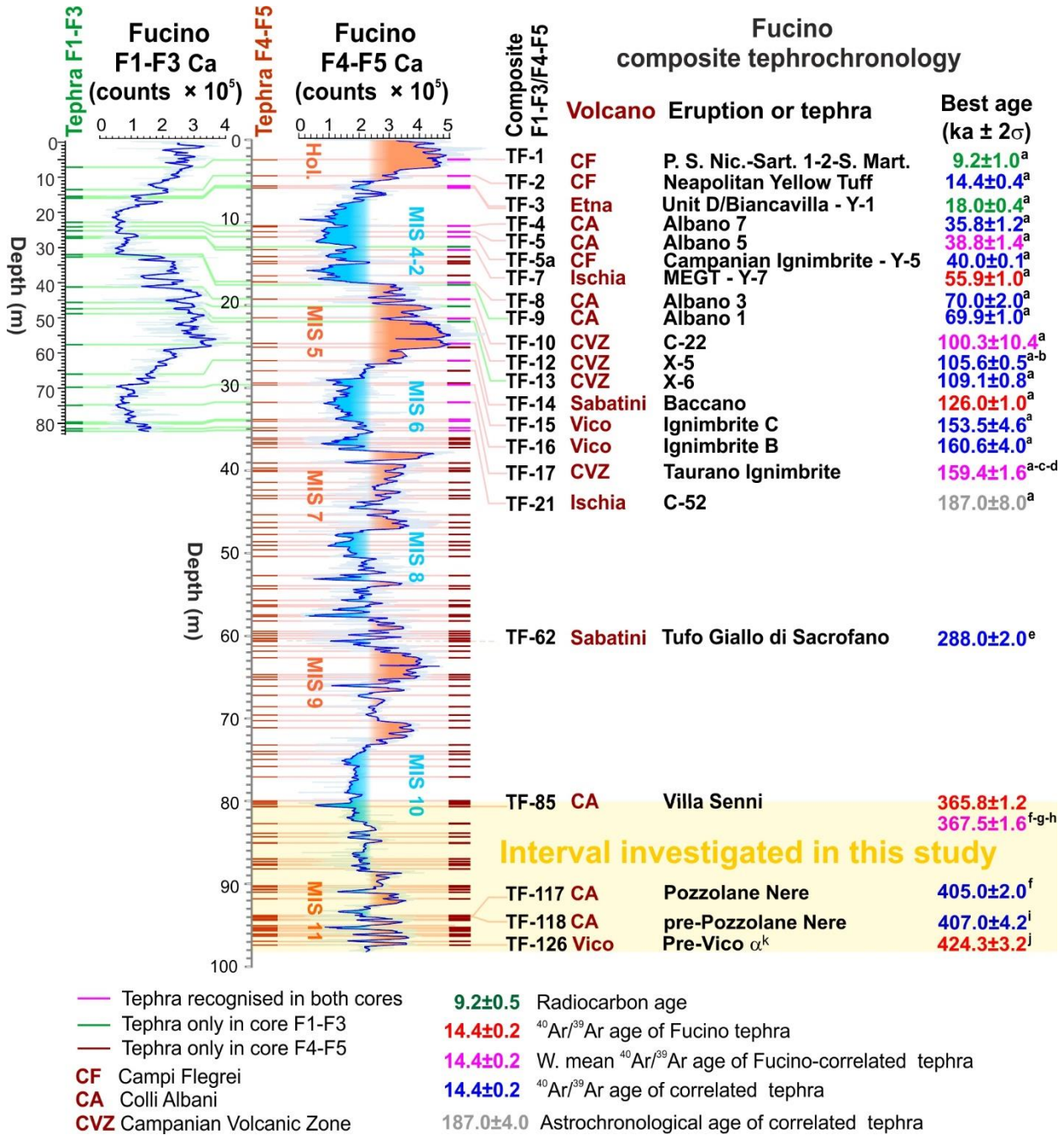


Figure 2. Stratigraphic interval of the F4-F5 Fucino Basin sediment core investigated in this study (modified from [Giaccio et al., 2019](#)). ⁴⁰Ar/³⁹Ar ages are recalculated relatively to an age of 1.1891 Ma for the Alder Creek sanidine monitor standard ([Niespolo et al., 2017](#)), with the uncertainty expressed at 2σ. ⁴⁰Ar/³⁹Ar ages data source: ^a [Mannella et al. \(2019 and references therein\)](#); ^b [Petrosino et al. \(2016\)](#); ^c [Amato et al. \(2018\)](#); ^d [De Vivo et al. \(2001\)](#); ^e [Sottili et al. \(2010\)](#); ^f [Marra et al. \(2009\)](#); ^g [Marra et al. \(2019\)](#); ^h [Giaccio et al. \(2012a, 2012b\)](#); ⁱ [Pereira et al. \(2018\)](#); ^j [Giaccio et al. \(2019\)](#).

2. Geological and volcanological setting

2.1. The Fucino Basin

The Fucino Basin (42° 00' 00" N; 013° 30' 00" E) is one of the larger inter-Apennine tectonic basins that developed during the extensional phase related to the geodynamic evolution of the Tyrrhenian Basin and central-southern Apennine chain (e.g., [Doglioni et al., 1996](#)). Extensional tectonics, mainly acting along E-W, NE-SW and NW-SE oriented high-angle faults, caused the stretching of the mountain chain (e.g., [D'Agostino et al., 2001](#)). The opening and evolution of these intermountain basins started from the Late Pliocene-Lower

154 Pleistocene period (Galadini and Galli, 2000; Boncio et al., 2004; Giaccio et al., 2012a; Amato et al., 2014).
155 The Plio-Quaternary tectonic and sedimentary evolution of the Fucino Basin was driven by the *Fucino Fault*
156 *System* (FFS, Galadini and Galli, 2000; Fig. 1c), which depicts a semi-graben architecture with an increasing
157 thickness of the Plio-Quaternary sedimentary infilling of up to ~900 m from west to east toward the depocenter
158 (Cavinato et al., 2002; Patacca et al., 2008).

159 The Fucino Basin, unlike other intra-Apennine basins, has likely undergone continuous sedimentation (~0,45
160 mm/yr in average in the central-eastern sector of the basin; Giaccio et al., 2017, 2019; Mannella et al., 2019)
161 since the Plio-Pleistocene and to recent historical times, i.e., potentially covering the last ~2.0 Ma (Giaccio et
162 al., 2015). Indeed, the basin hosted a lake, *Lacus Fucinus*, which was first partially reclaimed during Emperors
163 Claudius and Hadrian reigns (1st-2nd century CE), and then completely drained by the Torlonia family at the
164 end of the 19th century.

165
166

166 **2.2. The peri-Tyrrhenian potassic volcanic systems**

167 The Quaternary peri-Tyrrhenian volcanic systems of central-southern Italy (hereafter peri-Tyrrhenian potassic
168 volcanoes) belong to the *Roman Comagmatic Region* of Washington (1906), which comprises the volcanic
169 centers and areas fed by potassic and ultrapotassic magmas extending from southern Tuscany, through
170 Latium and Campania, i.e., from north-west to south-east (Fig. 1a and 1b): Vulsini, Vico, Sabatini and Colli
171 Albani (grouped in the *Roman Province* s.s. by Peccerillo, 2017), Volsci and Roccamonfina (*Ernici-*
172 *Roccamonfina Province*; Peccerillo, 2017) and the active volcanoes of the so-called *Campanian Volcanic*
173 *Zone* (Rolandi et al., 2003; or *Campanian Province*; Peccerillo, 2017), including Campi Flegrei, Ischia, Procida
174 and Somma-Vesuvius, also known as the *Neapolitan* volcanoes. Volcanism in the region started at the
175 beginning of the Middle Pleistocene, but the volcanic centers have been active during different time intervals
176 (Fig. 3). Direct evidence, i.e., near-vent deposits, of the oldest activity is documented within the Volsci Volcanic
177 Field (Cardello et al., 2020; Marra et al., 2021), which covers the 760-230 ka interval (Boari et al., 2009;
178 Centamore et al., 2010; Marra et al., 2021). Possible evidence of similarly old activity at Sabatini is provided
179 by distal tephra layers found in Tiber River delta, dated between 750 and 810 ka (Marra et al., 2014). During
180 the ~600-415 ka interval, the Vulsini, Sabatini, Colli Albani, Volsci and Roccamonfina volcanic complexes were
181 all simultaneously active (e.g., Sottili et al., 2004; Rouchon et al., 2008; Boari et al., 2009; Palladino et al.,
182 2010; Soligo and Tuccimei, 2010). Around ~415 ka, volcanic activity also started at Vico volcano (Pereira et
183 al., 2020). Finally, the onset of volcanic activity at Neapolitan volcanoes occurred around ~300 ka (Rolandi et
184 al. 2003), although there is growing evidence from distal settings revealing significantly older activity in this
185 region, extending as far back as at least 560 ka or perhaps more (e.g., Giaccio et al., 2014; Petrosino et al.,
186 2015; Wagner et al., 2019).

187 In summary, all the Latium (i.e., Vulsini, Vico, Sabatini, Colli Albani and Volsci) and Roccamonfina volcanoes
188 were active during the interval investigated in this study (i.e., 430-365 ka), consequently there is quite a degree
189 of complexity when trying to establish the volcanic source of distal ash layers deposited during this interval
190 (Fig. 3).

191
192
193
194
195
196
197
198
199
200
201
202
203
204
205
206
207
208
209
210
211
212
213
214
215
216
217
218
219
220
221
222
223
224
225
226
227
228
229
230
231
232
233
234
235
236
237
238
239
240
241
242
243
244
245
246
247
248
249
250
251
252
253
254
255
256
257
258
259
260
261
262
263
264
265

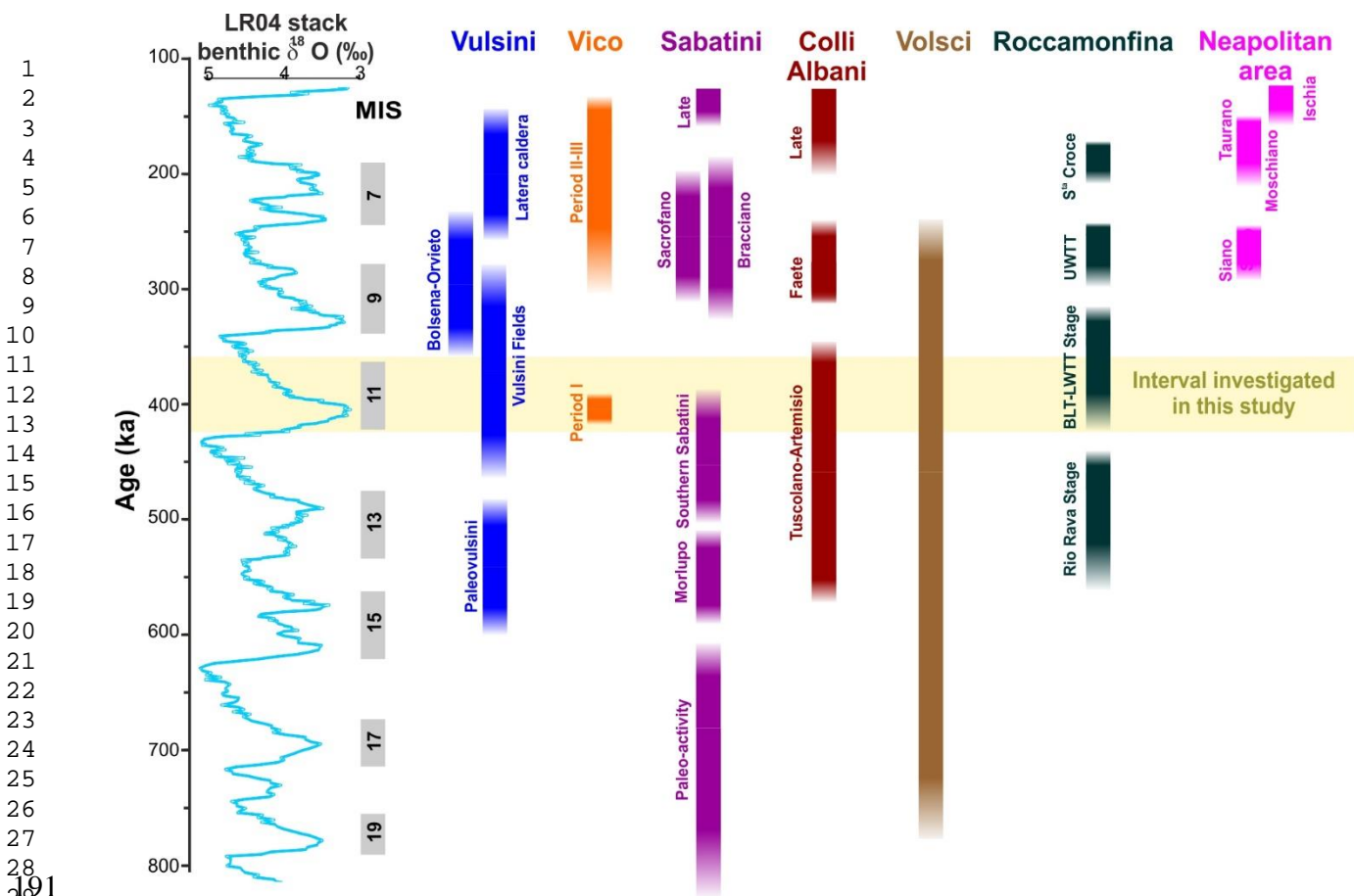


Figure 3. Temporal distribution of the Middle Pleistocene volcanic activity from the peri-Tyrrhenian potassic volcanic systems, plotted against the LR04 benthic stack record (Lisiecki and Raymo, 2005) Data source: Vulsini volcanic district: Palladino et al. (2010), Marra et al. (2020a); Vico: Perini et al. (2004), Pereira et al. (2020); Monti Sabatini volcanic district: Sottili et al. (2010), Marra et al. (2014, 2020b); Colli Albani: Marra et al. (2009); Volsci Volcanic Field: Boari et al. (2009), Centamore et al. (2010), Marra et al. (2021); Roccamonfina: Giannetti (1996a, 1996b), Giannetti and De Casa (2000), Rouchon et al. (2008), Scaillet et al. (2008); Neapolitan area: De Vivo et al. (2001), Rolandi et al. (2003), Belkin et al. (2016), Sbrana et al. (2018).

3. Materials and methods

3.1. Investigated tephra from F4-F5 cores and Roman volcanic province

A summary of the investigated tephra from Fucino and the Roman volcanic area in this study, and those available in the literature, is reported in Table 1.

Two cores were recovered at the F4-F5 drill site in the central area of the basin (Fig. 1c) and combined to a composite profile 98 meters long. Drilling site selection strategy and recovery procedure are reported in Giaccio et al. (2019). The F4-F5 composite record contains at least 130 tephra (Giaccio et al., 2019; Fig. 2). Based on correlations with tephra layers from the nearby F1-F3 record covering the last 190 kyr (Fig. 2; Giaccio et al., 2017), the geochemical fingerprinting of 11 relevant tephra markers, one direct $^{40}\text{Ar}/^{39}\text{Ar}$ age determination, and the recognition of a climatic proxy variability linked to glacial-interglacial cyclicity, the sediment succession from F4-F5 was ascribed to the last 430 kyr (Fig. 2; Giaccio et al., 2019). In this paper, we focus on the lowermost ~17 meter-thick interval (between ~80 and ~98 m composite depth) of the F4-F5 core, spanning a ~60 kyr time interval, between the lowermost tephra layer labelled TF-126, which is directly dated by $^{40}\text{Ar}/^{39}\text{Ar}$ method at 424.3 ± 3.2 ka (Giaccio et al., 2019), and the tephra TF-85, correlated to the Villa Senni eruption (i.e., Tufo Lionato) from the Colli Albani (Giaccio et al., 2019), which is dated at 367.6 ± 1.6 ka (Marra et al., 2009; Giaccio et al., 2012b; Fig. 2). This interval contains 32 ash layers, out of which 28 are investigated and

215 presented in this study, while 4 (i.e., TF-85, TF-117, TF-118 and TF-126) were already studied and reported
 216 in [Giaccio et al. \(2019\)](#).
 217
 218

Table 1. Data acquired in this study and available from literature for each investigated Fucino tephra or proximal volcanic unit.

Tephra	Site/Section	Type of analysis			
		Glass-WDS (EMPA)	Trace elements (LA-ICP-MS)	Sr isotopes (TIMS)	⁴⁰ Ar/ ³⁹ Ar
TF-85	F4-F5	Yes ^a	No	Yes ^b	Yes ^b
TF-88	F4-F5	Yes ^b	No	No	No
TF-89	F4-F5	Yes ^b	No	No	No
TF-90	F4-F5	Yes ^b	No	No	No
TF-93	F4-F5	Yes ^b	No	No	No
TF-94	F4-F5	Yes ^b	No	No	No
TF-96	F4-F5	Yes ^b	No	No	No
TF-97	F4-F5	Yes ^b	No	No	No
TF-98	F4-F5	Yes ^b	No	No	No
TF-99	F4-F5	Yes ^b	No	No	No
TF-100	F4-F5	Yes ^b	No	No	No
TF-102	F4-F5	Yes ^b	No	No	No
TF-103	F4-F5	Yes ^b	No	No	No
TF-104	F4-F5	Yes ^b	No	No	No
TF-106	F4-F5	Yes ^b	No	No	No
TF-107	F4-F5	Yes ^b	Yes ^b	Yes ^b	No
TF-108	F4-F5	Yes ^b	No	No	No
TF-109	F4-F5	Yes ^b	No	No	No
TF-110	F4-F5	Yes ^b	No	No	No
TF-111	F4-F5	Yes ^b	Yes ^b	Yes ^b	No
TF-114	F4-F5	Yes ^b	No	No	No
TF-115	F4-F5	Yes ^b	No	No	No
TF-116	F4-F5	Yes ^a	Yes ^b	No	No
TF-117	F4-F5	Yes ^a	No	No	Yes ^b
TF-118	F4-F5	Yes ^b	No	No	No
TF-120	F4-F5	Yes ^b	No	No	No
TF-121	F4-F5	Yes ^b	No	No	No
TF-122	F4-F5	Yes ^b	No	No	No
TF-123	F4-F5	Yes ^b	No	No	No
TF-124	F4-F5	Yes ^b	No	No	No
TF-125	F4-F5	Yes ^b	Yes ^b	No	No
TF-126	F4-F5	Yes ^a	Yes ^b	Yes ^b	Yes ^a
Casale delle Piane	Tuscania	Yes ^b	No	No	No
Castel Broco	Tuscania	Yes ^a	Yes ^b	Yes ^b	No
Vico α (TSP-1)	Tuscania	Yes ^b	No	No	No
TSP-2	Tuscania	Yes ^b	No	No	No
TSP-3	Tuscania	Yes ^b	No	Yes ^b	No
TSP-4	Tuscania	Yes ^b	No	No	No
Riano R-1	Riano	Yes ^b	Yes ^b	Yes ^b	Yes ^c
Pozzolane Nere	Rome	Yes ^d	No	Yes ^f	Yes ^b
Vico β	Vignanello	Yes ^e	Yes ^b	No	Yes ^e
Vico α type locality	Viterbo	Yes ^e	Yes ^b	No	Yes ^e

^a [Giaccio et al. \(2019\)](#); ^b This study; ^c [Marra et al. \(2018\)](#); ^d [Marra et al. \(2009\)](#); ^e [Pereira et al. \(2020\)](#); ^f [Gaeta et al. \(2006\)](#).

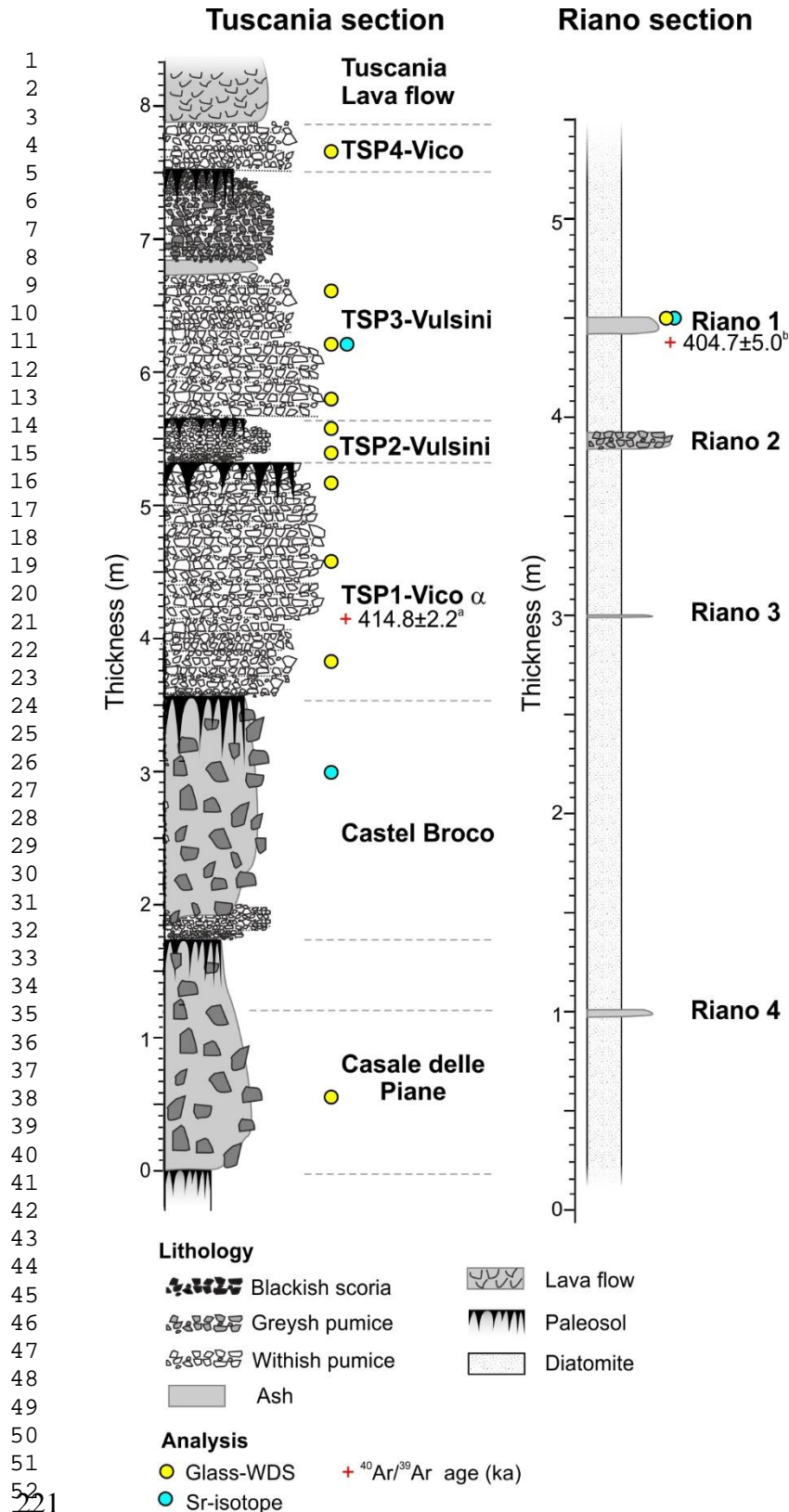


Figure 4. Reference stratigraphic successions outcropping at Tuscania-San Pietro (southern Vulsini) and Riano (eastern Sabatini) (see Fig. 1b for locations). The stratigraphic position of the samples used for geochemical analyses in this study are also shown. $^{40}\text{Ar}/^{39}\text{Ar}$ dating: ^a Pereira et al. (2020); ^b Marra et al. (2018).

In order to improve the reference geochemical dataset required for establishing reliable tephra correlations of the Fucino tephra, we re-examined the key pyroclastic succession at Tuscania-San Pietro (southern Vulsini;

229 Cioni et al., 1987; Palladino et al., 1994, 2010; 42° 24' 43.32" N, 011° 52' 45.13" E; Fig. 1b; Fig. 4) and
230 performed new analyses on four pumice fall units (TSP#). Of these, TSP-1 is correlated to the Vico α Plinian
231 fall marker (Cioni et al., 1987), while TSP-2 and TSP-3 are referred to the Plinian activity of the Vulsini Fields
232 (although with undefined source locations). In particular, TSP-3 is tentatively correlated to the Pumice Fall 0
233 (PF-0) of Turbeville (1992, 1993) dated at 399.8 ± 18.0 ka (Turbeville, 1992; age recalculated according to the
234 Alder Creek sanidine at 1.1891 Ma). We stress that this attribution is just putative until it will be corroborated
235 by stratigraphical and geochemical characterization of proximal PF-0 products collected in the type locality.
236 Finally, the Plinian fall horizon TSP-4 is attributed to Vico Plinian activity, although with an uncertain correlation.
237 The TSP succession also includes the Casale delle Piane and Castel Broco major pyroclastic flow deposits
238 (also considered in the present study, see below) and is topped by the Tuscania lavas (Palladino et al., 1994,
239 2010), which are broadly coeval with the Quarticcio lavas (356 ± 15 ka; Funicello et al., 2012) outcropping in
240 nearby localities.
241 To supplement the major element datasets for Vico volcano presented in Pereira et al., (2020), we provide
242 trace element glass analyses of selected proximal Vico α and β samples collected from Viterbo (Vico α ; Lower
243 fall [VT-Base Vico α] and Upper fall [VT-1A, VT-1B and VT-1C] and Vignanello (Vico β [VIG-3]) sections.
244 With the same aim, we also analysed the Riano R-1 tephra (Fig. 4), found within a lacustrine (diatomite)
245 succession outcropping along the Flaminia road (42° 05' 24.06" N, 012° 31' 57.43" E), north of Rome (Fig.
246 1b), and dated at 404.7 ± 5.0 ka by Marra et al. (2018). The Riano R-1 tephra is a 10-cm-thick, coarse to fine
247 blackish ash layer, likely representing a relatively distal occurrence of a major fall deposit, of uncertain, Sabatini
248 or external (i.e., from another Latium volcano), source area. The Riano diatomite succession contains three
249 additional tephra layers (R-2, R-3 and R-4; Fig. 4). However, while R-2 is a 10-cm-thick layer of dense scoria
250 lapilli, likely deriving from a minor local, i.e., Sabatini, Strombolian eruption, the ash layers R-3 and R-4 did not
251 yield fresh glass suitable for geochemical analyses.
252 Finally, in order to acquire a new $^{40}\text{Ar}/^{39}\text{Ar}$ age for the Colli Albani Pozzolane Nere caldera-forming eruption,
253 we sampled an exposure in Rome City (41° 50' 44.74" N, 012° 28' 40.56" E). Indeed, since we could not
254 establish which one of the two different monitor standards was used for determining the previous set of
255 $^{40}\text{Ar}/^{39}\text{Ar}$ ages for this deposit (Karner and Renne, 1998), the existing age of 407 ± 2 ka can not be recalculated
256 with respect to the current monitor standard improved ages, and thus does not allow direct comparisons.

3.2. EMP-WDS

258 Major and minor element compositions were determined on micro-pumice fragments and/or glass shards of
259 the 28 tephra layers from the F4-F5 record (Table 1), which were labelled following the same criteria adopted
260 in previous studies of the F1-F3 and F4-F5 cores (Giaccio et al., 2017, 2019), and for the above described five
261 proximal samples (Table 1). In order to have a good statistical expression of the tephra composition and their
262 geochemical variability, we aimed at analysing at least 10-15 shards/micro-pumices from each tephra.
263 However, in some cases (i.e., TF-96, TF-100, TF-107 and TF-123), the dense microlithic texture of the juvenile
264 clasts or the incipient alteration of the glass prevented us to acquire such a satisfactory number of analyses.
265 Nevertheless, also in those cases, the relatively homogeneity and/or geochemical consistency of the analysed
266 glasses indicate a satisfactory reliability and representativity of the compositional data for tephrochronological
267 purposes. A synthesis of all acquired data for each of the 28 tephra and 4 proximal pyroclastic units can be
268

269 found [Table 1](#), along with information relative to previously investigated tephra from F4-F5 core and proximal
 270 volcanics.

271 Polishing and carbon coating of the epoxy slides were performed for electronprobe microanalyser wavelength
 272 dispersive spectroscopy (EPMA-WDS) analysis at the *Istituto di Geologia Ambientale e Geoingegneria* of the
 273 Italian National Research Council (IGAG-CNR, Rome). Major and minor elements quantitative analyses were
 274 performed with a CAMECA SX-50 EPMA equipped with five-wavelength dispersive spectrometers (WDS),
 275 operating at 15 kV accelerating voltage, 15 nA beam current, 10 μm defocused beam diameter - to limit Na
 276 mobilization and loss - and 20 s element counting time for all elements. Wollastonite (Si and Ca), corundum
 277 (Al), periclase (Mg), magnetite (Fe), rutile (Ti), orthoclase (K), jadeite (Na), phlogopite (F), potassium chloride
 278 (Cl), barite (S), F-apatite (P) and metals (Mn) were used as internal standards. The Kakanui augite and
 279 Rhyolite RLS132 glasses from the United States Geological Survey were measured prior to each analytical
 280 run to evaluate the accuracy of the electron-microprobe analysis. Obtained mean values are shown in Table
 281 2, along with the difference % between each oxide with respect to the recommended values. The mean values
 282 show ~0.5% difference for SiO₂, ranging in concentrations from 50 wt% to 77 wt%, <0.2% for oxides in the 15-
 283 16 wt% concentration range, 3.3-1.8% for oxide concentrations between 5 and 12 wt%, 4.2-0.1% for oxides in
 284 the 2-5 wt% range, up to 5.7% for the oxides ranging from 0.2 wt% to 2 wt% and up to 39% for minor elements
 285 (i.e., oxides with concentrations <0.2 wt%).

286 In order to test the quality and reproducibility of our data, we also performed a series of analysis on the MPI-
 287 DING glass standards of Jochum et al. (2006) and a rhyolitic Lipari obsidian (i.e., ID3506; Kuehn et al., 2011).
 288 The results show <1.1% difference for SiO₂, ranging between 46 wt% and 77 wt% range, 2.8-0.2% for oxides
 289 ranging from 15 wt% to 27 wt%, 4.0-1.0% for oxides in the 5-13 wt% range, 5.2-0.6% for oxides ranging from
 290 2 wt% to 5 wt%, 8.1-1.5 for oxides in the 0.2-2 wt% range and up to 62% for minor elements (Table 2).

291 Data reduction was carried out using the PAP correction, while data processing was performed in Microsoft
 292 Excel. We adopted 93 wt% as a threshold for the measured total: analysis with total values lower than 93 wt%
 293 were discarded. All compositional data are shown as oxide weight percentages (wt%) in the Total Alkali vs
 294 Silica (TAS; Le Maitre et al., 2002) classification diagram - as well as bi-plots diagrams - with total iron (FeO_T)
 295 calculated as FeO and normalized to 100% on a volatile-free basis (i.e., excluding Cl, SO₃ and F volatiles) for
 296 correlation purposes. Collected data are all reported in Supplementary Dataset-1, along with secondary
 297 standards and MPI-DING measured values.

299 **Table 2.** Comparison between the measured and recommended values of secondary standards employed in this study (Kakanui Augite,
 300 Rhyolite RLS132, USGS, MPI-DING glass standards of Jochum et al., 2006, and Lipari obsidian ID3506, Kuehn et al., 2011).

Standard		Lipari (ID3506, Kuehn et al., 2011)												
Oxide	SiO ₂	TiO ₂	Al ₂ O ₃	FeO _{TOT}	MnO	MgO	CaO	Na ₂ O	K ₂ O	P ₂ O ₅	F	Cl	SO ₂	
Recommended values	74.94	0.07	13.25	1.57	0.07	0.04	0.74	4.12	5.17	0.01	0.15	0.34	0.01	
Measured (mean n 5)	75.43	0.07	12.83	1.61	0.06	0.04	0.75	3.99	5.20	0.01	0.11	0.33	0.01	
s.d.	0.47	0.00	-0.43	0.04	0.00	0.00	0.01	-0.13	0.03	0.00	-0.04	-0.02	0.00	
Difference %	0.63	-0.36	-3.21	2.86	-2.55	-10.48	1.88	-3.16	0.55	23.51	-27.51	-5.11	-20.51	
Standard		ATHO-G (Jochum et al., 2006)												
Oxide	SiO ₂	TiO ₂	Al ₂ O ₃	FeOT	MnO	MgO	CaO	Na ₂ O	K ₂ O	P ₂ O ₅	F	Cl	SO ₂	
Recommended values	75.79	0.26	12.23	3.28	0.11	0.10	1.70	3.76	2.65	0.03		0.04		
Measured (mean n. 10)	76.20	0.25	11.89	3.28	0.12	0.10	1.79	3.64	2.70	0.02	0.10	0.04	0.01	
s.d.	0.31	0.02	0.13	0.13	0.04	0.01	0.05	0.09	0.07	0.02	0.10	0.01	0.01	
Difference %	0.44	-2.27	-2.84	-0.05	13.15	-2.48	4.86	-3.38	2.09	-5.46	-	-9.71	-	
Standard		GOR128-G (Jochum et al., 2006)												

Oxide	SiO ₂	TiO ₂	Al ₂ O ₃	FeO _{TOT}	MnO	MgO	CaO	Na ₂ O	K ₂ O	P ₂ O ₅	F	Cl	SO ₂
Recommended values	46.49	0.29	9.99	9.89	0.18	26.22	6.29	0.58	0.04	0.03			
Measured (mean n. 9)	47.02	0.27	9.61	9.86	0.20	26.08	6.32	0.57	0.04	0.03	0.05	0.01	0.00
s.d.	0.57	0.02	0.10	0.33	0.04	0.26	0.09	0.02	0.01	0.03	0.09	0.01	0.01
Difference %	1.13	-6.51	-3.81	-0.30	10.02	-0.54	0.48	-2.21	4.93	25.85	-	-	-
Standard StHs 6/80-G (Jochum et al., 2006)													
Recommended values	63.83	0.70	17.84	4.38	0.08	1.97	5.29	4.45	1.29	0.16	0.03	0.02	
Measured (mean n. 9)	64.27	0.68	17.28	4.32	0.09	1.99	5.39	4.54	1.27	0.16	0.02	0.02	0.01
s.d.	0.46	0.03	0.09	0.18	0.04	0.03	0.10	0.14	0.04	0.03	0.03	0.01	0.01
Difference %	0.69	-3.11	-3.13	-1.45	21.11	0.89	1.84	2.12	-1.37	-2.88	-30.30	-2.26	
Standard Kakanui Augite (USGS)													
Recommended values	50.56	0.84	8.30	6.52	0.13	16.31	16.03	1.30					
Measured (mean n. 5)	50.99	0.79	8.15	6.42	0.18	16.28	15.85	1.30	0.01	0.02	0.04	0.01	0.02
sd	0.34	0.02	0.04	0.15	0.04	0.31	0.06	0.04	0.01	0.01	0.04	0.01	0.02
Difference %	-0.43	0.05	0.15	0.11	-0.05	0.03	0.18	0.00	-0.01	-0.02	-0.04	-0.01	-0.02
Standard Rhyolite RLS132 (USGS)													
Recommended values	76.56	0.19	11.58	2.03	0.16	0.08	0.10	4.78	4.50				
Measured (mean n. 15)	76.95	0.19	11.20	2.12	0.15	0.05	0.11	4.70	4.50	0.02	0.18	0.20	0.02
sd	0.25	0.02	0.13	0.07	0.02	0.02	0.02	0.19	0.06	0.01	0.11	0.02	0.02
Difference %	0.52	0.64	-3.29	4.17	-5.52	-36.41	5.79	-1.82	-0.02				

Note: Here all values are reported at second decimal digits, but some errors (difference%) are calculated up to the fourth digits, especially for minor elements.

3.3. LA-ICP-MS

Trace element analyses were conducted on volcanic glasses from five Fucino tephra units, i.e., TF-107, TF-111, TF-116, TF-125, and TF-126, and four proximal-medial pyroclastic deposits, i.e., the Castel Broco unit, from the above described Tuscania-San Pietro section at Vulsini (Fig. 4), Vico α and β , and the Riano R-1 Tephra (unknown source) (Table 1). These samples have been selected (i) to test if compositions of the trace elements and/or the ratios of incompatible trace elements allow distinguishing of tephra layers with major element composition alone (e.g., TF-107, TF-111, TF-126, Castel Broco, Riano R-1), and (ii) to obtain the complete geochemical composition of the products from the two major eruptions of Vico Period I (i.e., Vico α and Vico β), likely dispersed on wide areas of the central Mediterranean and thus representing potential tephra markers for this region. The analysis was performed using an Agilent 8900 triple quadrupole ICP-MS (ICP-QQQ) coupled to a Resonetics 193nm ArF excimer laser-ablation at the Department of Earth Sciences, Royal Holloway, University of London. Full analytical procedures for volcanic glass analysis are reported in Tomlinson et al. (2010). Spot sizes of 25 and 34 μm were used depending on the sample vesicularity and/or size of glass surfaces available for analysis. The repetition rate was 5 Hz, with a count time of 40 s on the sample, and 40 seconds on the gas blank to allow the subtraction of the background signal. Typically, blocks of eight or nine glass shards and one MPI-DING reference glass were bracketed by the NIST612 glass adopted as the calibration standard. The internal standard applied was ²⁹Si (determined by EMP-WDS analysis). In addition, MPI-DING reference glasses were used to monitor analytical accuracy (Jochum et al., 2006). LA-ICP-MS data reduction was performed in Microsoft Excel, as outlined in Tomlinson et al. (2010). Accuracies of LA-ICP-MS analyses of the MPI-DING reference glasses, ATHO-G and StHs6/80-G, were typically $\leq 5\%$ for most elements measured. These measurements are provided in Supplementary dataset 2 (SD-2), along with those of selected proximal eruption units and the full Fucino dataset.

327
328
329
330
331
332
333
334
335
336
337
338
339
340
341
342
343
344
345
346
347
348
349
350
351
352
353
354
355
356
357
358
359
360
361
362
363
364
365
366
367
368
369
370
371
372
373
374
375
376
377
378
379
380
381
382
383
384
385
386
387
388
389
390
391
392
393
394
395
396
397
398
399
400
401
402
403
404
405
406
407
408
409
410
411
412
413
414
415
416
417
418
419
420
421
422
423
424
425
426
427
428
429
430
431
432
433
434
435
436
437
438
439
440
441
442
443
444
445
446
447
448
449
450
451
452
453
454
455
456
457
458
459
460
461
462
463
464
465
466
467
468
469
470
471
472
473
474
475
476
477
478
479
480
481
482
483
484
485
486
487
488
489
490
491
492
493
494
495
496
497
498
499
500
501
502
503
504
505
506
507
508
509
510
511
512
513
514
515
516
517
518
519
520
521
522
523
524
525
526
527
528
529
530
531
532
533
534
535
536
537
538
539
540
541
542
543
544
545
546
547
548
549
550
551
552
553
554
555
556
557
558
559
560
561
562
563
564
565
566
567
568
569
570
571
572
573
574
575
576
577
578
579
580
581
582
583
584
585
586
587
588
589
590
591
592
593
594
595
596
597
598
599
600
601
602
603
604
605
606
607
608
609
610
611
612
613
614
615
616
617
618
619
620
621
622
623
624
625
626
627
628
629
630
631
632
633
634
635
636
637
638
639
640
641
642
643
644
645
646
647
648
649
650
651
652
653
654
655
656
657
658
659
660
661
662
663
664
665
666
667
668
669
670
671
672
673
674
675
676
677
678
679
680
681
682
683
684
685
686
687
688
689
690
691
692
693
694
695
696
697
698
699
700
701
702
703
704
705
706
707
708
709
710
711
712
713
714
715
716
717
718
719
720
721
722
723
724
725
726
727
728
729
730
731
732
733
734
735
736
737
738
739
740
741
742
743
744
745
746
747
748
749
750
751
752
753
754
755
756
757
758
759
760
761
762
763
764
765
766
767
768
769
770
771
772
773
774
775
776
777
778
779
780
781
782
783
784
785
786
787
788
789
790
791
792
793
794
795
796
797
798
799
800
801
802
803
804
805
806
807
808
809
810
811
812
813
814
815
816
817
818
819
820
821
822
823
824
825
826
827
828
829
830
831
832
833
834
835
836
837
838
839
840
841
842
843
844
845
846
847
848
849
850
851
852
853
854
855
856
857
858
859
860
861
862
863
864
865
866
867
868
869
870
871
872
873
874
875
876
877
878
879
880
881
882
883
884
885
886
887
888
889
890
891
892
893
894
895
896
897
898
899
900
901
902
903
904
905
906
907
908
909
910
911
912
913
914
915
916
917
918
919
920
921
922
923
924
925
926
927
928
929
930
931
932
933
934
935
936
937
938
939
940
941
942
943
944
945
946
947
948
949
950
951
952
953
954
955
956
957
958
959
960
961
962
963
964
965
966
967
968
969
970
971
972
973
974
975
976
977
978
979
980
981
982
983
984
985
986
987
988
989
990
991
992
993
994
995
996
997
998
999
1000

3.4. Isotopic composition of strontium

Strontium (Sr) isotope compositions were determined on glass shards/pumices and mineral phases (i.e., feldspar, leucite and pyroxene) from six selected samples, as summarised in [Table 1](#). The rationale underlying the selection of these samples is similar to that for LA-ICP-MS analysis, i.e., obtaining a further geochemical characterization of the tephra from some major eruptions of the peri-Tyrrhenian volcanoes during MIS 11 period, in order to have, if any, an additional fingerprinting tool for strengthening their recognition/discrimination in distal settings. The variable fractions were handpicked under a binocular microscope. When possible, the cleanest crystals were selected, avoiding the presence of glass rinds attached. Before chemical dissolution, glass shards and pumices were acid leached three/five times to reduce alteration effects. Leaching was carried out each time by placing the beakers containing samples and high-purity 6 N HCl on a hot plate for 10 min. Feldspar and pyroxene separates coated by a thin film of glass were leached with high-purity 7% HF for 10 min in an ultrasonic bath. After leaching, samples were rinsed with Milli Q[®] H₂O and dissolved with high-purity HF–HNO₃–HCl mixtures. Sr was separated from the matrix through conventional ion-exchange procedures at the clean chemistry laboratory of the *Istituto Nazionale di Geofisica e Vulcanologia, Osservatorio Vesuviano*. Sr blank was on the order of 0.3 ng during chemistry processing.

Sr isotopic compositions were determined by thermal ionization mass spectrometry (TIMS) at DiSTAR (Naples, Italy), using a Thermo Scientific Triton Plus mass spectrometer equipped with one fixed and eight adjustable Faraday cups. $2\sigma_{\text{mean}}$, i.e., the standard error with $N = 150$, was better than ± 0.000008 for all Sr measurements. Measured $^{87}\text{Sr}/^{86}\text{Sr}$ ratios were normalized for within-run isotopic fractionation to $^{88}\text{Sr}/^{86}\text{Sr} = 8.37521$. During the period of isotopic data collection, replicate analyses of NIST–SRM 987 (SrCO_3) international reference standard were carried out to check for external reproducibility 2σ (where σ is the standard deviation of the standard results, according to [Goldstein et al., 2003](#)). No correction has been applied to the measured $^{87}\text{Sr}/^{86}\text{Sr}$ values, since the mean measured value of $^{87}\text{Sr}/^{86}\text{Sr}$ for NIST–SRM 987 standard was 0.710248 ± 0.000006 (2σ , $N = 17$), which is indistinguishable from the recommended value of $^{87}\text{Sr}/^{86}\text{Sr} = 0.710248$ ([Thirlwall, 1991](#)).

3.5. $^{40}\text{Ar}/^{39}\text{Ar}$ geochronology

In order to improve the chronology of the investigated interval of the F4-F5 record, three new $^{40}\text{Ar}/^{39}\text{Ar}$ dating were performed on TF-85 and TF-117 samples, correlated to the Villa Senni and Pozzolane Nere eruptions, respectively ([Giaccio et al., 2019](#)), and on a sample of the proximal Pozzolane Nere (PN) unit collected from the above-mentioned outcrop in Rome City ([Table 1](#)). Samples were sieved and cleaned in distilled water, while undesirable magnetic crystals were removed by magnetic separation. Approximately thirty crystals were selected from each sample and loaded into an aluminium disk in three individual pits. All crystals from the individual samples were irradiated for 120 min in the Cd-lined, in-core CLICIT facility of the Oregon State University TRIGA reactor (IRR CO002). Interference corrections were based on the nucleogenic production ratios given in [Renne et al. \(2015\)](#). After irradiation, samples were transferred into a copper sample holder and loaded individually into a differential vacuum Cleartan[®] window. All measurements were done in the LSCE $^{40}\text{Ar}/^{39}\text{Ar}$ facility (France). Detailed analytical procedures can be found in [Nomade et al. \(2010\)](#). Single crystals were fused individually using a 25 Watts Synrad CO₂ laser at about 10 to 15 % of the nominal power. Extracted gas was then purified for 10 min by two hot GP 10 and two GP 50 getters (ZrAl). Argon isotopes (^{40}Ar , ^{39}Ar ,

368 ^{38}Ar , ^{37}Ar and ^{36}Ar) were successively measured using a VG 5400 mass spectrometer equipped with an
369 electron multiplier (Balzer SEV 217 SEN) coupled with an ion counter. Each argon isotope measurement
370 consisted of 20 cycles of peak-hopping. Neutron fluence J for each sample was calculated using co-irradiated
371 Alder Creek sanidine standard (ACs at 1.1891 Ma; [Niespolo et al., 2017](#)) and the K total decay constant of
372 [Renne et al. \(2011\)](#). This calibration produces ages independent of the astronomical tuning. J-values are the
373 followings: TF-85 (Villa Senni) = $0.00053020 \pm 0.00000053$, TF-117 (Pozzolane Nere) = $0.00052950 \pm$
374 0.00000053 and PN = $0.00053260 \pm 0.00000059$. Mass discriminations were monitored by analysis of air
375 pipette throughout the analytical period, and relative to a $^{40}\text{Ar}/^{36}\text{Ar}$ ratio of 298.56 ([Lee et al., 2006](#)). Procedural
376 blank measurements were achieved after every two or three unknown samples. For 10 min times of isolation
377 typical backgrounds are about $2.5\text{-}4.0 \times 10^{-17}$ and 5.0 to 7.0×10^{-19} moles for ^{40}Ar and ^{36}Ar , respectively.

378 379 **3.6. Age-depth modelling**

380 The age model and corresponding 95%-confidence interval were both obtained using the Bacon software
381 ([Blaauw and Christen, 2011](#)) written in the open-source statistical environment R ([R Core Team, 2016](#)).

382 To accommodate large differences in the sedimentation rate occurring during the investigated interval, we split
383 the record into three sedimentary zones A to C. Zone boundaries are defined through a preliminary evaluation
384 of changes in sedimentary facies and on the availability of the dated points. The definition of sedimentary
385 facies is based on the analysis of the composite profile derived by stacking consecutive core images acquired
386 by the ITRAX core scanner ([Giaccio et al., 2019](#)). For each interval, the mean sedimentation rate is estimated
387 by dividing the thickness of the interval for the time span elapsed between the deposition of the youngest and
388 oldest dated tephra layers bracketing the interval, or at least, a large part of it. In the case of multiple dated
389 layers in close stratigraphic position, we choose those featuring the most accurate dating. Sedimentary
390 intervals and estimated mean sedimentation rates are as follows:

- 391
392
393
394
- 395 • Zone A: 80.520 – 91.810 m, 33.33 cm/kyr
 - 396 • Zone B: 91.810 – 95.950 m, 30.30 cm/kyr
 - 397 • Zone C: 95.950 – 98.100 m, 4.76 cm/kyr

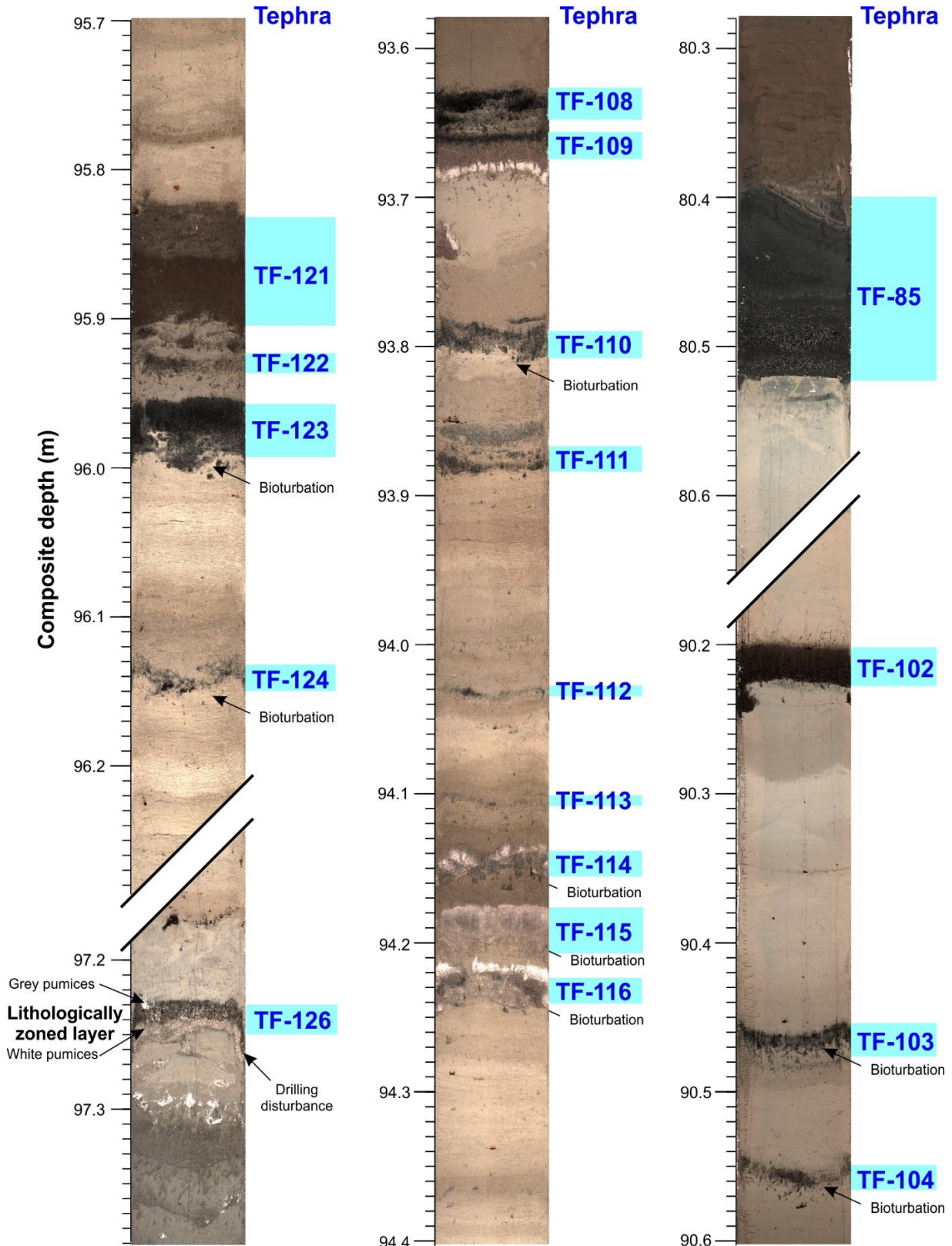
398 These zones do not represent homogeneous sedimentary facies; however, they represent the most accurate
399 approximation of long term (>4 kyr) changes in mean sedimentation rate that can be made on the basis of
400 currently available tephrochronological information.

401 402 **4. Results**

403 404 **4.1. Depositional and sedimentological features of the Fucino tephra succession**

405 Tephra layers in the Fucino lacustrine succession occur as discrete levels of ash with variable thickness (Table
406 3) and grain-size, well separated from each other by fine lake sediments (marl) (Fig. 5). In spite of a slight
407 bioturbation and/or mechanic disturbance related to the drilling operation (Fig. 5), each tephra layer shows
408 distinctive lithological (i.e., grain-size, shape, colour, vesicularity pattern and textural features of the juvenile
409 clasts, type and assemblage of the crystal and lithic components) and geochemical (glass-WDS major element
410 composition) features. These circumstances are verified also in the case of closely clustered tephra layers,
411 i.e., each layer forming the cluster presents its own distinctive lithological and geochemical characteristics with

409 respect to the adjacent ones. In some cases, tephra layers are also characterised by a sharp lower boundary
 410 and by an upsection lithological zonation (e.g., TF-126; Fig. 5). These features clearly indicate that tephra
 411 layers are undoubtedly primary fallout deposits and that post-depositional processes are negligible and did not
 412 affect the integrity of the tephra succession.
 413



414 Figure 5. Representative Fucino core sections, showing the general sedimentological and lithological features of the investigated tephra.
 415

4.2. Tephra lithology and glass composition

4.2.1. Data summary

The thickness and main lithological features of the 32 Fucino tephra and proximal volcanic units are summarized in [Tables 3 and 4](#), respectively. Full glass compositions are provided in Supplementary dataset 1 (SD-1), while their classification according to the total alkali vs silica (TAS) diagram ([Le Maitre et al., 2002](#)) is shown in [Figure 6](#). Description of the geochemistry (i.e., major, minor and trace elements and Sr-isotopes) of the volcanic glasses is given in the following sections.

Table 3. Main lithological, mineralogical and geochemical features of the 365-430 ka F4-F5 Fucino tephra.

Tephra	Thickness (cm)	Composite depth (m)	Core section and depth (cm)	CG	Lithology			Rock type
					Juvenile clasts	Minerals	Lithic content	
TF-85*	13.25	80.520	F5-49 74-88	ND	Black-brown scoria	Lc>bmca>cpx	Poor	K-f
TF-88	1.25	83.770	F4-51 131-133/ F5-51 65-66	CG-2	White pumice and grey-brown scoria	Kfs>cpx>bmca	Poor	ph-tr
TF-89	2.00	84.168	F5-51 107-109	CG-2	Grey scoria	Kfs>cpx>bmca	Poor	ph
TF-90	2.00	84.388	F5-51 130-131	CG-2	Black-grey scoria	Kfs>cpx>bmca	Rich	tr
TF-93	0.50	86.140	F4-53 51.3-52.2/ F5-52 149-150	CG-2	White pumice	Kfs>cpx	No	tph-ph
TF-94	0.75	86.853	F4-53 53.6-54.6	CG-2	White pumice	Kfs	No	ph-tr
TF-96	2.00	87.166	F4-53 85-86.2	CG-2	White pumice and grey scoria	Kfs>cpx	Poor	ph
TF-97	2.50	87.470	F4-53 110-112	CG-2	Grey scoria	Kfs>bmca	Poor	lat
TF-98	1.00	87.575	F4-53 119-120	CG-2	Grey scoria and whitish pumice	Kfs>bmca	Poor	lat-tph-ph-tr
TF-99	1.00	87.677	F4-53 128-129	CG-3	Highly vesicular white pumice and brown scoria	Kfs>bmca	Poor	K-tr-rhy
TF-100	6.75	88.045	F5-54 0-4.5	CG-1	Dense black scoria	Lc	Poor	K-f
TF-102	2.00	90.230	F4-55 58-60/ F5-54 125-126	CG-2	Poorly vesicular black scoria	Kfs>Lc>bmca	Poor	t-pht
TF-103	3.00	90.485	F4-55 83-86/ F5-54 133-134.2	CG-2	Poorly vesicular black scoria	Kfs>Lc>bmca	Poor	pht-tph
TF-104	1.25	90.560	F4-55 92-93/ F5-54 142-144	CG-2	Poorly vesicular grey scoria	Kfs>Lc>bmca	Poor	pht-tph
TF-106	1.25	90.860	F4-55 123-124.4	CG-2	Poorly vesicular grey scoria	Kfs>Lc>bmca	Rich	trb-pht-tph-sho
TF-107	2.00	91.620	F4-56 29-31/ F5-55 57.2-59	CG-2	Moderately vesicular whitish pumice and poorly vesicular greyish scoria	Kfs>bmca>cpx	Rich	ph-tr
TF-108	2.75	93.650	F5-56 110-113	CG-1	Dense, leucite-bearing black scoria	Lc	No	K-f
TF-109	2.00	93.690	F5-56 114-117	CG-3	Highly vesicular white pumice and greyish scoria	Kfs>bmca	Poor	K-ph-tr-rhy
TF-110	2.00	93.810	F5-56 126-128	CG-2	Highly vesicular white pumice and greyish scoria	Kfs>bmca	Poor	ph-tr
TF-111	1.50	93.885	F4-57 47-50	CG-2	Highly vesicular white pumice	Kfs>bmca	Very poor	ph-tr
TF-114	2.00	94.166	F4-57 77-79	CG-3	Highly vesicular white pumice and greyish scoria	Kfs>bmca>cpx	Poor	K-tr-rhy
TF-115	2.00	94.211	F4-57 81-83	CG-3	Highly vesicular white pumice	Kfs>bmca>cpx	Poor	K-tr-rhy
TF-116	2.50	94.251	F4-57 85-87	CG-3	Highly vesicular white pumice	Kfs>bmca>cpx	Poor	K-ph-tr-rhy
TF-117*	9.00	95.130	F4-57 151-152/ F5-57 0-7	ND	Poorly vesicular leucite-bearing black scoria	Lc>cpx	Poor	K-f
TF-118*	5.50	95.290	F5-57 16-23	ND	Poorly vesicular leucite-bearing black scoria	Lc	Poor	K-f
TF-120	2.00	95.540	F5-57 45-47	CG-2	Highly vesicular white pumice	Kfs>bmca	Very poor	ph-tr
TF-121	8.00	95.910	F5-57 77-85	CG-2	Poorly vesicular greyish-brownish scoria	bmca>Kfs>Lc	Poor	tph-ph-tr
TF-122	1.00	95.930	F5-57 85-86	CG-2	Dense, leucite-bearing brown scoria	Kfs>bmca>Lc	Poor	tph-ph-lat-tr
TF-123	5.50	96.005	F5-57 87-94	CG-2	Poorly vesicular black scoria	Lc>cpx>Kfs>bmca	Very rich	pht-tph
TF-124	0.75	96.155	F5-57 107-110	CG-2	Poorly vesicular black scoria and whitish pumice	Lc>cpx>bmca	Rich	sho
TF-125	3.50	96.775	F5-58 12-19.5	CG-3	Highly vesicular white pumice	Kfs>bmca>cpx>op	Poor	K-ph-tr-rhy
TF-126*	2.00	97.250	F5-58 64-66	ND	Highly vesicular white (base) and honey (top) pumice	Kfs>bmca>cpx>op	Poor	ph-tr

*=EPMA data in [Giaccio et al. \(2019\)](#); ND=Not determined in this study. Rock type abbreviations: K- = potassium- (suffix); f = foidite; ph = phonolite; tr = trachyte; tph = tephriphonolite; lat = latite; rhy = rhyolite. Mineral abbreviations: Kfs = K-feldspar; bmca = black mica; cpx = clinopyroxene; Lc = leucite; op = opaques. CG = compositional group (see [Fig. 6](#)).

Table 4. Geochemical and mineralogical data summary of the investigated proximal units.

Outcrop/ Location	Coordinates	Unit	Volcanic source	Lithology		Rock type
				Juvenile clasts	Minerals	
Tuscania- San Pietro	42° 24' 43.32" N – 11° 52' 45.13" E	Casale delle Piane	Vulsini	Highly vesicular dark grey, Kfs+bmca-bearing scoria	Kfs>bmca	Ph
		Vico α	Vico	Highly vesicular white, Kfs+bmca- bearing pumice and grey scoria	Kfs>bmca>cpx	K-tr-rhy
		TSP-2	Vulsini	Moderately vesicular grey Kfs- bearing pumice	Kfs>cpx	Ph
		TSP-3 (PF-0?)	Vulsini	Highly vesicular white, Kfs+bmca- bearing pumice	Kfs>bmca>cpx	Ph
		TSP-4	Vico	Reddish (thermally altered) Kfs- bearing pumice	Kfs>cpx	K-tr-rhy
Riano	42° 05' 24.06" N – 12° 31' 57.43" E	Riano R-1	ND (Sabatini?)	Blackish ash	Kfs>cpx>lc	Ph-tph-lat
Rome	41° 50' 44.74" N – 12° 28' 40.56" E	Pozzolane Nere	Colli Albani	Lc-bearing black scoria	Lc>cpx>bmca	K-f

ND=undetermined. Rock type abbreviations: K- = potassium- (suffix); f = foidite; ph = phonolite; tr = trachyte; tph = tephriphonolite; lat = latite; rhy = rhyolite. Mineral abbreviations: Kfs = K-feldspar; bmca = black mica; cpx = clinopyroxene; lc = leucite.

4.2.2. Major and minor elements

In the TAS diagram, the analysed tephra layers can be conveniently divided into three compositional groups (CGs; see also Table 3 for a classification summary). CG-1 (green area in Fig. 6) comprises of two tephra layers (i.e., TF-100 and TF-108), plus the previously investigated TF- 85, TF-117 and TF-118 layers (Giaccio et al., 2019), all displaying a K-foiditic composition. CG-2 (light-orange area) includes twenty-one F4-F5 tephra, plus two proximal units (TSP-2 and TSP-3), and the Riano R-1 tephra, and are classified as potassic phonotephrites, tephriphonolites, phonolites, latites and trachytes, each being often variable in composition and covering two or more fields of the TAS diagram (Fig. 6). Finally, CG-3 (blue area) includes six F4-F5 tephra (i.e., TF-99, TF-109, TF-114, TF-115, TF-116 and TF-125), and two proximal units (TSP-1/Vico α and TSP-4), which are phonolites-trachytes-rhyolites, trachytes-rhyolites and rhyolites. Although partially overlapping with CG-2 (Fig. 6), CG-3 tephra layers are clearly distinguishable owing to their distinctive rhyolitic components.

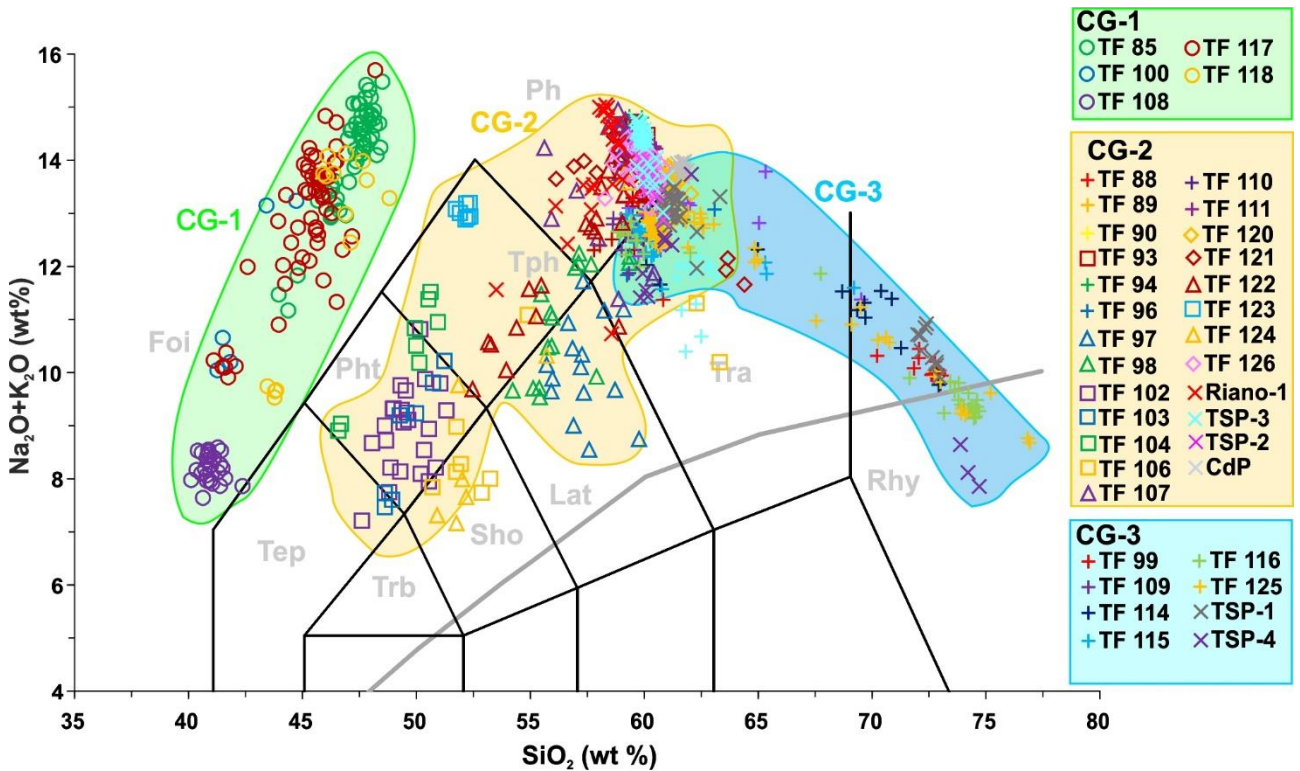


Figure 6. Total alkali vs silica (TAS) classification diagram (Le Maitre et al., 2002). The thirty-two F4-F5 MIS11 tephra and the proximal pyroclastic units plot in three compositional groups (CG-1, CG-2 and CG-3). Data source: glass-WDS of TF-85, TF-117, TF-118 and TF-

126: [Giaccio et al. \(2019\)](#); glass-WDS compositions of all others Fucino tephra and proximal pyroclastic units: this study. Foi=foidite; Pht=phonotephrite; Tph=Tephriphonolite; Ph=phonolite; Rhy=rhyolite; Tra=Trachyte; Lat=latite; Sho=Shoshonite; Trb=trachybasalt; Tep=tephrite; CdP=Casale delle Piane unit (Tuscania-San Pietro section).

4.2.3. Trace elements

The full trace element glass dataset of the tephra samples can be found in Supplementary dataset 2 ([SD-2](#)). Phono-trachytic tephra layers, TF-107 and TF-111 (CG2) display relatively heterogeneous, yet largely overlapping trace element concentrations, for instance Th contents range from 67-91 ppm and 66-95 ppm, respectively ([Fig. 7a](#)). Despite the variability in absolute concentrations of incompatible trace elements, ratios of High Field Strength Element (HFSE) to Th in both TF-107 (Nb/Th = 0.39 ± 0.02 ; Ta/Th = 0.021 ± 0.001 ; Zr/Th = 5.5 ± 0.5 [2 s.d.]) and TF-111 (Nb/Th = 0.39 ± 0.03 ; Ta/Th = 0.021 ± 0.001 ; Zr/Th = 5.6 ± 0.3 [2 s.d.]) remain constant, and indistinguishable from one another, possibly implying a common volcanic source. TF-116 belongs to CG3 and comprises phono-trachytic to rhyolitic glasses. However, our trace element analyses are derived from glass shards relating to the phono-trachytic end-member only. These TF-116 glasses are heterogeneous in terms of their trace element contents (e.g., 82-139 ppm Th; 31-55 ppm Nb; 469-718 ppm Zr) and are more enriched in incompatible trace element contents than the overlying phonolitic tephra layers (TF-107 and TF-111) ([Fig. 7a](#)). Ratios of HFSE to Th in these glasses remain constant, including Nb/Th ratio (0.41 ± 0.04 [2 s.d.]), Ta/Th (0.020 ± 0.001 [2 s.d.]) and Zr/Th (5.3 ± 0.4 [2 s.d.]) which all remain largely consistent with the overlying tephra (TF-107 and TF-111) ([Fig. 7b](#)). TF-125 also belongs to CG3, ranging from phono-trachytic to rhyolitic glasses, and this major element variability is captured by a large degree of trace element heterogeneity (e.g., 57-184 ppm Th; 1462-151 ppm Sr; 522-879 ppm Rb). Incompatible trace element concentrations observed in the phono-trachytic end-member glasses are consistent with TF-107 and TF-111 glasses. These TF-125 phono-trachytic glasses are more enriched in Sr, Ba and Eu relative to the rhyolitic end-member glasses, illustrating their compatibility during K-feldspar fractionation. Ratios of HFSE to Th in TF-125 glasses also differ between the phono-trachytic (Nb/Th = 0.39 ± 0.2 ; Zr/Th = 5.5 ± 0.3 ; Hf/Th = 0.13 ± 0.005 [2 s.d.]) and rhyolitic (Nb/Th = 0.30 ± 0.3 ; Zr/Th = 2.7 ± 0.7 ; Hf/Th = 0.07 ± 0.01 [2 s.d.]) end-members. Moreover, HFSE to Th ratios in the rhyolitic glasses show more variability than those of the phono-trachytic glasses, particularly in terms of Zr/Th, where Zr becomes depleted, probably driven by zircon fractionation. TF-126, previously reported in [Giaccio et al. \(2019\)](#), has a phono-trachytic composition and plots in CG-2. Incompatible trace element concentrations reveal a relatively homogeneous composition (e.g., 79 ± 7 ppm Th; 29 ± 1 ppm Nb; 393 ± 29 ppm Zr [2 s.d.]), and as such the ratios of HFSE to Th, show very limited variability, consistent with the homogeneous major element composition of the tephra (e.g., Nb/Th (0.37 ± 0.01 ; Ta/Th = 0.020 ± 0.001 ; Zr/Th = 4.9 ± 0.5 [2 s.d.])). Concerning the proximal pyroclastic deposits, the Castel Broco phonolitic glasses show a slight heterogeneity and are enriched in certain incompatible trace elements (e.g., 138-188 ppm Th [[Fig. 7a](#)]; 627-750 ppm ppm Zr; 30-42 ppm Y). Ratios of HFSE to Th remain constant within these glasses (Nb/Th = 0.32 ± 0.02 ; Zr/Th 4.1 ± 0.5 [2.d.]). Vico α trace element glass compositions are extremely heterogeneous (75-194 ppm Th; 1303-87 ppm Sr; 248-955 ppm Rb), consistent with their major element variability ranging from phono-trachytes to rhyolites ([Pereira et al., 2020](#)). The less evolved phono-trachytic glasses are more enriched in Sr, Ba and Eu relative to the rhyolitic end-member glasses; where these elements clearly behave compatibly during K-feldspar fractionation.

492 Ratios of HFSE to Th in these glasses also differ between the phono-trachytic (Nb/Th ~ 0.38; Zr/Th ~ 5.6) and
 493 rhyolitic (Nb/Th ~ 0.29; Zr/Th = 1.9-5.6) end-members. Vico β analyses focused on the predominantly rhyolitic
 494 sub-unit (VIG-3; [Pereira et al., 2020](#)); these rhyolitic glasses are relatively heterogeneous in the case of some
 495 incompatible elements (e.g., 137-169 ppm Th; 948-995 ppm Rb). Sr, Ba and Eu contents are more depleted
 496 in the rhyolitic glasses of Vico β than in Vico α .

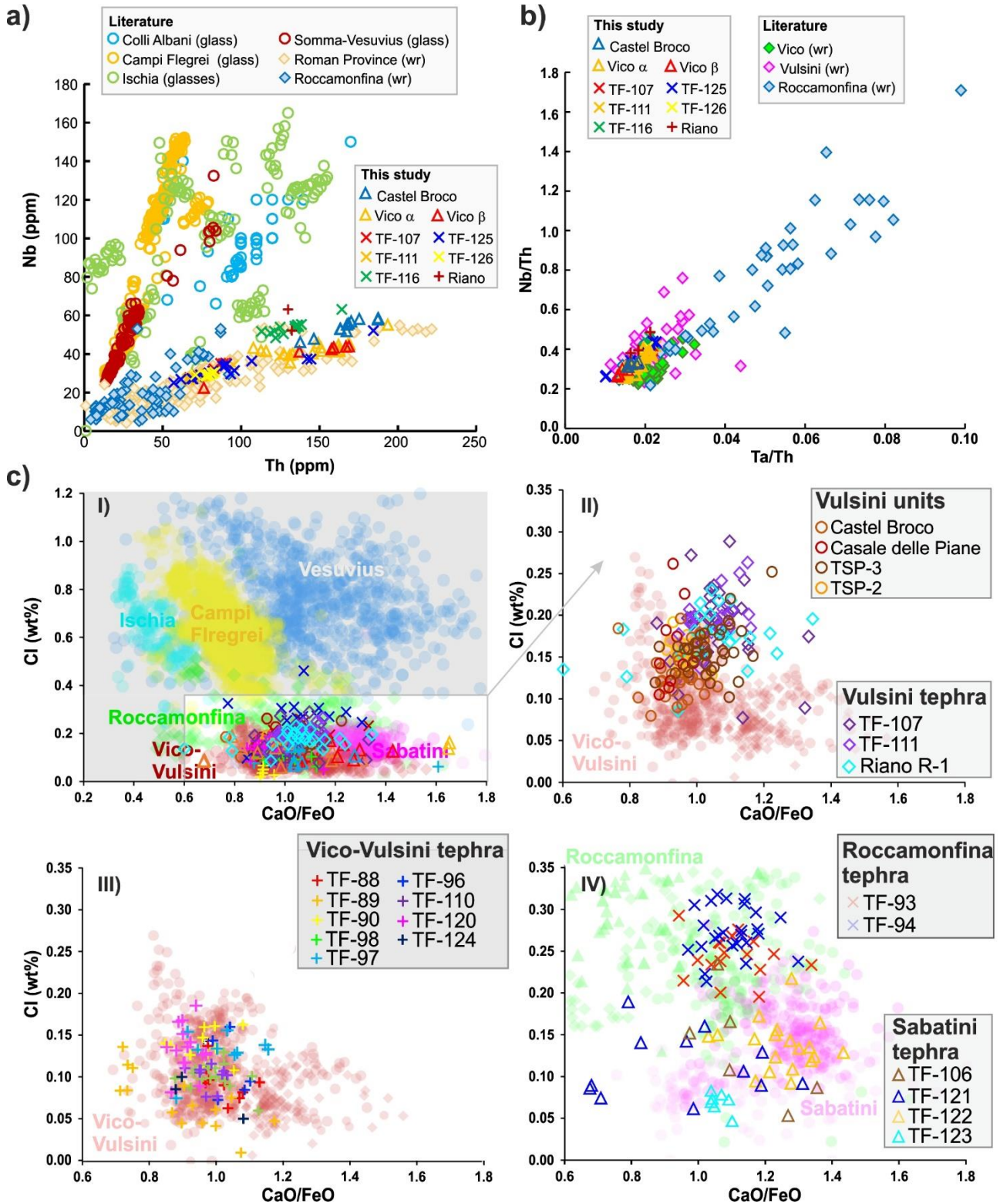


Figure 7. Discrimination diagrams for F4-F5 tephra. **a)** Th vs Nb bi-plot of the investigated tephra compared with literature data for the glasses of Neapolitan (i.e. Campi Flegrei, Somma-Vesuvius and Ischia) and Colli Albani volcanoes, which are characterized by a higher Nb/Th ratio than Roman/Latium (Vulsini, Sabatini, Vico) and Roccamonfina volcanoes; the compositions of the four tephra are compatible with either a Latium or Roccamonfina origin. **b)** Ta/Th vs Nb/Th discrimination diagram for Roccamonfina and Latium Volcanoes; the four tephra here investigated are characterized by a ratio compatible with either a Vulsini or Vico origin. Data source: TF-107, TF-111, TF-116 and TF-126: this study; literature data of whole rock (wr) compositions of products from Latium volcanoes and Roccamonfina: [Lustrino et al. \(2011\)](#) and references therein; glass composition of products from Colli Albani: [Cross et al., 2014](#); Ischia: [Tomlinson et al., 2014](#); Campi Flegrei: [Smith et al., 2011](#), [Tomlinson et al., 2012](#); Somma-Vesuvius: [Tomlinson et al., 2015](#). **c)** CaO/FeO vs Cl discriminating diagram of the volcanic sources of the Italian potassic trachyte-phonolite and tephriphonolite tephra (modified after [Giaccio et al., 2017](#)) for the F4-F5 and Riano R-1 tephra here shown in the Vulsini group for comparison. The compositions of the Vico and Vulsini pyroclastic units collected at Tuscania-San Pietro section, are also shown.

Only two successful analyses were obtained from the phonolitic Riano R-1 tephra, but the compositions are internally consistent for most incompatible elements, with the noticeable exception being the variable Nb content leading to a Nb/Th ratio of 0.39-0.48. Levels of incompatible trace element enrichment in the R-1 glasses (of unknown source area) appear more akin to those of Vulsini (e.g., Castel Broco), rather than Vico ([Fig. 7b](#)). Unfortunately, available trace element data for Sabatini are scant and cannot be considered here for comparison.

Ratios of HFSE to Th are seemingly useful when evaluating the origin of the five tephra layers characterised here in the context of peri-Tyrrhenian potassic volcanism, particularly given the limited trace element glass data available for some regional volcanic sources, and thus a reliance on whole-rock datasets, which are not always directly comparable to volcanic glass data (e.g., [Tomlinson et al., 2012](#)). It is clear that the Nb/Th ratios of the five Fucino layers analysed (TF-107, TF-111, TF-116, TF-125 and TF-126) preclude an origin from the Neapolitan volcanic zone (e.g., Campi Flegrei, Ischia, Vesuvius), where Nb values are far higher at overlapping Th content, and Nb/Th ratios are typically > 1.5 (glass datasets; [Fig. 7a](#)).

TF-107, TF-111, TF-116, TF-125 and TF-126 all have incompatible trace element concentrations and ratios of HFSE to Th compatible with the published analyses of the Latium and Roccamonfina volcanics ([Fig. 7a](#)). However, Roccamonfina appears an unlikely source of the five Fucino tephra layers owing to its typically higher Ta/Th ratios ([Fig. 7b](#)). In the investigated time-span, Colli Albani exclusively erupted K-foidites (CG-1) and can easily be discounted as the possible volcanic source of these Fucino layers, thus leaving the remaining Latium (Vulsini, Sabatini and Vico) volcanoes as the most obvious candidates. Indeed, ratios of HFSE to Th observed in TF-107, TF-111, TF-116, TF-125 and TF-126 are broadly consistent with those from published whole-rock (e.g., [Lustrino et al., 2011](#)) and our preliminary glass (reported above) data from Vulsini and Vico (although similarities to Sabatini products cannot be excluded owing to a paucity of data).

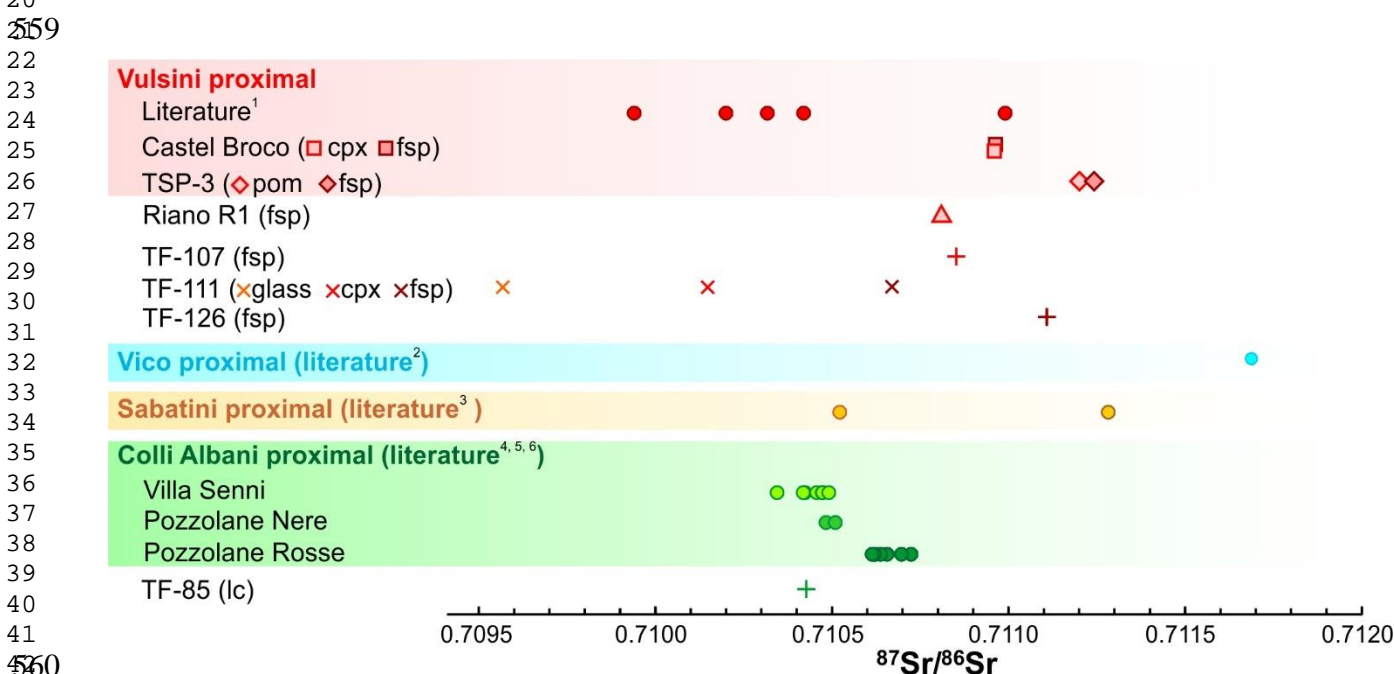
4.2.4. Strontium (Sr) Isotopes

Results for each analysed sample, along with associated uncertainty (2σ), are presented in [Table 5](#), while a comparison with values from the literature of proximal Vulsini, Vico, Sabatini and Colli Albani rock samples, erupted in the time interval 430-350 kyr, is shown in [Figure 8](#). In literature there are very few Sr-isotopic data (i.e., just one from [Perini et al., 2004](#)) for the Vico activity in the investigated 430-365 ka time interval, thus making it challenging to identify eruptive units from this volcano based on Sr-isotope signature. This knowledge gap should be filled in the future to better constrain the attribution of several TF tephra layers.

$^{87}\text{Sr}/^{86}\text{Sr}$ values were measured on either pyroxene or feldspar minerals on each sample, except for TSP-3, for which a matrix (pumice) measurement was obtained as well. For sample TF-85 a mineral fraction enriched in leucite crystals was analysed. The lowest value (0.7095) was measured on pumice fragments from the TF-111. Pyroxenes and feldspar from TF-111 are featured by $^{87}\text{Sr}/^{86}\text{Sr}$ ratio of 0.710149 and 0.710671,

545 respectively. The highest value (0.71120) was measured on feldspars of TSP-3. Therefore, all the measured
 546 ratios suggest a Roman province origin (Fig. 8) for the investigated tephra. Minerals from TF-85=Villa Senni
 547 have an $^{87}\text{Sr}/^{86}\text{Sr}$ ratio of 0.71043, which agrees with literature data (Gaeta et al., 2016). Measured values of
 548 proximal units from Vulsini (i.e., TSP-3 and Castel Broco) range up to 0.71125 (TSP-3 fsp), thus slightly
 549 extending the literature range for Vulsini (Fig. 8). The Riano R-1 tephra value of 0.71081 is broadly compatible
 550 with either a Sabatini or Vulsini source (rather than Vico). Finally, TF-126 has $^{87}\text{Sr}/^{86}\text{Sr}$ ratio of 0.71111 that
 551 would support the attribution of this tephra to a Vulsini eruption, as already suggested by Giaccio et al. (2019).

552
 553 Overall, the measured $^{87}\text{Sr}/^{86}\text{Sr}$ values do not provide sufficient evidence to be used as correlation tool for the
 554 Latium volcanoes, except for perhaps Vico: indeed, the amount of literature data on proximal samples is still
 555 too limited to allow solid attributions to a specific volcano. Nevertheless, the Latium volcanics, as previously
 556 known and confirmed by our data, show similar $^{87}\text{Sr}/^{86}\text{Sr}$ ranges, which are different from the products of other
 557 Italian volcanoes (e.g., Peccerillo, 2017). Thus, $^{87}\text{Sr}/^{86}\text{Sr}$ ratio can support an ascription of a tephra of unknown
 558 origin to the Latium volcanism, narrowing down the list of possible sources.



560
 561 **Figure 8.** $^{87}\text{Sr}/^{86}\text{Sr}$ ratio values of selected tephra layers and literature proximal references for the 430-350 ka time interval. Abbreviations:
 562 cpx=clinopyroxene; fs=feldspar; pom=pumice. Data source: TF-85, TF-107, TF-111, TF-126, Castel Broco, TSP-3, Riano R-1: this study;
 563 literature data: ¹ Peccerillo (2017); ² Perini et al. (2004); ³ Sottili et al. (2019); ⁴ Gaeta et al. (2006; 2016); ⁵ Giaccio et al. (2013a).

564
 565
 566 **Table 5.** $^{87}\text{Sr}/^{86}\text{Sr}$ ratio values of the selected four Fucino tephra and three proximal units.

Tephra/sample	Setting	Volcano	Glass composition	Analysed material	$^{87}\text{Sr}/^{86}\text{Sr}$	2 σ
TF-85	distal	Colli Albani	K-foidite	lc	0.710430	± 0.000007
TF-107	distal	Unknown	phonolite	fsp	0.710851	± 0.000006
				pum	0.709507	± 0.000006
TF-111	distal	Vulsini-Vico	phonolite	fsp	0.710671	± 0.000006
				cpx	0.710149	± 0.000007
				fsp	0.711105	± 0.000007
TF-126	distal	Vulsini	phonolite	fsp	0.711105	± 0.000007
Castel Broco	proximal	Vulsini	phonolite	cpx	0.710960	± 0.000006
				fsp	0.710965	± 0.000006
TSP-3	proximal	Vulsini	phonolite	pum	0.711199	± 0.000007
				fsp	0.711245	± 0.000006
Riano R-1	mid-proximal	Vulsini	phonolite	K-fsp	0.710810	± 0.000007

567 Abbreviations: K-fsp=K-feldspar; fsp=feldspar; cpx=clinopyroxene; pum=pumice.

568

569 **4.3. ⁴⁰Ar/³⁹Ar age of TF-85, TF-117 and Pozzolane Nere**

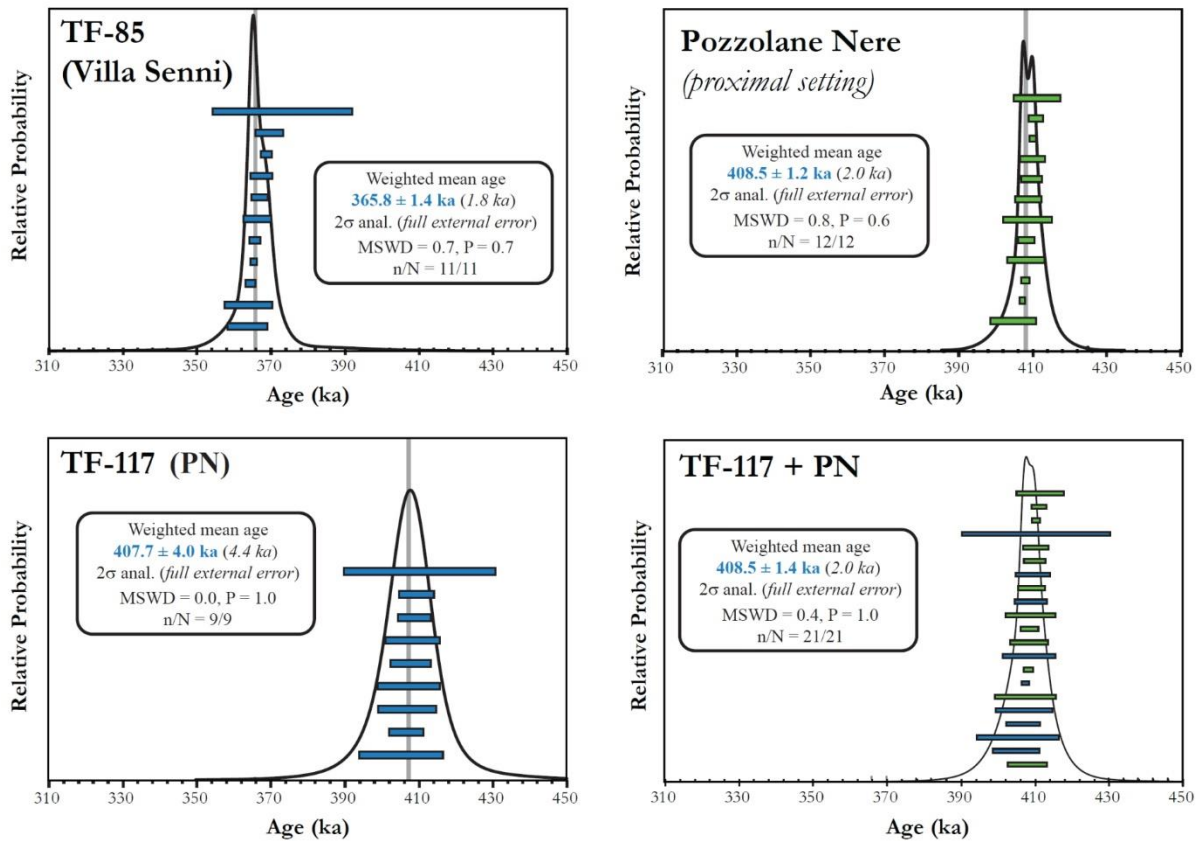
570 The results for each dated deposit are presented as probability diagrams in Figure 9. Reported uncertainties
571 are analytical at a 95.5% of confidence limit (J-value included), as well as fully propagated ones. Detailed
572 analytical data are available in Supplementary dataset 3 (SD-3).

573 **TF-85 (Villa Senni):** A total of eleven leucite single crystals were dated. All crystals yielded an
574 undistinguishable age, allowing us to calculate a meaningful weighted mean age of 365.8 ± 1.4/1.8 ka (MSWD
575 =0.7, P=0.7).

576 **TF-117 (Pozzolane Nere):** Nine leucite crystals were individually dated. All crystals yielded an
577 undistinguishable age, allowing the straightforward calculation of a weighted mean age of 407.7 ± 4.0/4.4 ka
578 (MSWD =0.04, P=1.0).

579 **Pozzolane Nere (Rome proximal setting):** Twelve leucite crystals were dated. They all share a similar age
580 within uncertainties, allowing us to calculate a statistically meaningful weighted mean age of 408.5 ± 1.2/2.0
581 ka (MSWD =0.8, P=0.6). In Figure 9 we also combined the 21 single leucite ages obtained on the Pozzolane
582 Nere from both the proximal deposits and distal equivalent, allowing us to propose a new, more precise
583 weighted mean age of 408.5 ± 1.4/2.0 ka (MSWD =0.4, P=1.0) for the Pozzolane Nere regional marker.

584



585

586 **Figure 9.** ⁴⁰Ar/³⁹Ar on single grain results (leucite crystals), presented as probability diagrams, for TF-85 (Villa Senni), TF-117 (Pozzolane
587 Nere) and Pozzolane Nere (Rome proximal setting). A combined weighted mean age of TF-117/Pozzolane Nere is then proposed. Ages
588 are calibrated according to Renne et al. (2011) total ⁴⁰K decay constant and from the optimization calibrated age of 1.1891 Ma for the flux
589 standard ACs-2 (Niespolo et al., 2017). Individual crystal error bars are at 1σ of uncertainties.

590

591

592

593

594

591 5. Discussion

592 5.1. Volcanic sources of tephra layers from core F4-F5

593 5.1.1. K-foidites (CG-1)

594 The K-foidite compositions of the two tephra layers from CG-1 (Fig. 6) are distinctive within the context of
595 Quaternary Italian volcanism, being limited to a few eruptive sources (e.g., Peccerillo, 2017). Among these,
596 the Colli Albani volcanic district has produced and dispersed several K-foiditic tephra (e.g., Marra et al., 2009)
597 from moderate to major eruptions that have been traced in both distal and ultra-distal settings (e.g., Giaccio et
598 al., 2013a, 2014; Petrosino et al., 2014b, Leicher et al., 2016). Consequently, Colli Albani should be regarded
599 as the most likely source of TF-100 and TF-108.

600 5.1.2. Potassic phonotephrites, tephriphonolites, phonolites, trachytes, trachy-phonolites and latites (CG2)

601 The glass geochemical compositions of tephra from CG-2 (i.e., potassic phonotephrites, tephriphonolites,
602 phonolites, trachytes, trachytes-phonolites and latites) are quite common and shared by almost all peri-
603 Tyrrhenian potassic volcanoes of central-southern Italy (e.g., Peccerillo, 2017). However, considering the time
604 interval investigated here (430-365 ka), we can confidently exclude the Neapolitan volcanoes (i.e., Ischia,
605 Procida, Campi Flegrei and Somma-Vesuvius) as possible sources of any of the twenty CG-2 tephra layers,
606 since the so-far oldest known eruption from these volcanoes is significantly younger (i.e., the $\sim 289.6 \pm 1.9$ ka
607 Seiano Ignimbrite; De Vivo et al., 2001; Rolandi et al., 2003; Belkin et al., 2016; Fig. 3). Nevertheless, a
608 geochemical fingerprinting approach remains essential, as there is always the possibility that Neapolitan
609 volcanism may be extended deeper in time with future investigations, particularly since some distal archives
610 might seem to suggest older activity in the region (e.g., Giaccio et al., 2014; Petrosino et al., 2015).

611 In order to discriminate the source of this large group of tephra, we employed the CaO/FeO vs Cl diagram
612 (Giaccio et al., 2017), which defines quite distinct fields for the individual sources of the Latium and Neapolitan
613 pyroclastic rocks with a SiO₂ content ranging from 52 wt% to 67 wt% (Fig. 7c-I). This confirms the lack of
614 products from the Neapolitan volcanoes and points to the Latium or Roccamonfina volcanoes as the only
615 plausible sources of 17 out of 21 CG-2 Fucino tephra (Fig. 7c-I). Furthermore, the trace element compositions
616 of all the phonolite and trachyte glass shards from the CG-2 (and CG-3) tephra layers also clearly precludes
617 the Neapolitan volcanoes as possible eruptive sources (Fig. 7a-b).

618 **Vulsini** – The Cl contents of TF-107 and TF-111 plot at the boundary between Vulsini-Vico and Roccamonfina
619 fields (Fig. 7c-II). However, these tephra layers can be tentatively attributed to the Vulsini, considering their
620 compositional match in the CaO/FeO vs Cl diagram with the Vulsini proximal pyroclastic units analysed in the
621 present study (especially TSP-3 Pumice fall from Tuscania-San Pietro section; Fig. 7c-II; Table 4),
622 Furthermore, though considering the paucity of the proximal reference dataset, ⁸⁷Sr/⁸⁶Sr ratios also support a
623 Vulsini origin for these two tephra (Fig. 8), while the trace elements confirm an origin from Roman (Vulsini or
624 Vico) volcanoes (Fig. 7b). The Riano R-1 tephra (404.7 ± 5.0 ka; Marra et al., 2018), for which a clear
625 stratigraphic/compositional correlation is still lacking, also matches the compositions of the Vulsini units
626 analysed in this study. It is therefore compatible with a possible distal origin from Vulsini, rather than from the
627 nearest Sabatini source.

628
629
630

60
61
62
63
64
65

631 **Vulsini-Vico** – Cl contents and CaO/FeO ratios of TF-88, TF-89, TF-90, TF-96, TF-97, TF-98, TF-110, TF-
 632 120 and TF-124 are consistent with either Vico or Vulsini compositions, and thus do not allow a further
 633 discrimination between these two potential sources (Fig. 7c-III). However, a discrimination between these two
 634 potential sources is possible based on further oxides composition as discussed in section 5.2.3.4.

635
 636 **Sabatini** – According to the CaO/FeO vs Cl diagram, TF-106 and TF-122 can be related to the Sabatini
 637 Volcanic District based on the high (i.e., >1.15) CaO/FeO ratio (Fig. 7c-IV). TF-106 forms along with TF-102,
 638 TF-103 and TF-104 a well-defined cluster of tephra that share a similar phono-tephritic composition (Fig. 6;
 639 Supplementary dataset SD-1) and lithology (Table 3). Therefore, though the CaO/FeO vs Cl discrimination
 640 diagram cannot be applied to TF-102, TF-103 and TF-104 because of their SiO₂ content being lower than 52
 641 wt%, (Giaccio et al., 2017), they can be reliably regarded as part of a cluster of eruptions from Sabatini.
 642 Although showing a more scattered composition in the CaO/FeO vs Cl diagram (Fig. 7c-IV), TF-121 can be
 643 attributed to the Sabatini as well, because of its close geochemical similarity with the directly underlying TF-
 644 122 layer (Fig. 5). Finally, TF-123 can be also likely attributed to the Sabatini, because of its homogenous
 645 composition in the CaO/FeO vs Cl diagram that matches a second well-defined compositional cluster of the
 646 Sabatini rock types (Fig. 7c-IV).

647
 648 **Roccamonfina** – TF-93 and TF-94 can be confidently attributed to the Roccamonfina volcano, based on the
 649 relatively high Cl content (i.e., >0.25 wt%), and thus their clear position in Roccamonfina field of the the
 650 CaO/FeO vs Cl diagram (Fig. 7c-IV), which is quite distinctive with respect to the Latium volcanoes (Fig. 7c-
 651 IV). (Fig. 7c-IV).

652 5.1.3. *K-rhyolites (CG-3)*

653 The six tephra layers forming CG-3 (TF-99, 109, 114, 115, 116, 125; Fig. 6) show K-rich rhyolitic and trachy-
 654 rhyolitic compositions, which is quite unusual within the context of the peri-Tyrrhenian Quaternary Italian
 655 volcanism, and peculiar to the Vico volcano (e.g., Perini et al., 1997, 2000, 2003, 2004; Perini and Conticelli,
 656 2002; Pereira et al., 2020), hence the most probable source of the Fucino CG-3 tephra layers.

657 In summary, based on distinctive chemical compositions, stratigraphic clues and lithological features and
 658 affinities, we propose a correlation among the Fucino tephra layers and the peri-Tyrrhenian potassic
 659 volcanoes, as summarized in Table 6.

660 **Table 6.** Volcanic sources of the investigated Fucino tephra, inferred from glass chemical composition and lithological features.

Volcano	Fucino tephra
Vulsini	TF-107, TF-111
Vico	TF-99, TF-109, TF-114, TF-115, TF-116, TF-125
Vulsini or Vico	TF-88, TF-89, TF-90, TF-96, TF-97, TF-98, TF-110, TF-120, TF-124
Sabatini	TF-102, TF-103, TF-104, TF-106, TF-121, TF-122, TF-123
Colli Albani	TF-100, TF-108
Roccamonfina	TF-93, TF-94

667 **5.2. Individual tephra correlation**

668 5.2.1. *Tephra from Colli Albani (CG-1).*

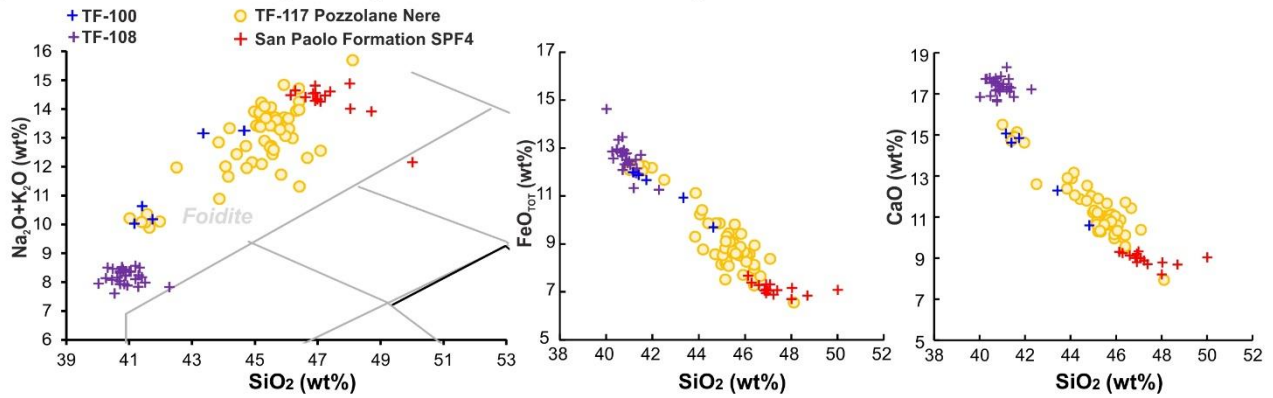
669 **TF-100 and TF-108** - These two K-foiditic tephra layers (CG-1), ascribed to the Colli Albani activity, occur
670 between TF-85 and TF-117 (Fig. 2), which were attributed to the Villa Senni (365.8 ± 1.4 ka) and Pozzolane
671 Nere (408.5 ± 1.4 ka) eruptions, respectively (Giaccio et al., 2019). The $^{87}\text{Sr}/^{86}\text{Sr}$ composition determined in
672 this study for TF-85 further supports its attribution to the Villa Senni eruption. Indeed, $^{87}\text{Sr}/^{86}\text{Sr}$ ratios of the
673 Colli Albani products show a strong time-dependent variability (Gaeta et al., 2006, 2016; Giaccio et al., 2013a)
674 and the $^{87}\text{Sr}/^{86}\text{Sr}$ value obtained for TF-85 precisely matches that of Villa Senni (Fig. 8).

675 Considering the available chronological constraints and its relative proximity to the TF-117/Pozzolane Nere,
676 TF-108 can be attributed to the post-caldera phase of the Pozzolane Nere eruptive cycle (*sensu* Gaeta et al.,
677 2016), which is equivalent to the Centogocce fall succession of Giordano et al. (2006). In proximal settings,
678 the Centogocce deposits consist in a series of scoria lapilli fall beds and lava flows overlying the Pozzolane
679 Nere deposits, emplaced in the 403.4 ± 5 ka - 396.4 ± 5 ka time interval (recalculated ages from Marra et al.,
680 2009 and Gaeta et al., 2016). Unfortunately, no glass composition is available for this scoria fall succession,
681 and therefore, we used the composition of TF-117/Pozzolane Nere for comparison (Fig. 10a). Furthermore,
682 Pereira et al. (2020) have recently reported the occurrence, within the San Paolo Formation aggradational
683 succession, of a tephra layer (SPF4), with a polymodal rhyolite, K-foidite and phonotephrite composition,
684 interpreted as a reworked volcanoclastic layer containing both Vico and Colli Albani eruption products. Pereira
685 et al. (2020) reported an age of 403.5 ± 4.2 ka for SPF4, which is consistent with the time interval (403.4 ± 5
686 ka - 396.4 ± 5 ka) covered by the Centogocce fall succession, in spite of a geochemical mismatch of TF-108
687 with SPF4 (Fig. 10a), which can be expected for multiple explosive and effusive eruptions occurred during a
688 relatively long interval. Based on glass composition and stratigraphic position relatively to the TF-
689 117/Pozzolane Nere, we attribute TF-108 to the Centogocce activity. The stratigraphic position of TF-100,
690 between the TF-117/Pozzolane Nere and the TF-85/Villa Senni (Fig. 2), suggests an age substantially younger
691 than the Centogocce equivalent TF-108. In spite of this, for its composition, which partially overlaps the wide
692 composition field of the Pozzolane Nere (Fig. 10a), TF-100 could be considered still as part of the final stage
693 of the Pozzolane Nere eruptive cycle.

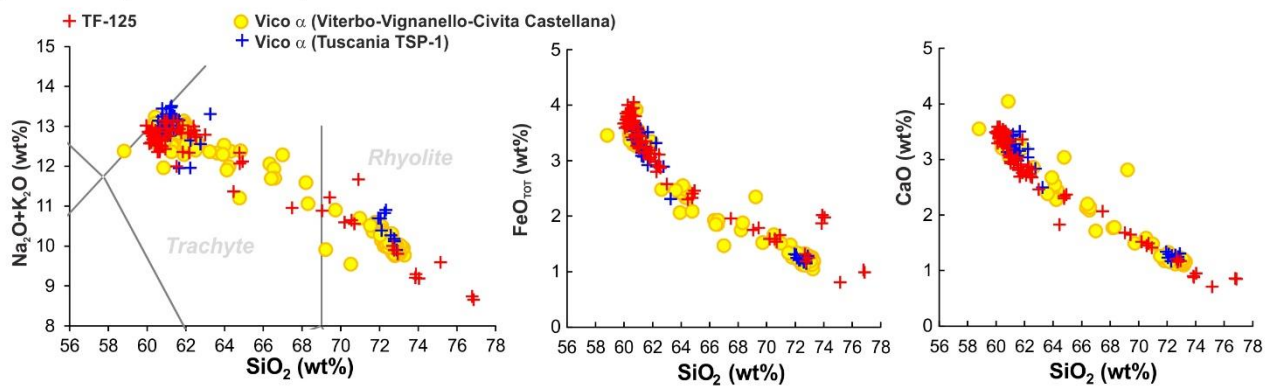
695 5.2.2. *Tephra from Vico (CG-3).*

696 **TF-125** - This tephra occurs in the lowermost portion of the F4-F5 record, ~50 cm upsection from TF-126 that
697 was directly dated at 424.3 ± 3.2 ka (Giaccio et al., 2019). TF-125 is characterized by a heterogeneous
698 trachyte-rhyolite composition, with a silica content ranging from 59 wt% to 77 wt% and an alkali content from
699 14 wt% to 8 wt%. Recently, Pereira et al. (2020) published new glass geochemical compositions for the early-
700 emplaced volcanics of Vico activity (Vico Period I; Perini et al., 2004), including Vico α and Vico β Plinian fall
701 markers (Cioni et al., 1987), both with a dominant rhyolitic composition, along with the characterization of three
702 minor events (i.e., Vico β_{top} , Vico γ and Vico δ ; Cioni et al., 1987). In addition, Pereira et al. (2020) acquired
703 very precise $^{40}\text{Ar}/^{39}\text{Ar}$ ages for Vico α (414.8 ± 2.2 ka), Vico β (406.5 ± 2.4 ka), Vico β_{top} (406.4 ± 2.0 ka) and
704 Vico δ (399.7 ± 3.0 ka).

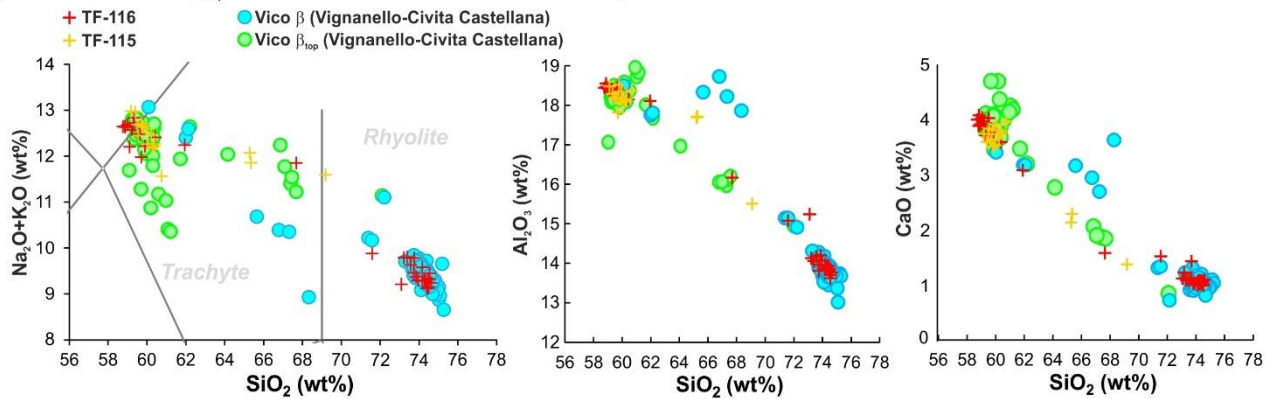
a) *Colli Albani Centogocce (402.7±5.0-396.7±5.0 ka)*



b) *Vico α (414.8±2.2 ka)*



c) *Vico β-Vico β_{top} (406.5±2.4 ka - 406.2±2.0 ka)*



d) *Vico γ (>399.7±3.0, < 406.2±2.0 ka)*

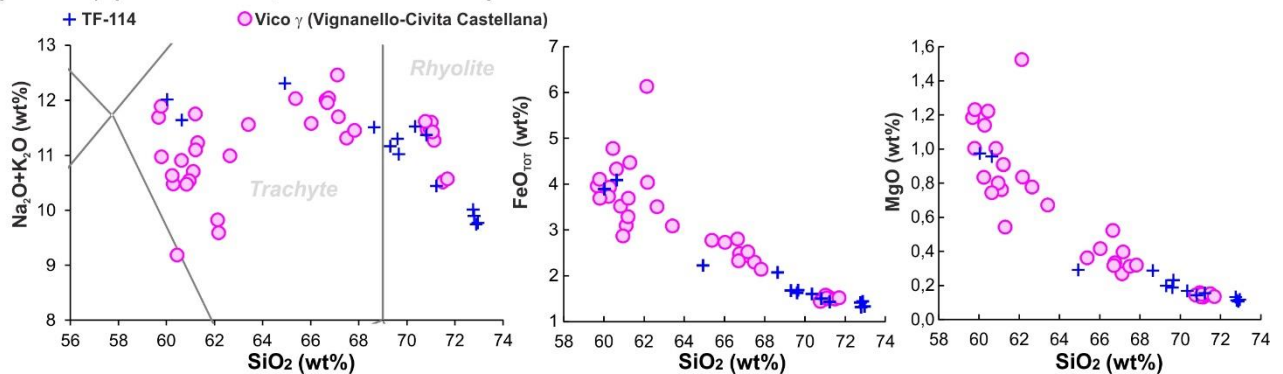


Figure 10. Total alkali versus silica (TAS) classification diagram after [Le Maitre et al. \(2002\)](#) and representative bi-plots for TF-100, TF-108, TF-114, TF-115, TF-116 and TF-125 from the F4-F5 teptra record, compared with SPF4 tephra layer from the San Paolo aggradational succession, Pozzolane Nere (TF-117), proximal Vico α, Vico β, Vico β_{top} and Vico γ units from Vico volcano. Data source: WDS glass composition of TF-100, TF-108, TF-114, TF-115, TF-116, TF-125 and Vico α (TSP-1): this study; WDS glass composition of TF-

711 117/Pozzolane Nere: [Giaccio et al. \(2017\)](#); WDS glass composition and $^{40}\text{Ar}/^{39}\text{Ar}$ age of tephra SPF4, Vico α , Vico β , Vico β_{top} and Vico
712 γ , sampled at Viterbo (VT), Civita Castellana (CC) and Vignanello (VIG): [Pereira et al. \(2020\)](#). $^{40}\text{Ar}/^{39}\text{Ar}$ ages are recalculated relative to
713 an age of 1.1891 Ma for the Alder Creek sanidine monitor standard ([Niespolo et al., 2017](#)), with the uncertainty expressed at 2σ .
714

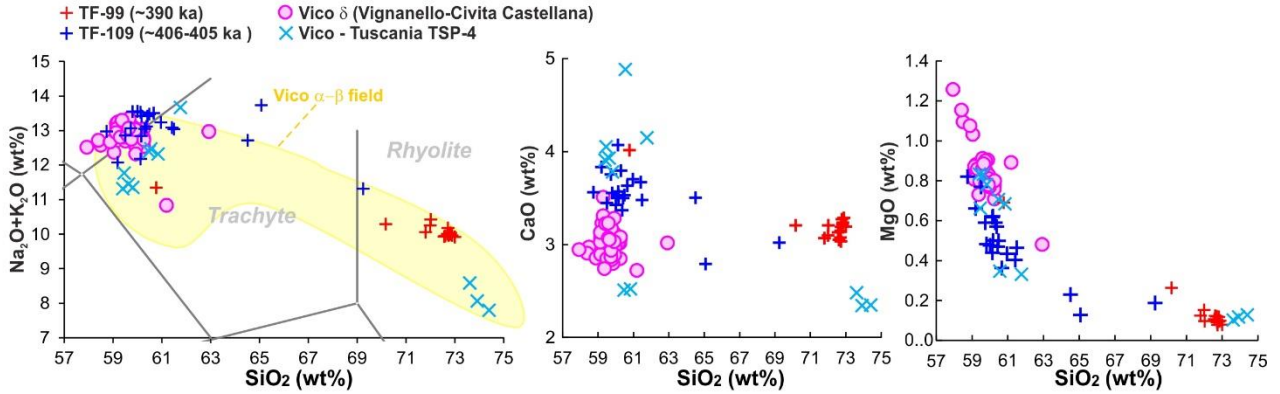
715 Using this updated geochemical dataset for the Vico Period I products, we found that TF-125 major element
716 composition matches that of Vico α of [Pereira et al. \(2020\)](#) and of Tuscania-San Pietro TSP-1 (this study; [Fig.](#)
717 [10b](#)), and this correlation is further strengthened by the similarities in the trace element glass compositions
718 obtained here for Vico- α and TF-125 ([Fig. 11a](#)). Considering this geochemical affinity and its stratigraphic
719 position between TF-126 (424.3 ± 3.2 ka) and TF-117/Pozzolane Nere (408.5 ± 1.4 ka), consistent with an
720 age of 414.8 ± 2.2 ka, we can confidently correlate TF-125 to the Vico α Plinian eruption.
721

722 **TF-116 and TF-115** – TF-116 is located less than 1 m upsection from TF-117, the latter dated at 407.7 ± 4.0
723 ka and correlated to the Pozzolane Nere eruption ([Giaccio et al., 2019](#)), which has been dated here more
724 precisely at 408.5 ± 1.4 ka ([Fig. 9](#)). Like TF-125, this tephra is characterized by a heterogeneous trachytic-
725 rhyolitic composition, with a dominant SiO_2 -rich (>75 wt%) rhyolitic component, and a minor scattered
726 phonolitic-trachytic one (58-68 wt% SiO_2), which is a distinctive, common features of the Vico Period I units
727 ([Pereira et al., 2020](#)). Trace element analyses ([Fig. 7a-b](#)) also support a Latium origin for this tephra.
728 Specifically, the glass rhyolitic composition of TF-116 matches that of Vico β ([Fig. 10c](#)) that, along with its
729 position on top of TF-117/Pozzolane Nere, allows us to correlate TF-116 to Vico β eruption (406.5 ± 2.4 ka;
730 [Pereira et al., 2020](#)). Noteworthy, TF-116 contains a significant trachyte-phonolite component that is poorly
731 represented or documented in proximal settings ([Fig. 10c](#)).

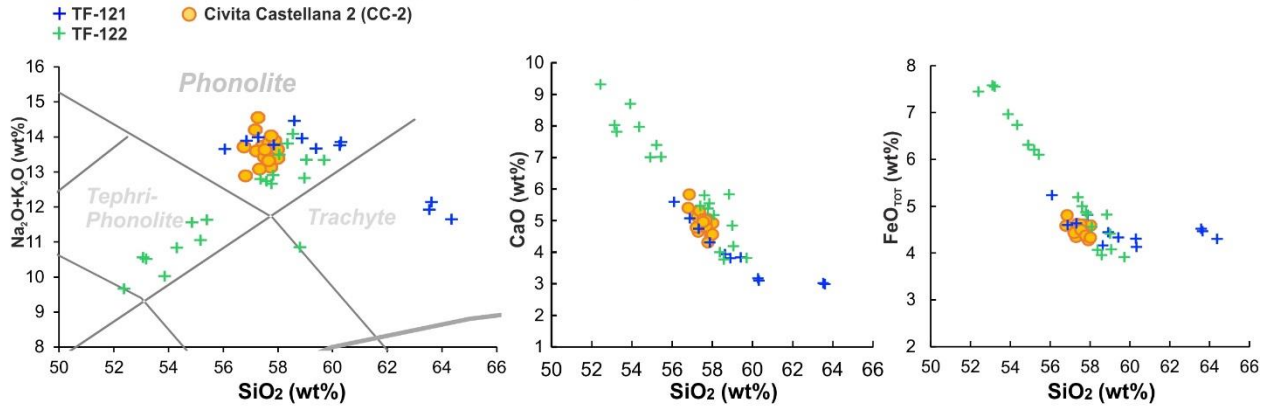
732 TF-115 tephra is found 2 cm above TF-116 and is characterized by a heterogeneous composition, consisting
733 of a main phonolitic-trachytic component (SiO_2 59-66 wt%) and a minor SiO_2 -rich (~ 69 wt%) rhyolitic one.
734 These geochemical features allow unambiguous correlation to Vico β_{top} ([Fig. 10c](#)), consistent with the
735 superposition of the tephra just on top of TF-116/Vico β . Furthermore, consistent with its strict stratigraphic
736 proximity to TF-116/Vico β , the proximal Vico β_{top} has a $^{40}\text{Ar}/^{39}\text{Ar}$ age of 406.5 ± 2.4 ka that is indistinguishable
737 from that of Vico β ([Pereira et al., 2020](#)). Noteworthy, [Pereira et al. \(2020\)](#) also pointed out that the combined
738 glass composition of Vico β and Vico β_{top} is to some extent similar to that of Vico α , so that, in the absence of
739 strong chronological and/or tephrostratigraphic constraints, the geochemical composition of the two units could
740 be potentially confused. However, in the F4-F5 record, the TF-115 and TF-116 couplet occurs on top of the
741 408.5 ± 1.2 ka Pozzolane Nere tephra, well upsection from the Vico α correlative (TF-125). Furthermore, when
742 dealing with sedimentary archives not so well constrained chrono-stratigraphically as Fucino, trace element
743 analysis of the Vico eruption products may offer useful means to discriminate the distal equivalents of Vico α
744 and Vico β . In fact, the phono-trachytic end-member glasses of TF-116/Vico β extend to greater levels of
745 incompatible trace element enrichment with respect to TF-125/Vico α ([Fig. 11a](#)), whilst the analysis of
746 proximal and distal Vico rhyolitic products reveals greater depletions in Sr, Eu associated with the Vico β tephra
747 ([Fig. 11b](#)). In conclusion, the general stratigraphic, chronological and geochemical features of TF-116 and TF-
748 115 consistently support their unambiguous attribution to Vico β and Vico β_{top} , respectively.
749

750 **TF-114** - This tephra is separated from the underlying TF-115 by 2-cm-thick lacustrine sediments. It is
751 characterized by a heterogeneous trachyte-rhyolite composition, with a silica content ranging from 60 to 73
752

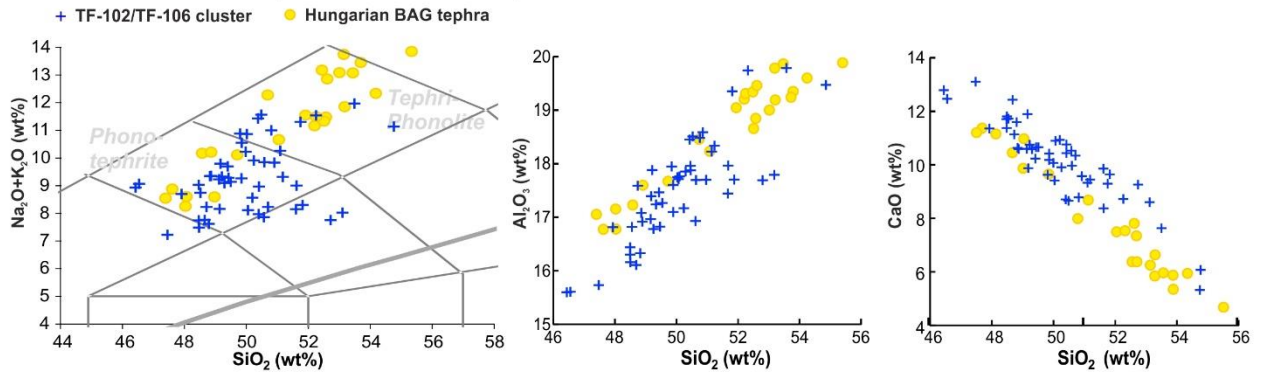
a) *Vico unknown (~406-405 ka - ~390 ka)*



b) *Sabatini Civita Castellana 2 (>408.5, <415 ka)*



c) *Sabatini unknown (>390 ka, <405 ka)*



d) *Roccamonfina Mt. Ophelio-Mt. Capitulo (398.5±18.0 ka - 385.6±16.0 ka)*

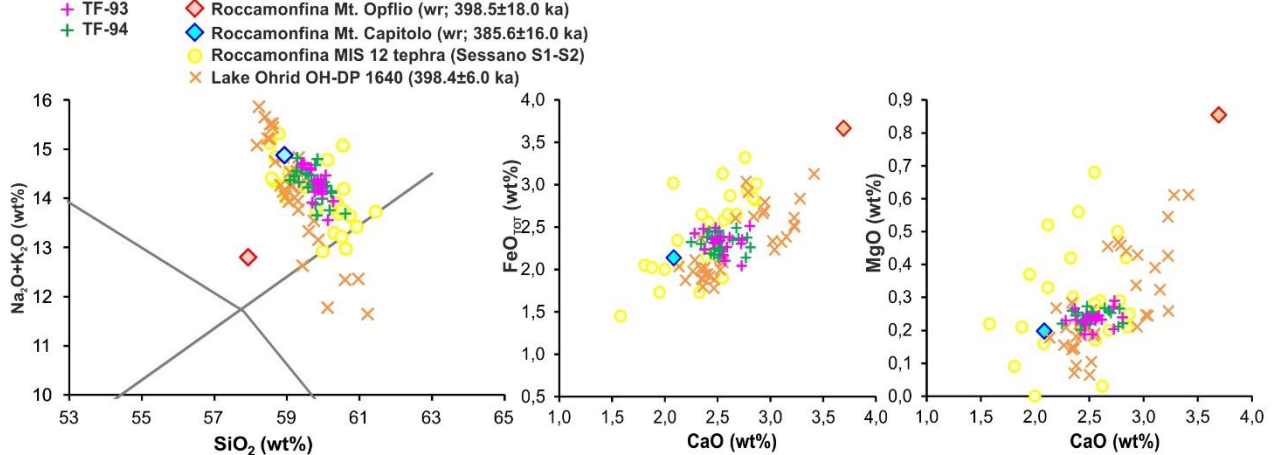


Figure 12. TAS diagram after Le Maitre et al. (2002) and representative bi-plots for the tephra TF-93, TF-94, TF-99, TF-102, TF-103, TF-104, TF-106, TF-109, TF-121 and TF-122 from the F4-F5 record, compared with proximal Vico δ units from Vico volcano, TSP-4 from

772 Tuscania-San Pietro succession, CC-2 from Civita Castellana succession, the distal Bag tephra from the MIS 10 Hungarian loess, tephra
773 OH-DP-1640 from Lake Ohrid and Sessano-1 and 2 (S1-S2) tephra from Sessano basin. For comparison, in panel a), the compositional
774 field of the major Vico α and Vico β Plinian eruptions is also shown. Data source: WDS glass composition of TF-93, TF-94, TF-99, TF-
775 102, TF-103, TF-104, TF-106, TF-109, TF-121, TF-122, TF-123, and TSP-4: this study; WDS glass composition and $^{40}\text{Ar}/^{39}\text{Ar}$ age of Vico
776 δ and CC-2, sampled at Vignanello (VIG) and Civita Castellana (CC), respectively: [Pereira et al., 2020](#); WDS glass composition and
777 modelled age of tephra OH-DP-1640: [Leicher et al. \(2019\)](#); WDS glass composition and of Bag tephra: [Pouclet et al. \(1999\)](#); post-Rio
778 Rava – pre-Brown Leucitic Tuff whole-rock compositions: [Rouchon et al. \(2008\)](#); S1 and S2 SEM-EDS glass composition: [Russo Ermolli
779 et al. \(2010\)](#). $^{40}\text{Ar}/^{39}\text{Ar}$ ages are recalculated relative to an age of 1.1891 Ma for the Alder Creek sanidine monitor standard ([Niespolo et
780 al., 2017](#)), with the uncertainty expressed at 2σ .

781
782 **TF-99 and TF-109** - TF-99 has a predominantly homogeneous rhyolitic composition (70-73 wt% of SiO_2) with
783 a single trachytic shard (60 wt% SiO_2), while TF-109 is characterized by a heterogeneous trachytic composition
784 (59-65 wt% SiO_2) with a minor rhyolitic component (one shard with ~69 wt% SiO_2 ; Fig. 12a). As stated in
785 section 5.1.3, the occurrence of a rhyolitic component in these tephra makes their attribution to the Vico
786 volcano quite straightforward, because it is the only known Middle Pleistocene peri-Tyrrhenian volcanic source
787 that produced K-rich rhyolitic tephra. Indeed, in the TAS diagram, both tephra plot within the compositional
788 field of the Vico α and Vico β Plinian eruptions (Fig. 12a).

789 Considering the stratigraphic position of TF-99 and TF-109 within the F4-F5 record, the most plausible
790 candidate for at least one of these tephra layers would be Vico δ , dated at 399.7 ± 3.0 ka ([Pereira et al., 2020](#)).
791 However, neither TF-99 nor TF-109 match Vico δ in composition (Fig. 12a). Although in the TAS diagram TF-
792 109 would seem compatible with Vico δ , suitable bi-plot diagrams show significant differences on several
793 oxides (e.g., CaO content; Fig. 12a). On the other hand, the geochemical composition of TF-109 is consistent
794 with the TSP-4 unit of the Tuscania-San Pietro succession (Fig. 12a). Thus, TF-109/TSP-4 and TF-99 can be
795 only generically attributed to the Vico Period I, their proximal equivalents at Vico not yet identified.

796 5.2.3. Tephra of Compositional Group-2 (CG-2)

797 5.2.3.1. Sabatini tephra

798
799 **TF-102, TF-103, TF-104, TF-106, TF-121, TF-122 and 123** - The geochemical composition of the TF-102/106
800 and TF-121/122 clusters are quite heterogeneous, with a SiO_2 content ranging from 46 wt% to 55 wt% and
801 from 52 wt% to 64 wt%, respectively (Fig. 12c and 12b, respectively). TF-123 shows instead a homogenous
802 high-alkali tephriphonolitic composition (Fig. 6).

803
804 The TF-102/106 cluster occurs just on top of TF-108, thus constraining its position close to the Centogocce
805 succession time interval (403.4 ± 5 ka - 396.4 ± 5 ka). TF-121/122 and TF-123 occur instead between TF-125
806 (Vico α , 414.8 ± 2.2 ka; [Pereira et al., 2020](#)) and TF-118 (Fontana Ranuccio, 407.0 ± 4.2 ka; [Pereira et al.,
807 2018](#)), or the more precisely dated TF-117/PN (408.5 ± 1.2 ka), constraining their ages in the narrow time
808 interval between ~415 ka and ~408 ka. Hence, both the TF-102/106 and TF-121/122 clusters and TF-123 can
809 be attributed to the Southern Sabatini activity (Fig. 3; [Sottili et al., 2004, 2010](#)), which was characterized by
810 the emplacement of widespread sub-Plinian to Plinian fall deposits in the time interval ~500-380 kyr ([Marra et
811 al., 2014, Sottili et al., 2019](#)).

812 Though no relevant activity is documented in the ~414-402 ka time-span of TF-121/122 and TF-102/106
813 clusters, recent investigations point to the occurrence of a previously unrecognized Sabatini unit
814 chronologically and geochemically consistent with TF-121/122 ([Pereira et al., 2020](#)). Specifically, at Civita
815 Castellana (Fig. 1b), [Pereira et al. \(2020\)](#) described a ~1 m-thick pumice fall unit (CC-2), phonolitic in
816 composition and tentatively ascribed it to Sabatini activity, sandwiched between Vico α (414.8 ± 2.2 ka; CC-1)
817 and Vico β (406.5 ± 2.4 ka; CC-3), i.e., a similar stratigraphic position of TF-121/122 within the F4-F5

818 succession. This unit was also found at San'Abbondio section (Fig. 1b) immediately on top of Vico α (Pereira
819 et al., 2020). Although more variable, in terms of geochemical composition, both TF-121 and TF-122 are
820 compatible with CC-2 phonolitic glass composition (Fig. 12b). Among the two layers, the thickest TF-121
821 seems to show a higher degree of geochemical similarity, and thus is a good candidate for correlation with
822 CC-2 pumice fall, while the thinner TF-122 could represent a minor eruption slightly preceding CC-2 fall.
823 In contrast, TF-123, whilst sharing a broadly similar chrono-stratigraphic position to they overlying TF-121/122
824 deposits, shows no geochemical similarity to the CC-2 pumice fall and thus has to be considered the product
825 of a slightly older, unknown Sabatini eruption.

826 Similarly, the TF-102/106 cluster has no chronological and stratigraphical relative in the currently
827 determined Sabatini proximal eruption record. This cluster would be instead chronologically consistent with
828 the activity of the Volsci volcanic field and specifically with Pofi Scoria cone and Amafi scoria cone, dated at
829 394.4 ± 3.5 ka and 395.8 ± 6.1 ka (Marra et al., 2021), respectively, likely equivalent to the Cava Pompei scoria
830 fall (392.7 ± 3.0 ka) and Isoletta I scoria fall (401.7 ± 3.0 ka) (Pereira et al., 2018). However, the lack of any
831 geochemical glass compositional data currently prevents any possible comparison and correlation with TF-
832 102/106.

833 In contrast, in the ultra-distal setting, the TF-102/106 cluster would be geochemically and chronologically
834 compatible with the so-called Bag Tephra (Fig. 12c), interbedded in Quaternary loess deposits of Hungary and
835 Slovakia (Poulet et al., 1999; Hum, 2005; Sági et al., 2008). In fact, the Bag Tephra has a phonotephritic-
836 tephriphonolitic glass composition (Poulet et al., 1999) very similar to that of the TF-102/106 cluster (Fig.
837 12c). The Bag tephra is commonly found below the so-called Basaharc Lower paleosol of the MIS 9 period
838 (Horváth and Bradák, 2014), thus consistent with the age of TF-102/106. The previous tentative correlation to
839 the Villa Senni eruption (Poulet et al., 1999) is ruled out by glass geochemistry. More recent petrographic
840 investigations (Sági et al., 2008) point out that the Bag tephra likely represents multiple tephra layers.
841 Therefore, the tephra cluster TF-102/106 would be a good candidate for a correlation with such an important
842 marker of the Hungarian loess. However, at present we can only propose a tentative correlation with either an
843 unknown Sabatini eruption cluster or the Pofi Scoria and Amafi centers of the Volsci volcanic field.

844 5.2.3.2. Roccamonfina tephra

845 **TF-93 and TF-94** – Both tephra layers are characterized by an almost homogeneous phonolitic composition,
846 with a SiO₂ content of ~59-61 wt% and alkali content ranging between ~13.5 and ~14.5 wt%. Considering their
847 position within the F4-F5 succession, between TF-85 (Villa Senni, 365.8 ± 1.2 ka) and TF-115 (Vico β_{top} , 406.4
848 ± 2.0 ka), the two tephra can be associated with the post-Rio Rava/pre-Brown Leucitic Tuff stage (355-440 ka;
849 Rouchon et al., 2008) of Roccamonfina volcano, and, more specifically, to the activity of the Monte Ofelio-
850 Monte Capitolo centers, dated to 398.5 ± 18.0 ka and 385.6 ± 16.0 ka (recalculated ages from Rouchon et al.,
851 2008). Although no glass composition is available for these Roccamonfina units, sample RMF6 of Monte
852 Capitolo (Rouchon et al., 2008; dated to 398.5 ± 18.0 ka), has a whole-rock phonolitic composition, which is
853 consistent with that of the two Fucino tephra (Fig. 12d). The attribution of the two tephra to Roccamonfina is
854 further supported by the analogous composition of two slightly older (i.e., MIS 12) Roccamonfina tephra layers
855 (S1-S2) from the Sessano basin, southern Italy, located immediately east of this volcano (Russo Ermolli et al.,
856 2010). Furthermore, the OH-DP-1640 tephra from Lake Ohrid (modelled age of 398.4 ± 6.0 ka; Leicher et al.,
857 2019), ascribed to Roccamonfina, could be tentatively correlated with TF-93/94 (Fig. 12d), based on a similar
858

859 age and geochemical composition (besides minor differences). Therefore, TF-93 and TF-94 can be attributed
860 to the Monte Ofelio-Monte Capitolo centers, and, based on good geochemical matching, more likely to the
861 latter. Future higher precision $^{40}\text{Ar}/^{39}\text{Ar}$ dating of these volcanic units in proximal setting will be of great interest
862 to strengthen the chronology and attribution proposed here.

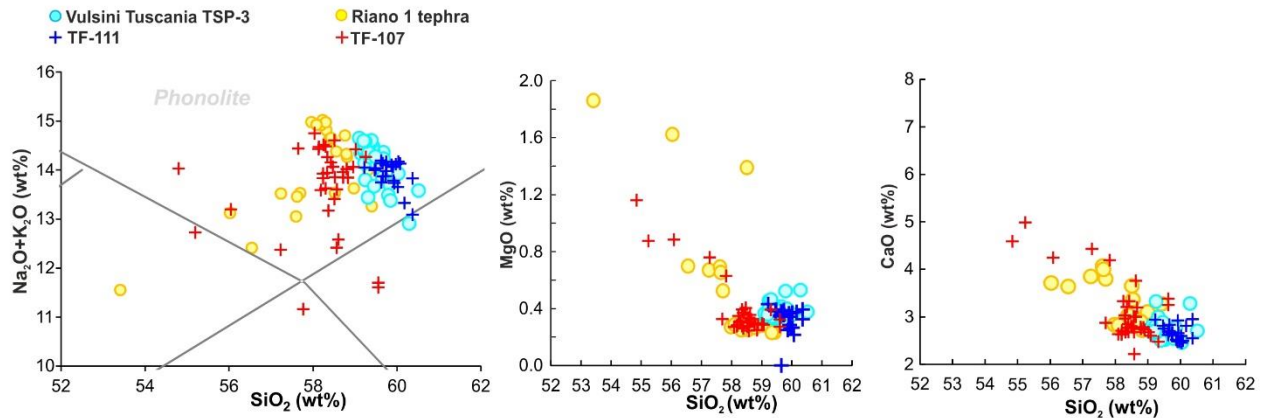
864 5.2.3.3. *Vulsini tephra*

865 **TF-107, TF-111 and TF-126** – In addition to TF-107 and TF-111, attributed to the Vulsini activity based on the
866 Cl vs CaO/FeO diagram (Fig. 7c) as discussed above, here we also re-evaluate the TF-126 layer, in light of
867 the acquired trace element data. Previously, TF-126 was tentatively correlated to the Castel Broco eruption of
868 Vulsini volcano, as well as geochemically matched to the pumice fall pre-Vico α , found immediately below Vico
869 α in the proximal area of Vico volcano (Pereira et al., 2020).

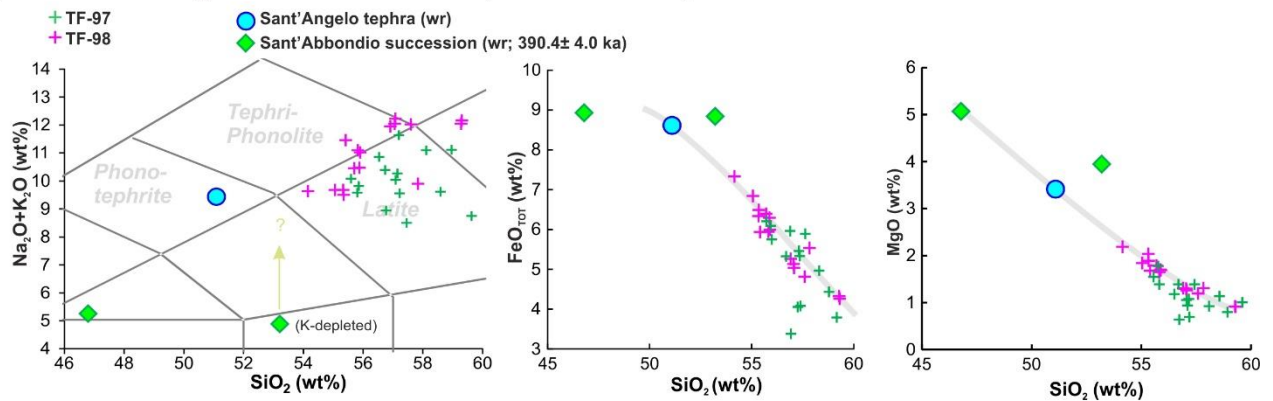
870 TF-107 and TF-111 are stratigraphically constrained between the ~365 ka TF-85/Villa Senni tephra and the
871 ~406 ka TF-115/Vico β_{top} . Within the Vulsini volcanic history (e.g., Palladino et al., 2010), the Pumice Fall 0
872 (PF-0) eruption (399.8 ± 18.0 ka; Turbeville, 1992), here tentatively identified with TSP-3 of the Tuscania-
873 San Pietro section, is the only known explosive event geochronologically consistent with both TF-107 and TF-
874 111. Of the two potential distal equivalents of PF-0/TSP-3, TF-111 shows a good geochemical match with
875 TSP-3 (Fig. 13a). Moreover, TSP-3 occurs below TSP-4 that has been here correlated to TF-109 (Fig. 12a),
876 which support the correlation of TF-111 with PF-0/TSP-3, even if $^{87}\text{Sr}/^{86}\text{Sr}$ ratios would seem do not suggest
877 it (Fig. 7).

878
879
880
881
882
883
884
885
886
887
888
889
890
891
892
893
894
895
896
897
898
899
900
901
902
903
904
905
906
907
908
909
910
911
912
913
914
915

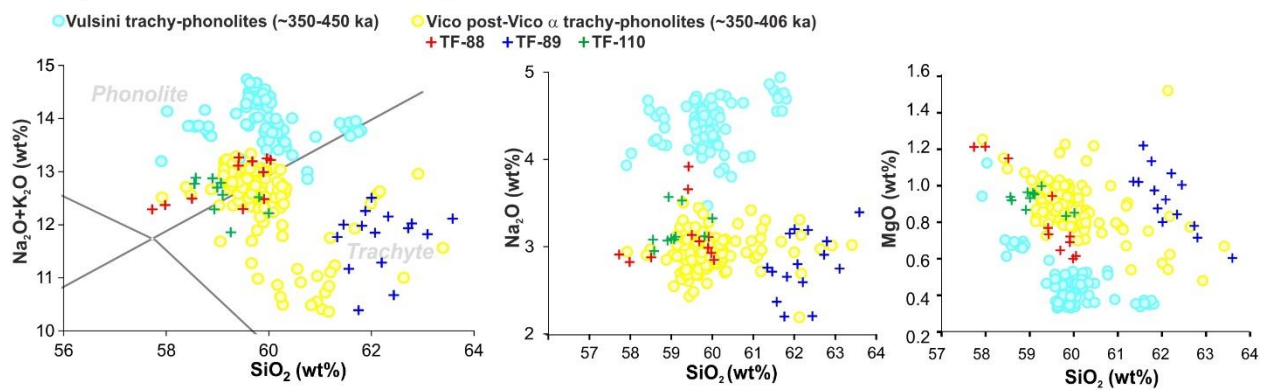
a) *Vulsini Pumice Fall 0(?) (~405-406 ka) - Riano 1 (404.7± 5.0 ka)*



b) *Vico Sant'Angelo-Sant'Abbondio (390.4± 4.0 ka)*



c) *Vico (~415-408 ka - ~366-390 ka)*



d) *Vulsini unknown (~406-405 ka - ~366-390 ka)*

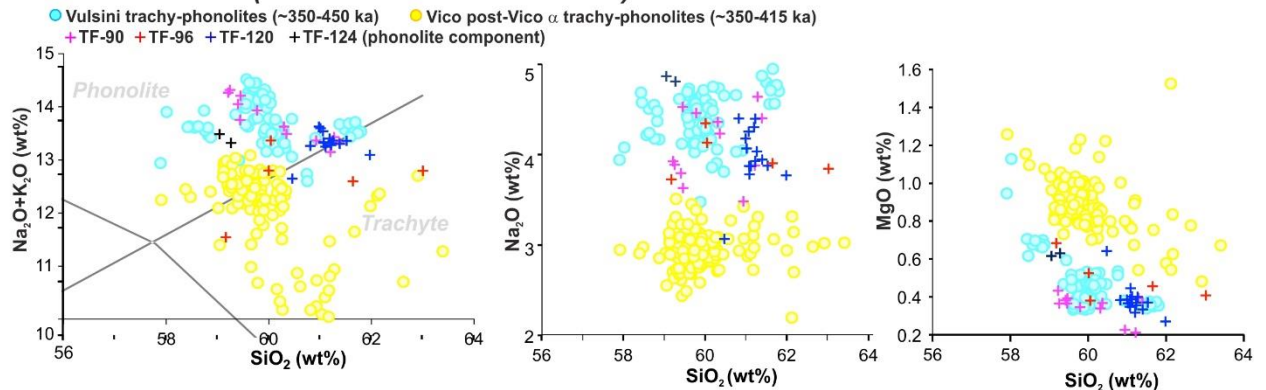


Figure 13. TAS diagram after Le Maitre et al. (2002) and representative bi-plots for the tephra TF-88, TF-89, TF-90, TF-107, TF110, TF-111, TF-120 and TF-124, compared with the proximal Vulsini unit TSP-3 from Tuscania-San Pietro section and Riano R-1 from the Riano succession (panel a), VCO 163 from Vico area, SA C4 and SA C5 from the Sant'Abbondio Fall succession (panel b) and with the proximal Vulsini (Casale delle Piane, Castel Broco, TSP-2 and TSP-3 from Tuscania-San Pietro section), and Post-Vico α Vico trachy-phonolites

(Vico β , Vico β_{top} , Vico γ) shown as blue and yellow circles in panels **c**) and **d**). Data source: WDS glass composition of tephra TF-88, TF-89, TF-90, TF-107, TF-110, TF-111, TF-120, Vulsini (TSP-2, TSP-3) and Riano R-1: this study; VCO 163 whole-rock geochemistry: [Perini et al. \(2004\)](#); SA C4 and SA C5 whole-rock geochemistry and $^{40}\text{Ar}/^{39}\text{Ar}$ age: [Marra et al. \(2014\)](#); $^{40}\text{Ar}/^{39}\text{Ar}$ age of R-1: [Marra et al. \(2018\)](#); WDS glass composition of Post-Vico α Vico trachy-phonolites (Vico β , Vico β_{top} , Vico γ): [Pereira et al. \(2020\)](#). $^{40}\text{Ar}/^{39}\text{Ar}$ ages are recalculated relative to an age of 1.1891 Ma for the Alder Creek sanidine monitor standard ([Niespolo et al., 2017](#)), with the uncertainties expressed at 2σ .

Regarding the trace element compositions, we notice that both TF-111 and TF-126 share similar levels of incompatible trace element enrichment to the trachytic components of the Vico α deposits, while they strongly differ from Castel Broco ([Fig. 11b](#)). This feature, on one hand, would preclude the correlation of TF-126 with Castel Broco and, on the other hand, would also raise doubts over the attribution of TF-111 and TF-126 layers to Vulsini, suggesting instead an origin from Vico. We note, however, that trace element data for Vulsini pyroclastic deposits are currently limited to only one sample from the co-eruptive basal fallout of Castel Broco ([Fig. 11b](#)), thus, they may not be fully representative of either the entire compositional spectrum of the Castel Broco eruption products, or even more so, the whole Vulsini eruptive successions. **Therefore, to take a conservative approach, while retaining a preferential attribution of TF-111 and TF-126 to the Vulsini district, we cannot fully exclude a Vico source for TF-111/TSP-3 and TF-126/pre-Vico α . Indeed, the unambiguous solution of this issue requires a statistically representative trace element dataset for both Vulsini and Vico products, which is not available yet.**

TF-107 shares a similar lithology and major element geochemistry with Riano R-1 tephra ([Fig. 13a](#)), here tentatively attributed to the activity of the Vulsini volcanic district ([Fig. 7c-II](#)) and dated at 404.7 ± 5.0 ka ([Marra et al., 2018](#)). While a correlation is further supported by very similar $^{87}\text{Sr}/^{86}\text{Sr}$ values ([Fig. 8; Table 5](#)), preliminary trace element glass analyses reveal some inconsistency ([Fig. 11b](#)).

5.2.3.4. Vulsini vs. Vico tephra

TF-88, TF-89, TF-90, TF-96, TF-97, TF-98, TF-110, TF-120, TF-124 – These nine tephra layers are characterized by Cl contents and CaO/FeO ratios consistent with both Vico and Vulsini volcanic sources ([Fig. 7c-III](#)).

TF-98 and TF-97 form, together with the rhyolitic tephra TF-99 (unambiguously from Vico; see section 5.2.2.), a stratigraphically strictly related cluster located between TF-85/Villa Senni and TF-116/Vico β . The age of this cluster is therefore bracketed between ~ 366 ka and ~ 406 ka. Among the potential Vico equivalents for TF-97 and TF-98, [Perini et al. \(2004\)](#) described the so-called Sant'Angelo tephra, which is stratigraphically constrained between Vico β (406.5 ± 2.4 ka; [Pereira et al., 2020](#)) and the Lava di Vico formation (~ 258 ka), thus chronologically consistent with TF-97 and TF-98, **as well as with TF-99, the latter unambiguously attributable to Vico due to its rhyolitic composition ([Fig. 12a](#)). However, no glass chemical composition is available for the Sant'Angelo tephra in literature, but only a single whole-rock composition in [Perini et al. \(2004\)](#). Even though whole-rock compositions allow only very limited comparison to glass-WDS data, a geochemical trend of TF-97/98 consistent with the whole-rock composition of the Sant'Angelo tephra ([Fig. 13b](#)) suggests a potential correlation. On the other hand, the whole rock composition of the Sant'Angelo tephra ([Perini et al., 2004](#)) is similar to that of the lowermost unit (i.e., SAAS C5) of the Sant'Abbondio lapilli and ash succession of [Marra et al. \(2014; Fig. 13b\)](#), which however yields a quite high loss on ignition, likely reflecting significant alkali loss. Nevertheless, less mobile elements make a tentative correlation of the Sant'Angelo tephra with SAAS C5 still tenable ([Fig. 13b](#)). The Sant'Abbondio succession, comprising at least**

931 six fallout horizons, occurs in the south-eastern sector of the Vico Volcano, at the boundary of the Vico-Sabatini
932 volcanic domains (Fig. 1b). The base and the top of this succession were $^{40}\text{Ar}/^{39}\text{Ar}$ dated at 390.4 ± 4.0 ka
933 (lowermost unit SAAS C5) and 380.4 ± 40.0 ka (uppermost unit SAAS C4; wide error associated with biotite
934 dating), and tentatively attributed to the Sabatini activity (Marra et al., 2014). However, considering its chemical
935 affinity with the Sant'Angelo tephra, the Sant'Abbondio lapilli and ash succession can be more likely ascribed
936 to the Vico activity and, possibly, to the Sant'Angelo unit. In summary, despite the lack of glass data for
937 Sant'Angelo/Sant'Abbondio and the weak geochemical correlation between TF-97/98 and the available whole-
938 rock composition, the Sant'Angelo-Sant'Abbondio succession appears as the only known chronologically
939 compatible and volcanologically plausible candidate for correlation. Therefore, as a preliminary tentative
940 attribution, we consider the tephra layers TF-97/98, and likely TF-99, as the distal expression of the
941 Sant'Angelo-Sant'Abbondio succession, which may represent the final explosive activity of the Vico Period I
942 (Perini et al., 2004).

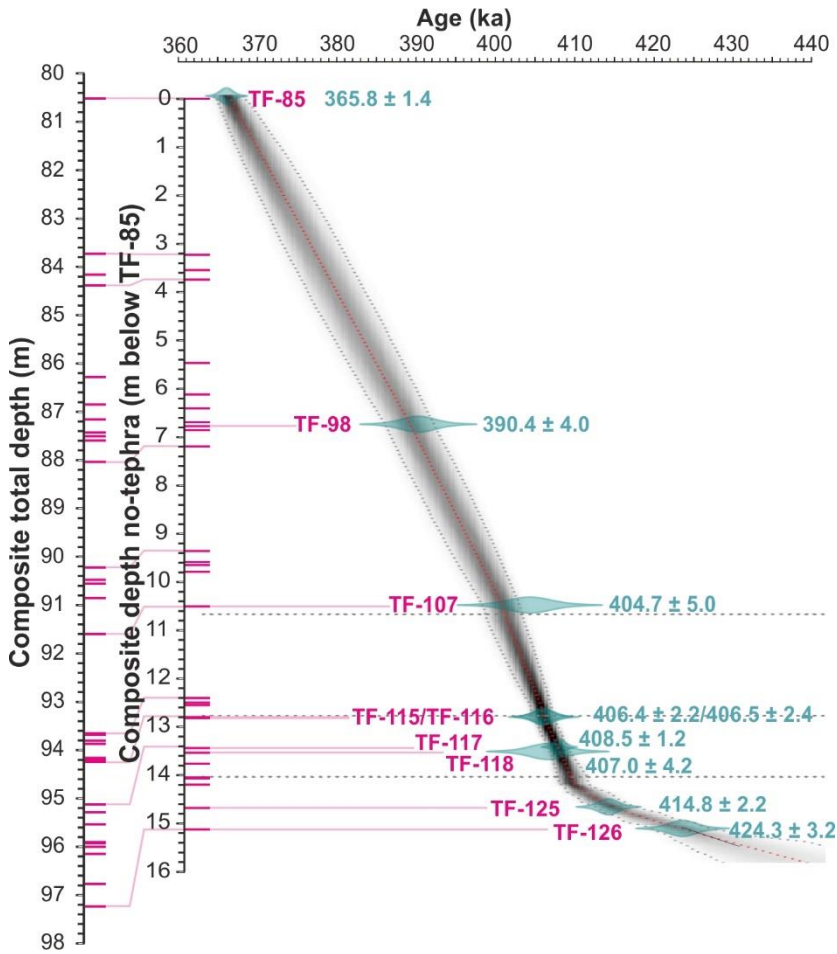
943 TF-88, TF-89, TF-90, TF-96, TF-110, TF-120 and TF-124, though apparently similar in composition and
944 indistinguishable in the Cl vs CaO/FeO diagram (Fig. 7c-III), can be easily attributed either to Vico or Vulsini
945 using the TAS and other simple bivariate diagrams, as shown in Figure 13c and 13d. Indeed, the glass
946 geochemistry of the post-Vico α trachy-phonolites (i.e., the trachy-phonolite component of Vico β , Vico β_{top} and
947 Vico δ) is quite different from that of the Vulsini trachy-phonolites spanning a similar time-interval (Fig. 13c-d).
948 Specifically, while TF-88, TF-89 and TF-110 systematically plot within the compositional fields of the post-Vico
949 α trachy-phonolites (Fig. 13c), TF-90, TF-96, TF-120 and the phonolite component of TF-124 plot in the field
950 of the Vulsini phonolites (Fig. 13d).

951 As for their potential proximal equivalents, TF-120 stratigraphically occurs between TF-117/Pozzolane Nere
952 (~ 408 ka) and TF-125/Vico α (~ 415 ka), i.e., geochronologically roughly consistent with PF-0 (399.8 ± 18.0 ka;
953 Turbeville, 1992), and thus might be considered as an alternative correlative for this Vulsini eruption, other
954 than the above-proposed TF-111. Finally, based on the available geochronological constraints, no specific
955 correlative deposits have been identified in the proximal records for the other Vico (TF-88, TF-89 and TF-110)
956 and Vulsini (TF-90, TF-96, TF-124) distal tephra layers.

957 5.3. Age model

959 Based on the direct and indirect (i.e., derived from geochemical fingerprinting) $^{40}\text{Ar}/^{39}\text{Ar}$ dating of the MIS 11
960 tephra record, we have developed a Bayesian depth-age model. Only a sub-set of radioisotopic ages (from
961 direct dating or reliable geochemical and/or stratigraphical correlations) with the necessary requisites of both
962 accuracy and precision were selected for this purpose. Specifically, for the investigated interval we selected
963 nine ages from an equivalent number of tephra layers, as shown in Figure 14. The depth-age curve (Fig. 14)
964 shows a remarkable slope change at ~ 410 ka, indicating that the sedimentation rate was distinctly lower in the
965 first part of the MIS 11 period (~ 424 - 410 ka). This change in sedimentation rate coincides with a shift in Ca,
966 from a relatively long and more stable period with of high Ca to a period characterized by large and rapid,
967 millennial-scale variations of Ca (Fig. 15). Ca was ascribed to represent lake primary productivity (Giaccio et
968 al. 2019, Mannella et al 2019) and thus the marked change in sedimentation rate is likely related to changing
969 environmental conditions, a topic which will be addressed elsewhere. Here, we can only underscore that this
970 change cannot be interpreted as a distortion of the age-depth curve due to the age model uncertainty, because

971 it occurs in a stratigraphic interval that is firmly well constrained by several radioisotopic dating dates (Fig.
 972 15).



973 **Figure 14.** Bayesian age-depth model for the investigated F4-F5 tephra record of the MIS 11 interval.

1
2
3
4
5
6
7
8
9
10
11
12
13
14
15
16
17
18
19
20
21
22
23
24
25
26
27
28
29
30
31
32
33
34
35
36
37
38
39
40
41
42
43
44
45
46
47
48
49
50
51
52
53
54
55
56
57
58
59
60
61
62
63
64
65

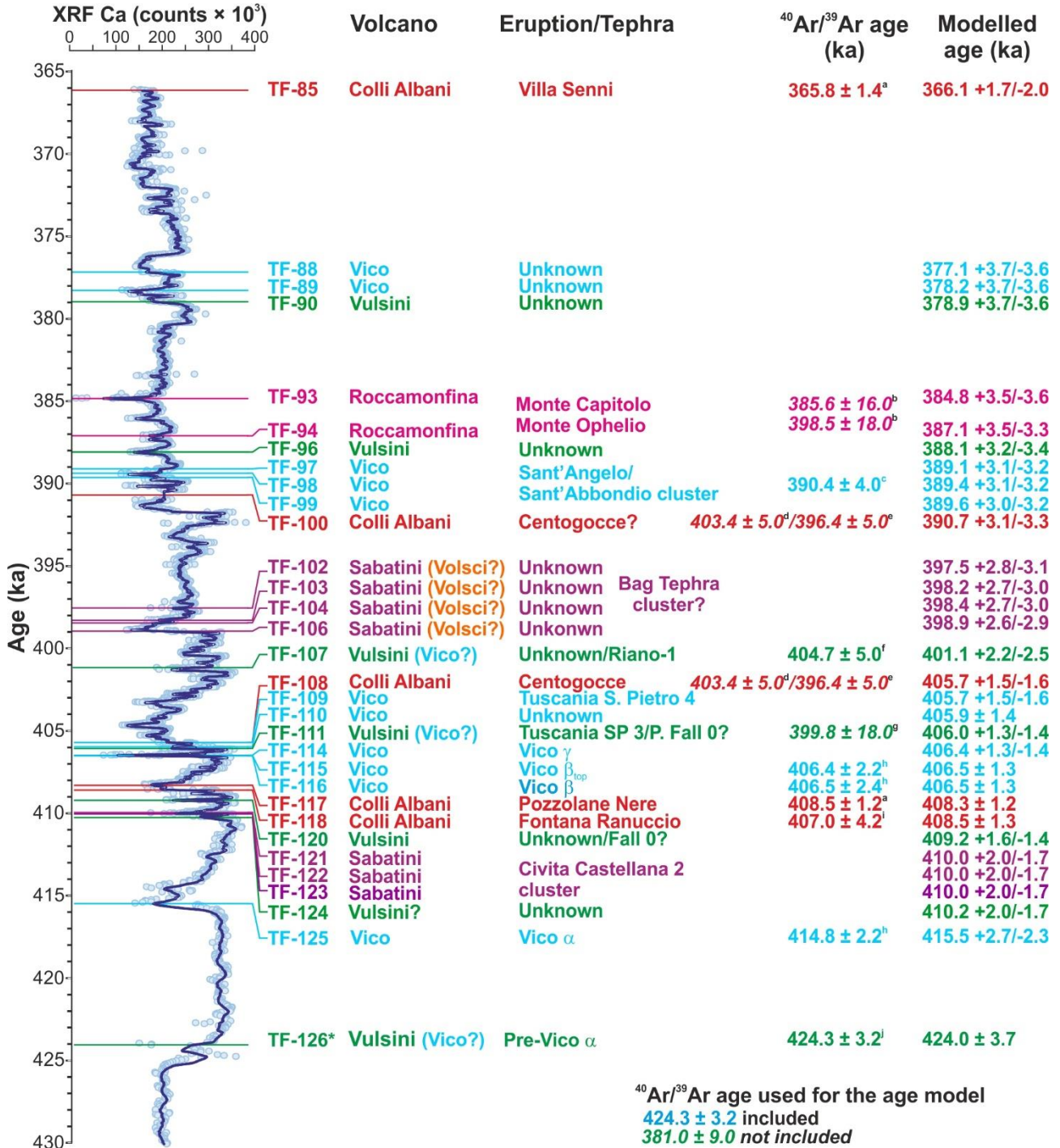


Figure 15. Summary of the volcanic sources, individual correlation and chronology (⁴⁰Ar/³⁹Ar and modelled ages) of the investigated Fucino F4-F5 tephra record. The MIS 11 temporal series of the calcium content in Fucino lacustrine sediments from F4-F5 core is also shown (XRF data from Giaccio et al., 2019). Ages not used for the age model are reported in italics. Data source: ^a this study; ^b Rouchon et al. (2008); ^c Perini et al. (2004); ^d Marra et al. (2014); ^e Marra et al. (2009); ^f Turbeville (1992); ^g Pereira et al. (2020); ^h Pereira et al. (2018); ⁱ Giaccio et al. (2019).

The age-depth model allows us to reliably assess the age and climatostratigraphic position of each individual tephra in the F4-F5 MIS 11 section, as shown in Figure 15. Such an integrated paleoenvironmental-tephra record provides a stratigraphically ordered series of tephra within the framework of the sub-millennial scale paleoclimatic variability of the MIS 11 period, which represents one of the most important features of this kind of integrated record. Indeed, while the chronology is susceptible of improvements through time, the

989 climatostratigraphic position of each tephra is firmly and definitively established here. For instance, the TF-126
990 tephra is a valuable marker for the onset of a higher productivity interval, likely driven by higher temperature
991 and enhanced nutrients delivery, i.e.; typical of interglacial conditions (i.e., MIS 11c; Fig. 15). This specific
992 climatostratigraphic position is independent of the current geochronological (and source) uncertainties of TF-
993 126 tephra and of any possible future improvement in accuracy and precision of the TF-126 dating itself.

994 995 **5.4. The Fucino MIS 11 tephra record in the framework of central Mediterranean Middle Pleistocene** 996 **tephrochronology and its relevance for the Quaternary sciences and volcanology**

997 In the framework of the Mediterranean tephrostratigraphy, only few relatively continuous records span through
998 the Middle Pleistocene (Fig. 1a). The on-land marine succession of Montalbano Jonico, southern Italy (Figs.
999 1a, 16), records the southern-Italy peri-Tyrrhenian and Vulture volcanic activity at the Early-Middle Pleistocene
1000 transition and provides the first evidence for an early onset of the volcanic activity in the Campania area, at
1001 the beginning of the Middle Pleistocene (Petrosino et al., 2015). The radioisotopic geochronological data
1002 acquired from Montalbano Jonico also allowed a better constraint of the chronology of the MIS 19 paleoclimatic
1003 change (Nomade et al., 2019) and of the cosmogenic nuclide ^{10}Be increase during the Matuyama-Brunhes
1004 geomagnetic reversal (Simon et al., 2018).

1005 The Sulmona Basin lacustrine succession, in central Italy (Figs. 1a, 16), represents another rich tephra archive
1006 encompassing the Early-Middle Pleistocene transition, which records an intense and frequent activity of the
1007 peri-Tyrrhenian volcanism (Giaccio et al., 2013b), poorly documented (or so far unrecognized) in proximal
1008 settings (Marra et al., 2014; Sottili et al., 2019). The Sulmona succession also provided the basis for
1009 assembling a robust radiometric chronology for both local and extra-regional MIS 19 paleoclimatic records
1010 (Giaccio et al., 2015a; Regattieri et al., 2019) and for constraining the timing of the Matuyama-Brunhes
1011 geomagnetic reversal (e.g., Sagnotti et al., 2014). Also, the Sulmona Basin tephra record spans
1012 discontinuously the MIS 15-MIS 10 period (e.g., Giaccio et al., 2013b, Giaccio et al., 2014; Regattieri et al.,
1013 2016), but a comprehensive tephra study for this interval is still pending. Specifically, among a number of
1014 tephra spanning the MIS 11 period (Fig. 16), currently only one tephra has been geochemically characterized
1015 (Regattieri et al., 2016). Based on its trachyte-rhyolite composition Regattieri et al. (2016) correlated it to Vico
1016 α , but according to the upgraded geochemical dataset obtained by Pereira et al. (2020) for the Vico Period I
1017 units, this tephra could be either attributed to Vico α or Vico β (Pereira et al., 2020).

1018 The rich tephra record of the river-lagoon stacked aggradational successions of the Tiber River delta, in central
1019 Italy (Figs. 1a, 16), though discontinuous, allowed to radioisotopically constrain the timing of the sea-level rise
1020 during the last eleven deglaciations (e.g., Marra et al., 2016b; Luberti et al., 2017), including the MIS 11 period
1021 (Fig. 16). However, only few tephra have been so far geochemically fully characterized (e.g., Pereira et al.
1022 2020), thus limiting the great potential of this succession for tephrochronological purposes.

1023 The deep-sea core KC01B in the Ionian Sea (Fig. 1a) spans continuously the last 1.1 Ma (Lourens, 2004), but
1024 detailed tephrostratigraphic investigations are currently available only for the last 200 kyr (Insinga et al., 2014;
1025 Fig. 16). A recent detailed tephra and crypto-tephra study of the nearby core ODP Site 964 (Fig. 1) allowed to
1026 extend this tephrochronological record back to 625 ka (Fig. 16) and to get for the first time a reliable
1027 synchronization of the marine and terrestrial records during specific intervals of the MIS 13 and MIS 10
1028 (Vakhrameeva et al., 2021).

1029 The Mercure, Vallo di Diano and Acerno basins in southern Italy (Figs. 1a, 16), in addition to some known
1030 major eruptions from Latium volcanoes, revealed a conspicuous activity of the Roccamonfina volcano during
1031 the MIS 15-MIS 12 period that is still fragmentary known or not currently found in the near-source volcanic
1032 area (Karner et al., 1999; Giaccio et al., 2014; Petrosino et al., 2014a; 2014b). Also located in southern Italy,
1033 the San Gregorio Magno lacustrine succession (Fig. 1a) provides a valuable tephra record of the poorly known
1034 late Middle Pleistocene activity of the Campanian Volcanic Zone, although not extending beyond 250 ka
1035 (Petrosino et al., 2019; Fig. 16). Similarly, the Adriatic Sea core PRAD 1-2 (Fig. 1a), partially extends a short
1036 interval into the late Middle Pleistocene by reaching ~200 ka (Bourne et al., 2015; Fig. 16).

1037 In the Eastern Mediterranean area, the marine Aegean Sea cores KL49, KL51 and LC21, and the terrestrial
1038 (peatland) tephra record of the Tenaghi Philippon basin (Vakhrameeva et al., 2019), in Greece (Fig. 1a), were
1039 used in combination for reconstructing and indirectly dating the explosive activity of the Santorini volcano in
1040 the last 360 kyr (Wulf et al., 2020, Fig. 16). The Tenaghi Philippon archive also documents a MIS 12-MIS 10
1041 tephra record, which was dated climatostratigraphically by using the high-resolution pollen profile, allowing a
1042 first age estimation of the tephra series of either known or unknown origin (Vakhrameeva et al., 2018; Fig. 16).

1043 Finally, the long and continuous tephra record from Lake Ohrid (Albania-North Macedonia, Fig. 1a), mostly
1044 from peri-Tyrrhenian potassic volcanic sources, provided important geochronological constraints for
1045 developing a robust age model for the outstanding 1.36 Ma-long palaeoclimatic succession, but also for so-far
1046 unknown volcanic eruptions (Leicher et al., 2019; Wagner et al., 2019; Fig. 16).

1047 In summary, from the above-mentioned Mediterranean Middle Pleistocene tephra records only four long and
1048 relatively continuous successions document in detail the MIS 11 period, i.e., the Sulmona Basin in central Italy,
1049 Lake Ohrid in Albania-Macedonia, the Tenaghi Philippon peatland in Greece and the Ionian Sea core ODP
1050 Site 964 (Figs. 1a, 16). However, beside the uncompletely explored Sulmona record, due to their remote
1051 location with respect to the peri-Tyrrhenian volcanoes, the remaining three MIS 11 records document none or
1052 only the largest explosive eruptions of the peri-Tyrrhenian potassic volcanic systems, which are the only
1053 sources of the tephra found in Fucino lake record. Specifically, among the Fucino MIS 11 tephra succession,
1054 only two tephra layers are found at Lake Ohrid, i.e., (i) Vico α /TF-125/OH-DP 1700.6 and (ii) Roccamonfina
1055 Monte Ofelio-Monte Capitolo/TF-96/OH-DP 1640 (Fig. 16), while a third layer, not identified at Fucino, was
1056 correlated to an undefined Roccamonfina eruption occurred at onset of the MIS 11 period (Leicher et al., 2019).

1057 Due to their even more remote locations with respect to the peri-Tyrrhenian potassic volcanic sources, the MIS
1058 11 records of Tenaghi Philippon and ODP-964 document only few potentially-unknown tephra from Neapolitan
1059 volcanoes, the majority being related to the volcanic sources of Santorini, for Tenaghi Philippon, and Santorini,
1060 Aeolian Islands and South Aegean Volcanic Arc, for ODP-964 (Vakhrameeva et al., 2018, 2019, 2021).

1061 Actually, none of these MIS 11 tephra from Tenaghi Philippon or ODP-964 are found in the Fucino record.

1062 In conclusion, the general tephrostratigraphy framework and lattice of correlation for the MIS 11 period is far
1063 for being satisfactory developed for a reliable application to Quaternary sciences and volcanology. In this
1064 regards, the Fucino MIS 11 record arises as a one of the fundamental reference geochemical and
1065 chronological dataset for the future development and application of the tephrochronology in the Mediterranean
1066 region, especially for the areas closer to the highly productive tephra sources of peri-Tyrrhenian potassic
1067 volcanoes. i.e., that have the potential of capturing part of the activity recorded at Fucino and thus to benefit
1068 of its rich tephrochronological record.

1070 **5.5. Implications for the peri-Tyrrhenian explosive volcanic history**

1071 *5.5.1. Distal tephrostratigraphy for elucidating explosive eruption histories: Advantages and limitations*

1072 Assessing the issue of the explosive volcanism history using distal archives presents a series of advantages,
1073 but also limitations that need to be discussed. Indeed, though on one hand the general overview provided in
1074 previous section show that distal archives often document explosive activity that is hardly traceable to known
1075 eruptions or activity of given volcanic source, thus highlighting the great potential of the distal
1076 tephrostratigraphy for the assessment of the explosive activity on a regional scale, on the other, a number of
1077 geographical, physical and time-dependent factors can limit the approach of the distal tephrostratigraphy.

1078 Specifically, the completeness of a distal archive with respect to a given volcano or cluster of volcanoes
1079 depends on the (i) distance from the volcanic sources, (ii) position with respect to the dominant winds, (iii)
1080 magnitude and intensity of the events, (iv) direction of the dispersal axis with respect to the volcano and distal
1081 archive location, (v) eruptive dynamics, (vi) variability of the atmospheric circulation pattern during glacial-
1082 interglacial and sub-orbital scale climate change. In turn, the impact of all these factors in limiting the
1083 usefulness of the distal tephrostratigraphy depends on the number and the geographical distributions of the
1084 distal archives documenting the same temporal interval and, more critical, the activity of the same volcanic
1085 system. In fact, a dense network of distal archives distributed across a wide region surrounding a given
1086 volcano, sensibly enhances the possibility of capturing the whole activity of a given volcanic system, reducing
1087 all the above-mentioned uncertainty and limitation factors and allowing to construct a composite record.

1088 As stressed throughout the paper, at present only limited tephrostratigraphic records span the interval
1089 documented in this study in great detail, and only one (i.e., Lake Ohrid) record shares with Fucino some tephra
1090 from the peri-Tyrrhenian potassic volcanic sources (Fig. 16). Therefore, the framework of the explosive activity
1091 of these volcanic systems obtained using the distal records is likely to be far from complete because of the
1092 poorly developed network of tephra record and lattice of correlations. Nevertheless, due to its privileged
1093 location, we are able to demonstrate that the Fucino paleolake captured most of the known major eruptions
1094 and many other unknown explosive events of the peri-Tyrrhenian potassic volcanoes. Therefore,
1095 reconstructing the explosive history of the peri-Tyrrhenian potassic volcanoes during the MIS 11 period using
1096 the Fucino record alone is fully justified and supported by the data gathered which illustrates that Fucino
1097 provides an extremely detailed eruption record.

42
43
44
45
46
47
48
49
50
51
52
53
54
55
56
57
58
59
60
61
62
63
64
65

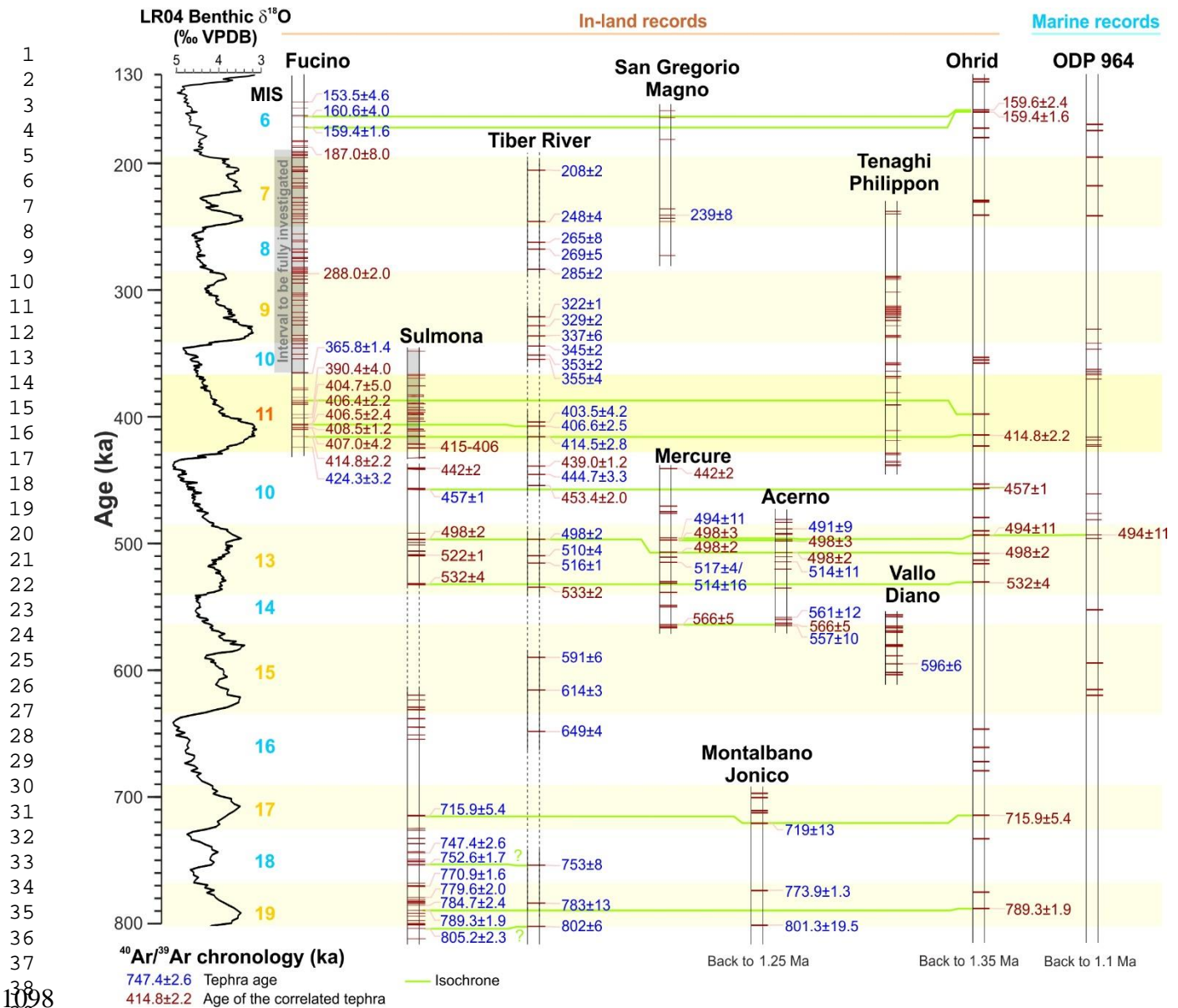


Figure 16. The Fucino MIS 11 tephra record within the framework of the Mediterranean Middle Pleistocene tephrochronological records. Data source: **Fucino**: Giaccio et al. (2017, 2019), Mannella et al. (2019), This study; **Sulmona**: Giaccio et al. (2013a, 2013b, 2014, 2015a), Sagnotti et al. (2014), Regattieri et al. (2015, 2019); **Tiber River**: Florindo et al. (2007), Villa et al. (2016), Marra et al. (2016a, 2017, 2019, and references therein), Pereira et al. (2020); **Mercure**: Giaccio et al. (2014), Petrosino et al. (2014a); **San Gregorio Magno**: Munno and Petrosino (2007), Petrosino et al. (2019); **Montalbano Jonico**: Petrosino et al. (2015); **Acerno**: Petrosino et al. (2014b); **Vallo di Diano**: Karner et al. (1999); **Tenaghi Philippon**: Vakhrameeva et al. (2018, 2019), Wulf et al. (2020); **Lake Ohrid**: Leicher et al. (2016, 2019), Wagner et al. (2019); **ODP 964**: Vakhrameeva et al. (2021).

5.5.2. The proximal record

In order to compare the distal (Fucino) and the proximal records of the peri-Tyrrhenian explosive volcanism of central Italy, we critically review the available geochronological data. The general framework of literature data for the peri-Tyrrhenian volcanic activity encompassing the MIS 11 period, or a slightly wider a temporal interval, is provided in Table 7. Though partially and fragmentarily mentioned in previous sections, i.e., when discussing the individual correlation, in the following we provide a general overview summarizing the state of art of the knowledge on the history of the peri-Tyrrhenian potassic explosive volcanism.

For the Vulsini Volcanic District, only one direct radioisotopic age determination is available for the study interval, i.e., the already mentioned Pumice Fall 0 dated at 399.8 ± 18.0 ka (Turbeville, 1992; Table 7). Castel

1117 Broco and Casale delle Piane are two other prominent Vulsini eruption units potentially falling in the
 1118 investigated interval, although lacking direct dating. Recently, Marra et al. (2020a) provided a tentative
 1119 reconstruction of the eruptive history in this time span, based on xenocryst populations occurring in primary
 1120 and reworked deposits of the eastern Vulsini (Bolsena-Orvieto and Vulsini Fields activities; Table 7),
 1121 suggesting that the statistically most significant population age of 425.4 ± 1.6 ka may correspond to that of the
 1122 Castel Broco eruption.

Table 7. Summary of the literature geochronological data for the peri-Tyrrhenian potassic volcanism of central Italy during the MIS 11, or a slightly wider interval. When possible, i.e., if all the all the required analytical data were published, $^{40}\text{Ar}/^{39}\text{Ar}$ ages are recalculated relative to an age of 1.1891 Ma for the Alder Creek sanidine or relative to an age of 28.294 Ma for the Fish Canyon sanidine monitor standards (Niespolo et al., 2017), with the uncertainty expressed at 2σ .

Volcanic source	Volcanic phase	Unit/sample	Type of activity/product	K/Ar and $^{40}\text{Ar}/^{39}\text{Ar}$ age (ka $\pm 2\sigma$)	References	
Vulsini	Bolsena	Ponticello Pumices	Pumice fall	352.0 \pm 4.0	Nappi et al., 1995	
		Fall 0	Pumice fall	345.4 \pm 2.1	Marra et al., 2020a	
	Vulsini Field	Castel Broco	Pumice fall-pyroclasti flow	n.d.		
		Piano della Selva	Pyroclastic flow	n.d.		
		Indirect evidence from xenocrysts age populations	undefined		400.5 \pm 3.7	Marra et al., 2020a
					411.4 \pm 2.4	
Vico	Period I	SAAS-bottom	Pumice fall	390.4 \pm 4.0	Marra et al., 2014	
		VICO δ	Pumice fall	399.7 \pm 3.0		
		VICO γ	Pumice fall	n.d.		
		VICO β_{top}	Pumice fall	406.4 \pm 2.0	Pereira et al., 2020	
		VICO β	Pumice fall	406.5 \pm 2.4		
		VICO α	Pumice fall	414.8 \pm 2.2		
Sabatini	Southern Sabatini	CC-2	Pumice fall	n.d.	Pereira et al., 2020	
		La Rosta	Pumice fall	439.1 \pm 1.0	Marra et al., 2020b	
		FALL F	Pumice fall	448.5 \pm 7.0	Marra et al., 2014	
Colli Albani	Villa Senni Eruption Cycle	Madonna degli Angeli succession	Lava dyke	354.5 \pm 6.0	Gaeta et al., 2006 and references therein Marra et al 2003	
			Lava flow	357.5 \pm 9.0		
			Lava flow	359.5 \pm 6.0		
			Lava flow	359.5 \pm 8.0		
	Pozzolane Nere Eruption Cycle	Pantano Secco hydromagmatic center	Madonna degli Angeli succession	Scoria fall	368.6 \pm 2.0	
				Lava flow	369.6 \pm 3.0	
		Tufo Lionato	Corcolle succession	Pyroclastic flow	368.6 \pm 4.0	
				Lava flow	396.0 \pm 5.0	
		Pozzolane Rosse Eruption Cycle	Pozzolane Nere	Vallerano Lava	Scoria fall	402.3 \pm 5.0
					Pyroclastic flow	407 \pm 2.0
Volsci volcanic filed		Selva Piana	Lava	362.0 \pm 11.0	Boari et al., 2009	
		Colle Avarone CA-CGT	Reworked volcanic horizon	360.8 \pm 6.5	Marra et al., 2021	
		Isoletta III	Scoria fall	363.8 \pm 8.0	Pereira et al., 2018	
		Isoletta II	Scoria fall	373.7 \pm 4.0		
		Valcatara	Lava dyke	379.0 \pm 8.0	Boari et al., 2009	
		Lademagne II	Reworked volcanic horizon	387.7 \pm 5.0	Pereira et al., 2018	
		Pofi-Colle La Grotta	Phreatomagmatic deposit	391.5 \pm 3.6	Marra et al., 2021	
		Giuliano di Roma	Lava	394.6 \pm 6.0	Boari et al., 2009	

1
2
3
4
5
6
7
8
9
10
11
12
13
14
15
16
17
18
19
20
21
22
23
24
25
26
27
28
29
30
31
32
33
34
35
36
37
38
39
40
41
42
43
44
45
46
47
48
49
50
51
52
53
54
55
56
57
58
59
60
61
62
63
64
65

		Pofi Scoria cone	Scoria fall	394.4±3.5	Marra et al., 2021
		Cava Pompei	Scoria fall	392.7±3.0	Pereira et al., 2018
		Arnara Scoria cone	Scoria fall	395.8±6.1	Marra et al., 2021
		Isoletta I	Scoria fall	401.7±3.0	Pereira et al., 2018
		Lademagne I	Scoria fall	404.0±5.0	
		Supino	Phreatomagmatic deposit	407.7±2.6	Marra et al., 2021
		La Tomacella, upper	Pyroclastic rock	410.0±10.0	Boari et al., 2009
		Tecchiena	Lava	416.1±11.0	Boari et al., 2009
		Cellesta	Lava	417.1±6.0	
		La Tomacella, lower	Pyroclastic rock	425.2±13.0	
				343.6±6.0	Scaillet et al., 2008
		Brown Leucititic Tuff	Pyroclastic flow	358.2±10.0	Rouchon et al., 2008
				385.0±23.0	Luhr and Giannetti, 1987
		Scipicciano 89X	Lava flow	361.7±10.0	Rouchon et al., 2008
		Fontana-radina RMF7	Lava flow	363.7±16.0	
				360.0±42.0 (GM)	Giannetti, 2001
		SP/R-30	Lava dome	382.0±3.0 (San)	
				390.0±30.0 (San)	
		SP/R-31	Effusive	370.8±3.0	Rouchon et al., 2008
		La Frascara RMF4	Lava flow	373.9±18.0	
		Galluccio RMF3	Lava flow	375.9±16.0	Radicati di Brozolo et al., 1988
		Monte Casi	Lava dome	370.0±9.0	
				378.9±4.0 (San)	Giannetti, 2001
		LP/R-247	Effusive	399.3±12.0 (San)	
				430.0±6.0 (GM)	
		MLT/R-352	Lava flow	374.0±11.0	Rouchon et al., 2008
		MLP/R-69	Lava dome	376.0±16.0	
		Monte Capitolo RMF6	Pyroclastic	396.2±16.0	Rouchon et al., 2008
		Masseria Robetti	Lava flow	397.0±18.0	Radicati di Brozolo et al., 1988
		MLT/R-290	Lava flow	408.4±9.0	Giannetti, 2001
		Monte Ofelio RMF12	Pyroclastic	409.4±18.0	Rouchon et al., 2008
				409.4±10.0	Giannetti, 2001
		MLT/R-351	Lava flow	415.5±18.0	
		LP/R-104	Lava dome	416.6±32.0	Radicati di Brozolo et al., 1988
		Masseria Robetti	Undefined	421.0±9.0	
		LP/T-247	Lava dome	430.0±6.0	Giannetti, 2001
		Rio Rava RMF14	Lava flow	446.0±12.0	Rouchon et al., 2008

GM, groundmass; San, sanidine.

At Vico Volcano, multiple explosive eruptions of sub-Plinian to Plinian intensity occurred in the investigated interval, which roughly matches the Vico Period I stage (Perini et al., 2004), including: Vico α , Vico β , Vico β_{top} , Vico γ , Vico δ and Sant'Angelo tephra (Cioni et al., 1987; Perini et al., 2004; Pereira et al., 2020) (Table 7). The chronology of the Vico Period I has recently been improved by Pereira et al. (2020) who reported new $^{40}\text{Ar}/^{39}\text{Ar}$ ages for 4 out of the 5 of the main eruption units recognised in proximal settings (Table 7). In addition, we may put an age constraint to the Sant'Angelo tephra (Perini et al., 2004), based on the proposed correlation to the Sant'Abbondio lapilli and ash succession (390.4 ± 4.0 ka; Marra et al., 2014).

In contrast, no relevant activity is documented at Sabatini Volcanic District during the MIS 11 period. Indeed, the intense explosive activity of the Southern Sabatini stage took place between 500 ka ("Fall A" Plinian

1139 eruption) and 439 ka (“La Rosta” Plinian fall; Sottili et al., 2004; Marra et al., 2020b, while the subsequent
1140 Bracciano stage starts at ~325 ka, thus indicating a long phase of quiescence extending more than ~100 kyr
1141 at the volcano. However, the recent attribution of CC-2 fall, which is bracketed between Vico α and Vico β , to
1142 the Sabatini activity (Pereira et al., 2020), would partially fill this seemingly long gap of activity. Moreover, as
1143 already mentioned in section 3.1., the Strombolian lithological features of the R-2 tephra occurring in the MIS
1144 11 lacustrine succession cropping out near Riano (Fig. 1), laying below the Vulsini tephra Riano R-1 dated at
1145 404.7 ± 5.0 ka (Marra et al., 2018; Table 7), would also suggest the occurrence of a minor explosive activity
1146 of Mts Sabatini during the MIS 11 period.

1147 The 450-350 ka interval at the Colli Albani Volcanic District was characterized by the occurrence of three main
1148 eruption cycles, all belonging to the Tuscolano-Artemisio phase of activity: Pozzolane Rosse, Pozzolane Nere
1149 and Villa Senni Eruption Cycles (Freda et al., 1997, 2011; Giordano et al., 2006; Marra et al., 2009; Gaeta et
1150 al., 2016) (Table 7). Each cycle is characterized by large, caldera-forming eruptions, emplacing up to several
1151 tens of km³ of pyroclastic-flow deposits (De Rita et al., 1988, 1995). The climatic phases were followed by
1152 several kyr-long post-caldera phases of activity, characterized by Strombolian and effusive eruptions revealed
1153 by numerous scoria cones and lava vents along peri-caldera ring faults, namely the Corcolle, Centogocce and
1154 Madonna degli Angeli successions (Giordano et al., 2006) (Table 7). The three eruption cycles were separated
1155 from each other by ~50 kyr-long quiescent intervals (Marra et al., 2009; Gaeta et al., 2016).

1156 The Volsci Volcanic Field was characterized by diffuse, low-scale, magmatic (Strombolian and subordinate
1157 effusive) and phreatomagmatic activities from monogenetic scoria cones and tuff rings (e.g., Cardello et al.,
1158 2020; Marra et al., 2021). Several radioisotopic age determinations, encompassing the investigated interval,
1159 have been recently acquired (Boari et al., 2009; Nomade et al., 2011; Pereira et al., 2018; Marra et al., 2021)
1160 (Table 7). It appears that available ⁴⁰Ar/³⁹Ar ages are often grouped in statistically indistinguishable clusters
1161 (Table 7), which could be referred to either an individual eruptive event or multiple, closely spaced, eruptions.
1162 In reconstructing eruptive activity, this could lead to overestimate (i.e., multiple dating of the same eruption) or
1163 underestimate (i.e., grouping of statistically indistinguishable datings that actually refer to multiple events) the
1164 number, frequency and recurrence of the events. Notwithstanding, the quite distinctive compositional features
1165 of the Volsci products (Marra et al., 2021 and references therein), the usual lack of analyzable glass in the
1166 dated pyroclastic samples prevents their reliable application for tephrochronological purposes. Therefore, the
1167 current data available for the Volsci volcanic field prevent us from assessing the presence of tephra layers
1168 from this volcanic system in distal settings (including Fucino) and thus potentially improving its explosive
1169 history.

1170 Finally, for the Roccamonfina volcano, despite the large number of dated products, many of the samples
1171 ranging in age from 446 ± 4 ka to 353 ± 5 ka pertain to effusive or poorly defined products (Luhr and Giannetti,
1172 1987; Radicati di Brozolo et al., 1988; Giannetti, 2001; Rouchon et al., 2008) (Table 7). Only the major Brown
1173 Leucitic Tuff eruption, and the minor Mt. Capitolo and Mt. Ofelio eruptions document explosive activity in the
1174 investigated timespan (Table 7). Moreover, several of these samples were dated by K/Ar method and yielded
1175 low precision, and therefore are scarcely reliable ages (Table 7). For example, a previous dating on the Brown
1176 Leucitic Tuff provided a quite imprecise age of 385 ± 23 ka (Luhr and Giannetti, 1987), and also differs quite
1177 significantly from more recent age determinations obtained for this eruption (e.g., 358.2 ± 10.0 ka, Rouchon et
1178 al., 2008; 343.6 ± 6.0 , Scaillet et al., 2008). Finally, a large uncertainty, and unreliability, is reflected by the

1179 scattered ages obtained by dating different material from the same sample (e.g., SP/R-30 and LP/R-247; Table
1180 7).

1181 1182 **5.5.3. Comparing the proximal and Fucino records of the peri-Tyrrhenian potassic volcanism**

1183 The above critical revision of the available literature data for the peri-Tyrrhenian explosive volcanism of central
1184 Italy allows a suitable comparison with Fucino MIS 11 tephra record. Overall, the history of the peri-Tyrrhenian
1185 explosive volcanism recorded at Fucino appears substantially richer and temporally better resolved with
1186 respect to the proximal settings (Fig. 17b). Noteworthy, the Fucino record provides direct evidence for “ghost”
1187 eruptive events that may lack exposures (or are not yet been identified) within the proximal successions.
1188 Indeed, the age distribution of xenocrysts extracted from Vulsini pyroclastic units younger than MIS 11 (Marra
1189 et al., 2020a) define three clusters at 425.4 ± 1.6 ka, 411.4 ± 2.4 ka and 400.5 ± 3.7 ka (Table 7; Fig. 17b) that
1190 so far do not correspond with dated exposed products, or undated potential candidates, which are in good
1191 agreement with the $^{40}\text{Ar}/^{39}\text{Ar}$ and modelled ages of the Fucino tephra TF-126 (424.0 ± 3.7 ka) and TF-120
1192 (409.2 ± 1.6 ka) and of TF-107 (401.1 ± 2.5 ka), correlated to Vulsini (Figs. 15 and 17b), providing evidence
1193 for such a ghost volcanic activity.

1194 The Fucino record further refines our knowledge of the early explosive history of Vico Volcano (Pereira et al.,
1195 2020). Indeed, with the exception of the missing Vico δ , Fucino documents the whole known activity of Vico
1196 Period I and highlights new eruptive events still unrecognised in proximal areas (i.e., TF-99 and TF-109). The
1197 age-depth model of Fucino indicates that the previously undated Vico γ eruption occurred around 406.4 ± 1.4
1198 ka (Figs. 15 and 17b), i.e., immediately after the Vico β and Vico β_{top} eruption couple, both with a modelled
1199 age of 406.4 ± 1.3 ka. Fucino provides evidence for three distinct tephra layers (i.e., TF-116, TF-115 and TF-
1200 114) within a very narrow stratigraphic interval of ~9 cm (Table 3; Fig. 5). They represent three distinct eruptive
1201 events of notable intensity occurred in a very short time span and may elude field observations in proximal
1202 exposures. Furthermore, while the uppermost fall deposit of the Sant’Abbondio succession, which is here
1203 tentatively ascribed to the Vico activity (Sant’Angelo tephra), yielded a poorly constrained age of 380 ± 40 ka
1204 (Marra et al., 2014), the Fucino record points out that this eruption cluster likely occurred in a short time span
1205 between ~390 ka and ~389 ka (Figs. 15 and 17b). Finally, the Fucino record allows us to refine the timing of
1206 the early Vico activity, indicating an age of ~377-379 ka for the emplacement of at least two additional,
1207 previously unknown, pyroclastic units (Figs. 15 and 17b).

1208 Regarding the Sabatini volcanic district, the Fucino dataset improves the knowledge on the history and
1209 chronology of the activity, by providing a modelled age of 410.0 ± 2.0 ka for the CC -2 pumice fall (Pereira et
1210 al., 2020). Also, Fucino records a cluster of four tephra (TF-102/TF-106) at ~397-400 ka, which may represent
1211 the equivalent of the Bag Tephra marker(s) of the Middle Pleistocene Hungarian loess, thus providing the first
1212 reliable age and climatostratigraphic position for this stratigraphic marker(s). If confirmed by future
1213 investigations, the recognition of this eruption cluster may shed new light on the Sabatini eruption frequency.
1214 In fact, in the whole eruptive history (589 ± 4 ka to 70 ± 3 ka) of the district, the longest dormancy of ~90 kyr
1215 has been so far documented in the time span 438 ± 1 to 329 ± 4 ka (Marra et al., 2020b). The Fucino dataset,
1216 showing a previously undetected eruption cluster at $398.9 + 2.6/2.9$ ka - $397.5 + 2.8/-3.1$ ka, allows us to
1217 estimate a maximum quiescence of 68.5 ± 4.1 kyr in the district (i.e., same as the time lapse since the last
1218 documented eruption), with implications for hazard assessment in the Roman area. However, at present we

cannot exclude that this cluster of eruptions could originate by the Volsci volcanic field (Fig. 15), which documents activity in a comparable time-span (Table 7).

With respect to the known stratigraphic and chronological framework of Colli Albani volcano (Marra et al., 2003, 2009, 2016b; Freda et al., 2006; Giaccio et al., 2009; Gaeta et al., 2011, 2016), the Fucino dataset integrates the chronology of the post-caldera phase that followed the major Pozzolane Nere eruption. Specifically, the last documented eruption of this phase (i.e., Centogocce succession; Fig. 15) occurs at 396.4 ± 5 ka in the Fucino record, which confirms the 30.6 ± 6.4 kyr-long dormancy preceding the onset of the Villa Senni eruption cycle (365.8 ± 1.4 ka), as previously suggested (Gaeta et al., 2016). Such dormancies have relevance in understanding the relationships between the geodynamic/tectonic and magmatic processes (Marra et al., 2004), stress-field and eruptive activity (Marra et al., 2009), as well as in assessing the volcanic hazard in the Roman area (Marra et al., 2016a, 2020b). In particular, the Colli Albani volcano is characterized by a quasi-periodic eruptive behaviour, with average recurrence times of 41 ± 2 kyr for the onset of the main eruptive cycles and average dormancies of 38 ± 2 kyr (Marra et al., 2016a). Notably, the last eruptive cycle started at 41 ± 2 ka and the last eruption occurred at 36 ± 1 ka, thus strongly evidencing a potentially still active (although quiescent) volcanic system.

Finally, the location of the Fucino paleolake NNW of Roccamonfina volcano is less favourable for intercepting the distal products of major (Plinian and Sub-Plinian) eruption columns (usually dispersed toward the eastern quadrants at these latitudes), different from co-ignimbrite ash clouds and eruptive plumes from minor explosive events subject to lower altitude winds. Nevertheless, the MIS 11 Fucino dataset improves the chronology, both in term of accuracy and precision, of the post-Rio Rava/pre-Brown Leucitic Tuff stage of the Roccamonfina activity, through the identification of a possible distal equivalent of the Mt. Ofelio-Mt. Capitolo parasitic centers (Rouchon et al., 2008).

Overall, based on the updated chronological data for both proximal volcanic areas and Fucino succession, we obtained the probability density functions for the explosive activity of the peri-Tyrrhenian potassic volcanism during the MIS 11 period (Fig. 17c). By comparing these statistical expressions of the regional explosive volcanism, the proximal record would seem to show a single, monotonous increase of the eruptive frequency between ~ 410 ka and ~ 395 ka, followed by a quite homogenous activity during the following 395-365 ka interval. Instead, the better-resolved and richer record derived from Fucino shows a much more complex chronicle. Specifically, the temporal distribution of the peri-Tyrrhenian explosive volcanism is not homogenous and appears significantly clustered, with at least four (or possibly more) ~ 4 -5 kyr-long periods of frequent activity separated by similarly long (5 kyr) periods of declining activity or quiescence. Though intriguing as a feature, here we do not speculate on the possible significance of such cyclicity (e.g., identifying a possible external forcing such as sea level change; Satow et al., 2021; astronomical factors and/or regional tectonics; Marra et al., 2004), as the current analysed record of Fucino is still too short for performing a statistically significant analysis of the frequency distribution of the whole peri-Tyrrhenian potassic explosive activity. We remark that the shape and fluctuation of the reported curve of the temporal distribution (Fig. 17c) does not consider the magnitude and intensity of the events, whereas the actual rate of the erupted volume or mass of magma through time represents an even more important parameter than the mere recurrence interval or frequency of eruptive events. Therefore, further considerations on this key issue are postponed until the complete Fucino tephra record covering the last 430 kyr, or even a longer record, will be retrieved and fully investigated.

1
2
3
4
5
6
7
8
9
10
11
12
13
14
15
16
17
18
19
20
21
22
23
24
25
26
27
28
29
30
31
32
33
34
35
36
37
38
39
40
41
42
43
44
45
46
47
48
49
50
51
52
53
54
55
56
57
58
59
60
61
62
63
64
65

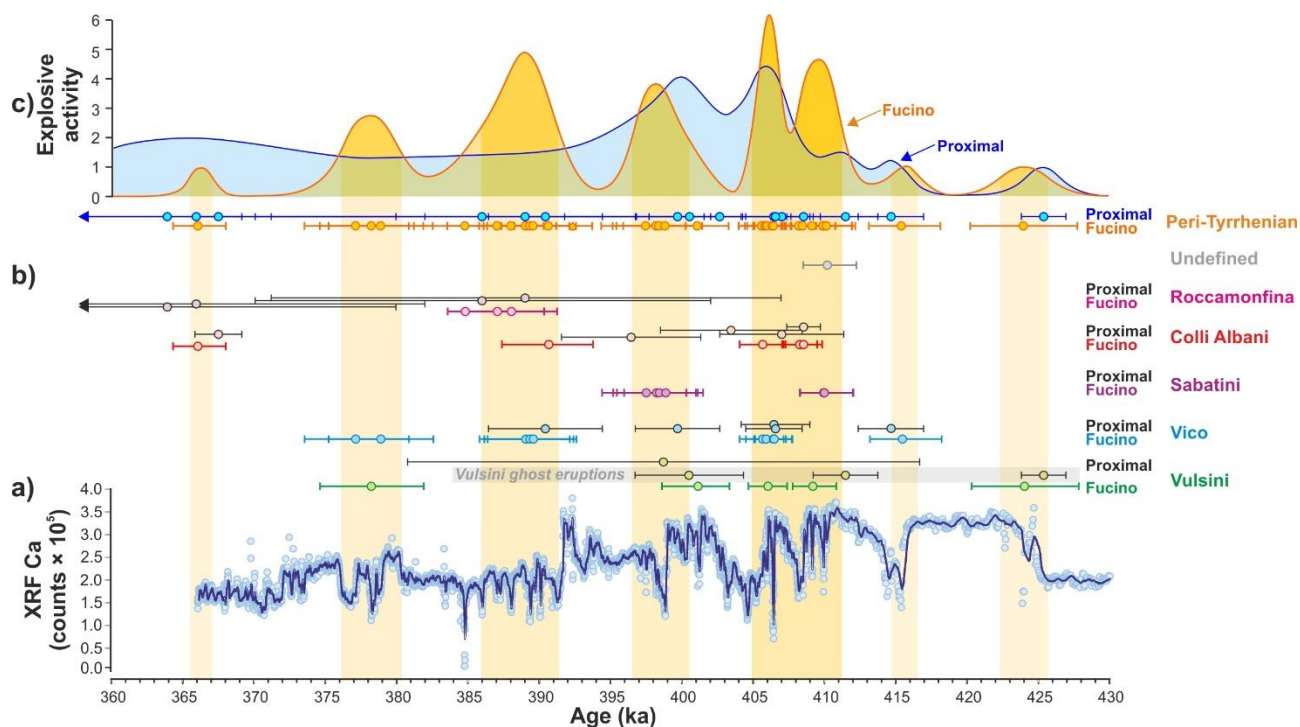


Figure 17. Temporal distribution of the explosive activity of the peri-Tyrrhenian potassic volcanism of central Italy during the 430-360 ka interval, as inferred from the Fucino MIS 11 tephra record and chronological data from proximal volcanic areas. **a)** Temporal series of calcium content of the Fucino lacustrine sediments from F4-F5 core (XRF data from [Giaccio et al., 2019](#)). **b)** Comparison between the Fucino and proximal chronological databases from individual peri-Tyrrhenian volcanoes. **c)** Comparison between the probability density functions of the temporal distribution of the peri-Tyrrhenian explosive activity derived from available chronological data from Fucino and proximal volcanic areas. Source for the $^{40}\text{Ar}/^{39}\text{Ar}$ age of the proximal units: **Vulsini:** [Turbeville \(1992\)](#), [Marra et al. \(2020a\)](#); **Vico:** [Marra et al. \(2014\)](#), [Pereira et al. \(2020\)](#); **Colli Albani:** [Gaeta et al. \(2016\)](#), [Marra et al. \(2016a\)](#); **Roccamonfina:** [Rouchon et al. \(2008\)](#).

6. Summary and concluding remarks

Here, we have presented a comprehensive review of the state-of-the-art Mediterranean tephrochronology and explosive history of the peri-Tyrrhenian potassic volcanoes during the MIS 11 period, in light of new lithostratigraphic, geochemical (major and trace glass composition and multi-phase $^{87}\text{Sr}/^{86}\text{Sr}$ composition) and geochronological ($^{40}\text{Ar}/^{39}\text{Ar}$ dating) characterization of 28 tephra layers from the Fucino F4-F5 succession, as well as of some, potentially equivalent, pyroclastic units collected in proximal areas of the peri-Tyrrhenian potassic volcanoes of central Italy. The integration of these new data with previous investigation from F4-F5 core, results in a record of 32 tephra layers spanning the 430-365 ka interval, thus making Fucino the richest distal archive for this time interval over the entire Mediterranean region. The resulting dataset allowed us to detect the volcanic sources of most of the newly investigated 28 tephra layers and, in many cases, to recognise the specific equivalent eruption or eruptive phase. A Bayesian depth-age model, based on nine, either directly or geochemically correlated $^{40}\text{Ar}/^{39}\text{Ar}$ dated tephra layers, yielded a continuously dated record for the Fucino MIS 11 tephra. A synopsis of all the investigated tephra, along with their volcanic sources, corresponding eruptions and related ages is shown in [Figure 15](#). By combining the updated stratigraphic, geochemical and chronological datasets, we provide an overview of the MIS 11 tephrochronology for the central Mediterranean area ([Fig. 16](#)) and even beyond, as shown here by the finding of the possible equivalent of the Hungarian Bag tephra.

Furthermore, regardless of the limitations of using a single location distal tephra archive to reconstruct past volcanism, the Fucino record clearly documents the eruptive history of the peri-Tyrrhenian explosive volcanoes of central Italy with unprecedented detail and at a higher chronological resolution than all available datasets

1290 from proximal areas. The improved knowledge of the activity histories of Vulcini, Vico, Sabatini, Colli Albani
1291 and Roccamonfina volcanoes, in many cases providing new evidence for previously unidentified eruptions and
1292 substantially improving the chronology of the known ones, sets the ground for refining the eruption timing and
1293 frequency as well as duration of intervening quiescence periods, with key implications for hazard assessment
1294 as well as for identifying cyclic behaviour of the explosive activity (Fig. 17) linked to still unknown external
1295 forcing.
1296 Finally, from a wider methodological point of view, the results of this study strengthen and consolidate the
1297 relevance of the distal tephra archives as fundamental, integrative records for better reconstructing the
1298 behaviour of explosive volcanism, which is crucial for understanding the underlying dynamics and the
1299 assessment of the related hazards. This is particularly true in a perspective of future widening of the network
1300 of records throughout the regions surrounding Quaternary volcanic areas. Such network will be most valuable
1301 for extending the lattice of correlations and for tracing individual tephra layers, which in turn are crucial for both
1302 tephrochronological and volcanological purposes. In this perspective, the Fucino Basin, with its long and
1303 continuous sedimentary history and strategic position, arises as a cornerstone for the development and the
1304 application of this approach in the Mediterranean region for the Quaternary sciences and volcanology.

1305 1306 **Acknowledgments**

1307 This article is a contribution of project “Fucino Tephrochronology Unites Quaternary Records (FUTURE)”,
1308 supported by the Italian Ministry of Education, University and Research (MIUR, grant PRIN No.
1309 20177TKBXZ_003; G. Zanchetta, coordinator). The Fucino project is co-funded by DFG (German Research
1310 Foundation) grant WA 2109/16. $^{40}\text{Ar}/^{39}\text{Ar}$ dating also received complementary contribution from the CNRS
1311 INSU-LEFE 2018-2020 action to S. Nomade. P.G. Albert is supported by a UKRI Future Leaders Fellowship
1312 (MR/S035478/1). INGV, OV laboratories have been also financially supported by the EPOS Research
1313 Infrastructure through the contribution of the Italian Ministry of University and Research (MUR). An early
1314 version of the manuscript benefited from useful comments from Roberto Sulpizio and an anonymous reviewer.

1315 1316 **References**

- 1317
1318 Albert, P.G., Giaccio, B., Isaia, R., Costa, A., Niespolo, E.M., Nomade, S., Pereira, A., Renne, P.R., Hinchliffe, A., Mark,
1319 D.F., Brown, R.J., Smith, V.C., 2019. Evidence for a large-magnitude eruption from Campi Flegrei Caldera (Italy) at 29
1320 ka. *Geology*. <https://doi.org/10.1130/G45805.1>.
1321 Albert, P.G., Smith, V.C., Suzuki, T., Tomlinson, E.L., Nakagawa, T., McLean, D., Yamada, M., Staff, R.A., Scholaut, G.,
1322 Takemura, T., Nagahashi, Y., Kimura, J., Suigetsu 2006 Project Members, 2018. Constraints on the frequency and
1323 dispersal of explosive eruptions at Sambe and Daisen volcanoes (South-West Japan Arc) from the distal Lake Suigetsu
1324 record (SG06 core). *Earth Science Reviews*, 185, 1004-1028.
1325 Amato, V., Aucelli, P.P.C., Cesarano, M., Filocamo, F., Leone, N., Petrosino, P., Roskopf, C.M., Valente, E., Casciello,
1326 E., Giralt, S., Jicha, B.R., 2018. Geomorphic response to late Quaternary tectonics in the axial portion of the Southern
1327 Apennines (Italy): A case study from the Calore River valley. *Earth Surface Processes and Landforms*, 43, 2463-2480.
1328 Amato, V., Aucelli, P.P.C., Cesarano, M., Jicha, B., Lebreton, V., Orain, R., Pappone, G., Petrosino, P., Russo Ermolli, E.,
1329 2014. Quaternary evolution of the largest intermontane basin of the Molise Apennine (Central Southern Italy).
1330 *Rendiconti Lincei*, 25, 197-216.
1331 Belkin, H.E., Rolandi, G., Jackson, J.C., Cannatelli, C., Doherty, A.L., Petrosino, P., De Vivo, B., 2016. Mineralogy and
1332 geochemistry of the older (>40 ka) ignimbrites in the Campanian Plain, southern Italy. *Journal of Volcanology and*
1333 *Geothermal Research*, 323, 1-18.
1334 Bini M., Zanchetta G., Drysdale R.N., Giaccio B., Stocchi P., Vacchi M., Hellstrom J.C., Couchoud I., Monaco L., Ratti A.,
1335 Martini, F., Sarti L., 2020. An end to the Last Interglacial highstand before 120 ka: Relative sea-level evidence from
1336 Infreschi Cave (Southern Italy). *Quaternary Science Reviews* 250, 106658.
1337 Blaauw, M. & Christen, J.A., 2011. Flexible paleoclimate age-depth models using an autoregressive gamma process.
1338 *Bayesian Analysis*, 6:3, 457-474.

61
62
63
64
65

- 1339 Boari, E., Tommasini, S., Laurenzi, M.A., Conticelli, S., 2009. Transition from Ultrapotassic Kamafugitic to Sub-Alkaline
1340 Magmas: Sr, Nd, and Pb Isotope, Trace Element and ^{40}Ar - ^{39}Ar Age Data from the Middle Latin Valley Volcanic Field,
1341 Roman Magmatic Province, Central Italy. *Journal of Petrology*, 50, 7, 1327-1357.
- 1342 Boncio, P., Lavecchia, G., Pace, B., 2004. Defining a model of 3D seismogenic sources for seismic hazard assessment
1343 applications: The case of central Apennines (Italy). *Journal of Seismology*, 8(3), 407-425.
1344 <https://doi.org/10.1023/B:JOSE.0000038449.78801.05>.
- 1345 Bourne, A.J., Albert, P.G., Matthews, I.P., Trincardi, F., Wulf, S., Asioli, A., Blockley, S.P.E., Keller, J., Lowe, J.J., 2015.
1346 Tephrochronology of core PRAD 1-2 from the Adriatic Sea: insights into Italian explosive volcanism for the period 200-
1347 80 ka. *Quaternary Science Reviews*, 116, 28-43.
- 1348 Bourne, A.J., Lowe, J.J., Trincardi, F., Asioli, A., Blockley, S.P.E., Wulf, S., Matthews, I.P., Piva, A., Vigliotti, L., 2010.
1349 Distal tephra record for the last ca 105,000 years from core PRAD 1-2 in the central Adriatic Sea: implications for the
1350 marine tephrostratigraphy. *Quaternary Science Reviews*, 29, 3079-3094.
- 1351 Cardello, G.L., Consorti, L., Palladino, D.M., Carminati, E., Carlini, M., Doglioni, C., 2020. Tectonically controlled
1352 carbonate-seated maar-diatreme volcanoes: The case of the Volsci Volcanic Field, central Italy. *Journals of*
1353 *Geodynamics*, 139, 101763.
- 1354 Cavinato, G.P., Carusi, C., Dell'Asta, M., Miccadei, E., Piacentini T., 2002. Sedimentary and tectonic evolution of Plio-
1355 Pleistocene alluvial and lacustrine deposits of Fucino Basin (central Italy). *Sedimentary Geology*, 148, 29-59.
- 1356 Centamore, E., Dramis, F., Di Manna, P., Fumanti, F., Milli, S., Rossi, D., Palombo, M.R., Palladino, D.M., Triglia, R.,
1357 Zanon, V., Chiocchini, M., Didaskalou, P., Potetti, M., Nisio, S., 2010. Note illustrative del Foglio 402 Ceccano. *Carta*
1358 *Geologica d'Italia 1:50000*. Servizio Geologico d'Italia, Roma.
- 1359 Cioni, R., Sbrana, A., Bertagnini, A., Buonasorte, G., Landi, P., Rossi, U., Salvati, L., 1987. Tephrostratigraphic correlations
1360 in the Vulsini, Vico and Sabatini volcanic succession. *Periodico di Mineralogia*, 56, 137-155.
- 1361 Cross, J.K., Tomlinson, E.L., Giordano, G., Smith, V.S., De Benedetti, A.A., Roberge, J., Manning, C.J., Wulf, S., Menzies,
1362 M.A., 2014. High level triggers for explosive mafic volcanism: Albano Maar, Italy. *Lithos*, 190-191, 137-153.
- 1363 D'Antonio, M., Mariconte, R., Arienzo, I., Mazzeo, F.C., Carandente, A., Perugini, D., Petrelli, M., Corselli, C., Orsi, G.,
1364 Principato, M.S., Civetta, L., 2016. Combined Sr-Nd isotopic and geochemical fingerprinting as a tool for identifying
1365 tephra layers: Application to deep-sea cores from Eastern Mediterranean Sea. *Chemical Geology*, 443, 121-136.
- 1366 D'Agostino, N., Jackson, J. A., Dramis, F., Fucicello, R., 2001. Interactions between mantle upwelling, drainage evolution
1367 and active normal faulting: an example from the central Apennines (Italy). *Geophysical Journal International*, 147(2),
1368 475-497.
- 1369 de Fontaine, C.S., Kaufman, D.S., Anderson, R.S., Werner, A., Waythomass, C.F., Brown, T.A., 2007. Late Quaternary
1370 distal-fall deposits in lacustrine sediments, Kenai Peninsula, Alaska. *Quaternary Research*, 68, 1, 64-78.
- 1371 De Rita, D., Fucicello, R., Parotto, M., 1988. *Carta geologica del complesso vulcanico dei Colli Albani (Vulcano Laziale)*.
1372 C.N.R.-Gruppo Nazionale Vulcanologia.
- 1373 De Rita, D., Giordano, G., Rosa, C., Sheridan, M.F., 1995. Volcanic risk at the Alban Hills volcano and numerical
1374 simulations. In: Triglia, R. (Ed), *The Volcano of the Alban Hills*. Tipografia SGS, Rome, pp. 267-283.
- 1375 De Vivo, B., Rolandi, G., Gans, P.B., Calvert, A., Bohrsen, W.A., Spera, F.J., Belkin, H.E., 2001. New constraints on the
1376 pyroclastic eruptive history of Campanian volcanic Plain (Italy). *Mineralogy and Petrology*, 73, 47-65.
- 1377 Del Carlo, P., Smedile, A., Petrelli, M., Di Roberto, A., 2020. Evidence of an unknown explosive eruption of Mt. Etna
1378 volcano (Italy) during the Late Glacial. *Journal of Volcanology and Geothermal Research*, 402, 106992.
- 1379 Di Roberto, A., Smedile, A., Del Carlo, P., De Martini, P.M., Iorio, M., Petrelli, M., Pantosti, P., Pinzi, S., Todrani, A., 2018.
1380 Tephra and cryptotephra in a ~60,000-year old lacustrine sequence from the Fucino Basin: new insights into the major
1381 explosive events in Italy. *Bulletin of Volcanology*, 80:20.
- 1382 Doglioni, C., Harabaglia, P., Martinelli, G., Mongelli, F., Zito, G., 1996. A geodynamic model of the Southern Apennines
1383 accretionary prism. *Terra Nova*, 8:6, 540-547.
- 1384 Donato, P., Albert, P.G., Crocitti, M., De Rosa, C., Menzies, M.A., 2016. Tephra layers along the southern Tyrrhenian coast
1385 of Italy: Links to the X-5 & X-6 using volcanic glass geochemistry. *Journal of Volcanology and Geothermal Research*,
1386 317, 30-41.
- 1387 Dugmore, A.J., 1989. Icelandic volcanic ash in Scotland. *Scottish Geographical Magazine*, 105:3, 168-172, DOI:
1388 10.1080/14702548908554430.
- 1389 Dugmore, A.J., Newton, A.J., Smith, K.T., Mairs, K.A., 2013. Tephrochronology and the late Holocene volcanic and flood
1390 history of Eyjafjallajökull, Iceland. (2013). *Journal of Quaternary Science*, 28:3, 237-247.
- 1391 Florindo, F., Karner, D.B., Marra, F., Renne, P.R., Roberts A.P., Weaver, R., 2007. Radioisotopic age constraints for
1392 Glacial Terminations IX and VII from aggradational sections of the Tiber River delta in Rome, Italy. *Earth and Planetary*
1393 *Science Letters* 256, 61-80. doi: 10.1016/j.epsl.2007.01.014.
- 1394 Freda, C., Gaeta, M., Giaccio, B., Marra, F., Palladino, D.M., Scarlato, P., Sottili, G., 2011. CO₂-driven large mafic explosive
1395 eruptions: the Pozzolane Rosse case study from the Colli Albani Volcanic District (Italy). *Bulletin of Volcanology*, 73,
1396 241-256.
- 1397 Freda, C., Gaeta, M., Karner, D.B., Marra, F., Renne, P.R., Taddeucci, J., Scarlato, P., Christensen, J.N., Dallai, L., 2006.
1398 Eruptive history and petrologic evolution of the Albano multiple maar (Alban Hills, Central Italy). *Bulletin of Volcanology*,
1399 68, 567-591.
- 1400 Freda, C., Gaeta, M., Palladino, D.M., Trigila, R., 1997. The Villa Senni eruption (Alban Hills, Central Italy): the role of H₂O
1401 and CO₂ on the magma chamber evolution and on the eruptive scenario. *Journal of Volcanology and Geothermal*
1402 *Research*, 78 (1-2), 103-120.
- 1403 Fucicello, R., De Rita, D., Sposato, A., Esposito, A., Fabbri, M., Marsili, P., Mazzini, I., Paccara, P., Trigari, A., Capelli, G.,
1404 Faccenna, C., Fiorentino, A., Mazza, R., Rossetti, F., Sardella, R., Soligo, M., Tuccimei, P., Villa, I.M., 2012. Note
1405 Illustrative della Carta Geologica d'Italia alla scala 1:50.000, Foglio 354 "Tarquinia". Presidenza del Consiglio dei

- 1406 Ministri, Agenzia per la Protezione dell'Ambiente e per i servizi Tecnici: Roma, Italy, Servizio Geologico d'Italia, scale
1407 1:50,000 (in press).
- 1408 Gaeta, M., Freda, C., Christensen, J.N., Dallai, L., Marra, F., Karner, D.B., Scarlato, P., 2006. Time-dependent
1409 geochemistry of clinopyroxene from the Alban Hills (Central Italy): clues to the source and evolution of ultrapotassic
1410 magmas. *Lithos* 86, 330-346.
- 1411 Gaeta, M., Freda, C., Marra F., Arienzo, I., Gozzi, F., Jicha, B., Di Rocco, T., 2016. Paleozoic metasomatism at the origin
1412 of Mediterranean ultrapotassic magmas: Constraints from time-dependent geochemistry of Colli Albani volcanic
1413 products (Central Italy). *Lithos*, 244, 151-164.
- 1414 Gaeta, M., Freda, C., Marra, F., Di Rocco, T., Gozzi, F., Arienzo, I., Giaccio, B., Scarlato, P., 2011. Petrology of the most
1415 recent ultrapotassic magmas from the Roman Province (Central Italy). *Lithos*, 127, 298-308.
- 1416 Galadini, F. & Galli, P., 2000. Active tectonics in the Central Apennines (Italy) - Input Data for Seismic Hazard Assessment.
1417 *Natural Hazards*, 22, 225-270.
- 1418 Gatta, M., Sinopoli, G., Giardini, M., Giaccio, B., Hajdas, I., Pandolfi, L., Bailey, G., Spikins, P., Rolfo, M.F., Sadori, L.,
1419 2016. Pollen from Late Pleistocene hyena (*Crocota Crocota spelaea*) coprolites: An interdisciplinary approach from
1420 two Italian sites. *Review of Palaeobotany and Palynology*, 233, 56-66.
- 1421 Gehrels, M.J., Lowe, D.J., Hazell, Z.J., Newnham, R.M., 2006. A continuous 5300-yr Holocene cryptotephrostratigraphic
1422 record from northern New Zealand and implications for tephrochronology and volcanic hazard assessment. *The*
1423 *Holocene*, 16, 2, 173-187.
- 1424 Giaccio, B., Arienzo, I., Sottili, G., Castorina, F., Gaeta, M., Nomade, S., Galli, P., Messina, P., 2013a. Isotopic (Sr-Nd)
1425 and major element fingerprinting of distal tephra: An application to the Middle-Late Pleistocene markers from the Colli
1426 Albani volcano, central Italy. *Quaternary Science Reviews*, vol. 67, 190-206.
- 1427 Giaccio, B., Castorina, F., Nomade, S., Scardia, G., Voltaggio, M., Sagnotti, L., 2013b. Revised Chronology of the Sulmona
1428 Lacustrine Succession, Central Italy. *Journal of Quaternary Science*, 28, 545-551.
- 1429 Giaccio, B., Galli, P., Messina, P., Peronace, E., Scardia, G., Sottili, G., Sposato, A., Chiarini, E., Jicha, B., Silvestri, S.,
1430 2012b. Fault and basin depocentre migration over the last 2Ma in the L'Aquila 2009 earthquake region, central Italian
1431 Apennines. *Quaternary Science Reviews*, 56, 69-88.
- 1432 Giaccio, B., Galli, P., Peronace, E., Arienzo I., Nomade, S., Cavinato, G.P., Mancini, M., Messina, P., Sottili, G., 2014. A
1433 560-440 ka tephra record from the Mercure Basin, Southern Italy: volcanological and tephrostratigraphic implications.
1434 *Journal of Quaternary Science*, 29, 232-248.
- 1435 Giaccio, B., Leicher, N., Mannella, G., Monaco, L., Regattieri, E., Wagner, B., Zanchetta, G., Gaeta, M., Marra, F., Nomade,
1436 S., Palladino, D.M., Pereira, A., Scheidt, S., Sottili, G., Wonik, T., Wulf, S., Zeeden, C., Ariztegui, D., Cavinato, G.P.,
1437 Dean, R.J., Florindo, F., Leng, M.J., Macri, P., Niespolo, E., Renne, P.R., Rolf, C., Sadori, L., Thomas, C., Tzedakis,
1438 P.C., 2019. Extending the tephra and paleoenvironmental record of the Central Mediterranean back to 430 ka: A new
1439 core from Fucino Basin, central Italy. *Quaternary Science Reviews*, 225, 106003.
- 1440 Giaccio, B., Marra, F., Hajdas, I., Karner, D.B., Renne, P.R., Sposato, A., 2009. ⁴⁰Ar/³⁹Ar and ¹⁴C geochronology of the
1441 Albano maar deposits: Implications for defining the age and eruptive style of the most recent explosive activity at Colli
1442 Albani Volcanic District, Central Italy. *Journal of Volcanology and Geothermal Research*, 185, 203-213.
- 1443 Giaccio, B., Niespolo, E.M., Pereira, A., Nomade, S., Renne, P.R., Albert, P.G., Arienzo, I., Regattieri, E., Wagner, B.,
1444 Zanchetta, G., Gaeta, M., Galli, P., Mannella, G., Peronace, E., Sottili, G., Florindo, F., Leicher, N., Marra, F.,
1445 Tomlinson, E.L., 2017. First integrated tephrochronological record for the last ~190 kyr from the Fucino Quaternary
1446 lacustrine succession, central Italy. *Quaternary Science Reviews*, 158, 211-234.
- 1447 Giaccio, B., Nomade, S., Wulf, S., Isaia, R., Sottili, G., Cavuoto, G., Galli, P., Messina, P., Sposato, A., Sulpizio, R.,
1448 Zanchetta, G., 2012a. The late MIS 5 Mediterranean tephra markers: a reappraisal from peninsular Italy terrestrial
1449 records. *Quaternary Science Reviews*, 56, 31-45.
- 1450 Giaccio, B., Regattieri, E., Zanchetta, G., Nomade, S., Renne, P.R., Sprain, C.J., Drysdale, R.N., Tzedakis, P.C., Messina,
1451 P., Scardia, G., Sposato, A., Bassinot, F., 2015a. Duration and dynamics of the best orbital analogue to the present
1452 interglacial. *Geology*, 43, 603-606.
- 1453 Giaccio, B., Regattieri, E., Zanchetta, G., Wagner, B., Galli, P., Mannella, G., Niespolo, E., Peronace, E., Renne, P.R.,
1454 Nomade, S., Cavinato, G.P., Messina, P., Sposato, A., Boschi, C., Florindo, F., Marra, F., Sadori, L., 2015b. A key
1455 continental archive for the last 2 Ma of climatic history of the central Mediterranean region: A pilot drilling in the Fucino
1456 Basin, central Italy. *Scientific Drilling*, 20, 13-19.
- 1457 Giannetti, B. & De Casa, G., 2000. Stratigraphy, chronology, and sedimentology of ignimbrites from the white trachytic tuff,
1458 Roccamonfina Volcano, Italy. *Journal of Volcanology and Geothermal Research*, 96, 3-4, 243-295.
- 1459 Giannetti, B., 1996a. The geology of the Yellow Trachytic Tuff, Roccamonfina Volcano. *Journal of Volcanology and*
1460 *Geothermal Research*, 71, 1, 53-72.
- 1461 Giannetti, B., 1996b. Volcanology of trachytic and associated basaltic pyroclastic deposits at Roccamonfina volcano,
1462 Roman Region, Italy. *Journal of Volcanology and Geothermal Research*, 71, 2-4, 229-248.
- 1463 Giannetti, B., 2001. Origin of the calderas and evolution of Roccamonfina volcano (Roman Region, Italy). *Journal of*
1464 *Volcanology and Geothermal Research*, 106, 301-319.
- 1465 Giordano, G., De Benedetti, A.A., Diana, A., Diano, G., Gaudio, F., Marasco, F., Miceli, M., Mollo, S., Cas, R.A.F.,
1466 Funciello, R., 2006. The Colli Albani mafic caldera (Roma, Italy): Stratigraphy, structure and petrology. *Journal of*
1467 *Volcanology and Geothermal Research*, 155, 49-80.
- 1468 Goldstein, S.L., Denis, P., Oelkers, E.H., Rudnick, R.L., Walter, L.M., 2003. Standards for publication of isotope ratio and
1469 chemical data in chemical geology. *Chemical Geology*, 202, 1-4.
- 1470 Horváth, E. & Bradák, B., 2014. Sárga föld, lösz, lösz: Short historical overview of loess research and lithostratigraphy in
1471 Hungary. *Quaternary International*, 319, 1-10.
- 1472 Hum, L., 2005. Középső pleisztocén tufithorizontok megjelenése dunaszekcsői és Mórág környéki löszszelvényekben.
1473 *Malakológiai Tájékoztató*, 23, 131-148 (in Hungarian).

- 1474 Insinga, D.D., Tamburrino, S., Lirer, F., Vezzoli, L., Barra, M., De Lange, G.J., Tiepolo, M., Vallefucio, M., Mazzola, S.,
1475 Sprovieri, M., 2014. Tephrochronology of the astronomically-tuned KC01B deep-sea core, Ionian Sea: insights into the
1476 explosive activity of the Central Mediterranean area during the last 200 ka. *Quaternary Science Reviews*, 85, 63-84.
- 1477 Jochum, K.P., Stoll, B., Herwig, K., Willbold, M., Hofmann, A.W., Amini, M., Aarbug, S., Abouchami, W., Hellebrand, E.,
1478 Mocek, B., Raczek, I., Stracke, A., Alard, O., Bouman, C., Becker, S., Dücking, M., Brätz, H., Klemm, R., de Bruin, D.,
1479 Canil, D., Cornell, D., de Hoog, C.-S., Dalpé, C., Danyushevsky, L., Eisenhauer, A., Gao, Y., Snow, J.E., Groschopf,
1480 N., Günther, D., Latkoczy, C., Guillong, M., Hauri, E.K., Höfer, H.E., Lahaye, Y., Horz, K., Jacob, D.E., Kasemann,
1481 S.A., Kent, A.J.R., Ludwig, T., Zack, T., Mason, P.R.D., Meixner, A., Rosner, M., Kisawa, K., Nash, P.B., Pfänder, J.,
1482 Premo, W.R., Sun, W.D., Tiepolo, M., Vannucci, R., Vennemann, T., Wayne, D., Woodhead, J.D., 2006. MPI-DING
1483 reference glasses for in situ microanalysis: New reference values for element concentrations and isotope ratios.
1484 *Geochemistry, Geophysics, Geosystems*, 7:2.
- 1485 Karner, D.B. & Renne, P.R., 1998. ⁴⁰Ar/³⁹Ar geochronology of Roman volcanic province tephra in the Tiber River valley:
1486 Age calibration of middle Pleistocene sea-level changes. *Geological Society of America Bulletin*, 110, 6, 740-747.
- 1487 Karner, D.B., Juvinge, E., Brancaccio, L., Cinque, A., Russo Ermolli, E., Santangelo, L., Bernasconi, S., Lirer, L., 1999. A
1488 potential early middle Pleistocene tephrostratotype for the Mediterranean basin: the Vallo Di Diano, Campania, Italy.
1489 *Global and Planetary Change*, 21, 1-15.
- 1490 Keller, J., Ryan, W.B.F., Ninkovich, D., Altherr, R., 1978. Explosive volcanic activity in the Mediterranean over the last
1491 200,000 yr as recorded in deep-sea sediments. *Geological Society of America Bulletin*, 89, 591-604.
- 1492 Kousis, I., Koutsodendris, A., Peyron, O., Leicher, N., Francke, A., Wagner, B., Giaccio, B., Knipping, M., Pross, J., 2018.
1493 Centennial-scale vegetation dynamics and climate variability in SE Europe during Marine Isotope Stage 11 based on
1494 a pollen record from Lake Ohrid, *Quaternary Science Reviews*, 190, 20-38.
- 1495 Kuehn, S.C., Froese, D.G., Shane, P.A.R., INTAV Intercomparison Participants, 2011. The INTAV intercomparison of
1496 electron-beam microanalysis of glass by tephrochronology laboratories: Results and recommendations. *Quaternary
1497 International*, 246, 19-47.
- 1498 Lane, C.S., Brauer, A., Blockley, S.P.E., Dulski, P., 2013. Volcanic ash reveals time-transgressive abrupt climate change
1499 during the Younger Dryas. *Geology*, 41 (12), 1251-1254.
- 1500 Larsen, G., Róbertsdóttir, B.G., Óladóttir, B.A., Eiríksson, J., 2020. A shift in eruption mode of Hekla volcano, Iceland, 3000
1501 years ago: two-coloured Hekla tephra series, characteristics, dispersal and age. *Journal of Quaternary Science*, 35,
1502 Special Issue 1-2, 143-154.
- 1503 Le Maitre, R.W., Streckeisen, A., Zanettin, B., Le Bas, M.J., Bonin, B., Bateman, P., Bellieni, G., Dudek, A., Efremova, S.,
1504 Keller, J., Lameyre, J., Sabine, P.A., Schmid, R., Sørensen, H., Woolley, A.R., 2002. *Igneous Rocks: A Classification
1505 and Glossary of Terms. Recommendation of the International Union of Geological Sciences Subcommittee on the
1506 Systematics of Igneous Rocks, 2nd Edition.* Cambridge University Press, Cambridge. 236 pages.
- 1507 Lee, J.Y., Marti, K., Severinghaus, J.P., Kawamura, K., Yoo, H.S., Lee, J.B., Kim, J.S., 2006. A redetermination of the
1508 isotopic abundances of atmospheric Ar. *Geochimica and Cosmochimica Acta*, 70, 4507-4512.
- 1509 Leicher, N., Giaccio, B., Zanchetta, G., Wagner, B., Francke, A., Palladino, D.M., Sulpizio, R., Albert, P.G., Tomlinson,
1510 E.L., 2019. Central Mediterranean explosive volcanism and tephrochronology during the last 630 ka based on the
1511 sediment record from Lake Ohrid. *Quaternary Science Reviews*, 226, 106021.
- 1512 Leicher, N., Zanchetta, G., Sulpizio, R., Giaccio, B., Wagner, B., Nomade, S., Francke, A., Del Carlo, P., 2016. First
1513 tephrostratigraphic results of the DEEP site record from Lake Ohrid (Macedonia and Albania). *Biogeosciences*, 13, 2151-
1514 2178.
- 1515 Lisieki, L.E. & Raymo, M.E., 2005. A Pliocene-Pleistocene stack of 57 globally distributed benthic $\delta^{18}\text{O}$ records.
1516 *Paleoceanography*, 20, doi:10.1029/2004PA001071.
- 1517 Lourens, L.J., 2004. Revised tuning of Ocean Drilling Program Site 964 and KC01B (Mediterranean) and implications for
1518 the $d^{18}\text{O}$, tephra, calcareous nannofossil, and geomagnetic reversal chronologies of the past 1.1 Myr.
1519 *Paleoceanography and Paleoclimatology*, 19, PA3010.
- 1520 Lowe, D.J., 2011. Tephrochronology and its application: A review. *Quaternary Geochronology*, 6, 107-153.
- 1521 Luberti, G.M., Marra, F., Florindo, F., 2017. A review of the stratigraphy of Rome (Italy) according to geochronologically
1522 and paleomagnetically constrained aggradational successions, glacio-eustatic forcing and volcano-tectonic processes.
1523 *Quaternary International*, 438, Part B, 40-67.
- 1524 Luhr, J.F. & Giannetti, B., 1987. The Brown Leucitic Tuff of Roccamonfina Volcano (Roman Region, Italy). *Contributions
1525 to Mineralogy and Petrology*, 95, 420-436.
- 1526 Lustrino, M., Duggen, S., Rosenberg, C.L., 2011. The Central-Western Mediterranean: Anomalous igneous activity in an
1527 anomalous collisional tectonic setting. *Earth-Science Reviews*, 104, 1-3, 1-40.
- 1528 Mannella, G., Giaccio, B., Zanchetta, G., Regattieri, E., Niespolo, E.M., Pereira, A., Renne, P.R., Nomade, S., Leicher, N.,
1529 Perchiazzi, N., Wagner, B., 2019. Paleoenvironmental and paleohydrological variability of mountain areas in the central
1530 Mediterranean region: A 190-ka-long chronicle from the independently dated Fucino paleolake record (central Italy).
1531 *Quaternary Science Reviews*, 210, 190-210.
- 1532 Marra, F., Cardello, G.L., Gaeta, M., Jicha, B.R., Montone, P., Niespolo, E.M., Nomade, S., Palladino, D.M., Pereira, A.,
1533 De Luca, G., Florindo, F., Frepoli, A., Renne, P.R., Sottili, G., 2021. The Volsci Volcanic Field (central Italy): eruptive
1534 history, magma system and implications on continental subduction processes. *International Journal of Earth Sciences*.
1535 <https://doi.org/10.1007/s00531-021-01981-6>.
- 1536 Marra, F., Castellano, C., Cucci, L., Florindo, F., Gaeta, M., Jicha, B., Palladino, D.M., Sottili, G., Tertulliani, A., Tolomei,
1537 C., 2020b. Monti Sabatini and Colli Albani: the dormant twin volcanoes at the gates of Rome. *Scientific Reports*
1538 10:8666. <https://doi.org/10.1038/s41598-02-65394-2>.
- 1539 Marra, F., Costantini, L., Di Buduo, G.M., Florindo, F., Jicha, B.R., Monaco, L., Palladino, D.M., Sottili, G., 2019. Combined
1540 glacio-eustatic forcing and volcano-tectonic uplift: geomorphological and geochronological constraints on the Tiber

61
62
63
64
65

1541 River terraces in the eastern Vulsini Volcanic District (central Italy). *Global and Planetary Change*, 182,103009.
1542 doi:10.1016/j.gloplacha.2019.103009.

1543 Marra, F., Freda, C., Scarlato, P., Taddeucci, J., Karner, D.B., Renne, P.R., Gaeta, M., Palladino, D.M., Trigila, R.,
1544 Cavaretta, G., 2003. Post-caldera activity in the Alban Hills volcanic district (Italy): $^{40}\text{Ar}/^{39}\text{Ar}$ geochronology and insights
1545 into magma evolution. *Bulletin of Volcanology*, 65, 227-247.

1546 Marra, F., Gaeta, M., Giaccio, B., Jicha, B.R., Palladino, D.M., Polcari, M., Sottili, G., Taddeucci, J., Florindo, F.,
1547 Stramondo, S., 2016a. Assessing the volcanic hazard for Rome: $^{40}\text{Ar}/^{39}\text{Ar}$ and In-SAR constraints on the most recent
1548 eruptive activity and present-day uplift at Colli Albani Volcanic District. *Geophysical Research Letters*, 43, 6898-6906.

1549 Marra, F., Jicha, B., Florindo, F., 2017. $^{40}\text{Ar}/^{39}\text{Ar}$ dating of Glacial Termination VI: constraints to the duration of Marine
1550 Isotopic Stage 13. *Scientific Reports*, 7, 8908. doi:10.1038/s41598-017-08614-6

1551 Marra, F., Jicha, B., Palladino, D.M., Gaeta, M., Costantini, L., Di Buduo, G.M., 2020a. $^{40}\text{Ar}/^{39}\text{Ar}$ single crystal dates from
1552 pyroclastic deposits provide a detailed record of the 590-240 ka eruptive period at the Vulsini Volcanic District (central
1553 Italy). *Journal of Volcanology and Geothermal Research*, 398, 106904.

1554 Marra, F., Karner, D.B., Freda, C., Gaeta, M., Renne, P., 2009. Large mafic eruptions at Alban Hills Volcanic District
1555 (Central Italy): chronostratigraphy, petrography and eruptive behavior. *Journal of Volcanology and Geothermal
1556 Research*, 179, 217-232.

1557 Marra, F., Nomade, S., Pereira, A., Petronio, C., Salari, L., Sottili, G., Bahain, J.J., Boschian, G., Di Stefano, G., Falguères,
1558 C., Florindo, F., Gaeta, M., Giaccio, B., Masotta, M., 2018. A review of the geological sections and the faunal
1559 assemblages of Aurelian Mammal Age of Latium (Italy) in the light of a new chronostratigraphic framework. *Quaternary
1560 Science Reviews*, 181, 173-199.

1561 Marra, F., Rohling, E.J., Florindo, F., Jicha, B., Nomade, S., Pereira, A., Renne, P.R., 2016b. Independent $^{40}\text{Ar}/^{39}\text{Ar}$ and
1562 ^{14}C age constraints on the last five glacial terminations from the aggradational successions of the Tiber River, Rome
1563 (Italy). *Earth and Planetary Science Letters*, 449, 105-117.

1564 Marra, F., Sottili, G., Gaeta, M., Giaccio, B., Jicha, B., Masotta, M., Palladino, D.M., Deocampo, D.M., 2014. Major
1565 explosive activity in the Monti Sabatini Volcanic District (central Italy) over the 800-390 ka interval: geochronological-
1566 geochemical overview and tephrostratigraphic implications. *Quaternary Science Reviews*, 94, 74-101.

1567 Marra, F., Taddeucci, J., Freda, C., Marzocchi, W., Scarlato, P., 2004. Recurrence of volcanic activity along the Roman
1568 Comagmatic Province (Tyrrhenian margin of Italy) and its tectonic significance. *Tectonics*, 23, TC4013.

1569 Matthews, I.P., Trincardi, F., Lowe, J.J., Bourne, A.J., MacLeod, A., Abbott, P.M., Andersen, N., Asioli, A., Blockley, S.P.E.,
1570 Lane, C.S., Oh, Y.A., Satow, C.S., Staff, R.A., Wulf, S., 2015. Developing a robust tephrochronological framework for
1571 Late Quaternary marine records in the Southern Adriatic Sea: new data from core station SA03-11. *Quaternary Science
1572 Reviews*, 118, 84-104.

1573 Mcmanus, J., Oppo, D., Cullen, J., & Healey, S. 2003. Marine isotope stage 11 (MIS 11): analog for Holocene and future
1574 Climate? Earth's climate and orbital eccentricity: the marine isotope stage 11 question, 137, 69-85.

1575 Morabito, S., Petrosino, P., Milia, A., Sprovieri, M., Tamburrino, S., 2014. A multidisciplinary approach for reconstructing
1576 the stratigraphic framework of the last 40 ka in a bathyal area of eastern Tyrrhenian Sea. *Global and Planetary Change*,
1577 123, Part A, 121-138.

1578 Munno, R. & Petrosino, P., 2007. The late Quaternary tephrostratigraphical record of the San Gregorio Magno basin
1579 (southern Italy). *Journal of Quaternary Science*, 22, 247-266.

1580 Nappi, G., Renzulli, A., Santi, P., Gillot, Y.P., 1995. Geological evolution and geochronology of the Vulsini volcanic district
1581 (central Italy): *Bollettino della Società Geologica Italiana*, v. 114, p. 599-613.

1582 Narcisi, B. & Vezzoli, L., 1999. Quaternary stratigraphy of distal tephra layers in the Mediterranean - an overview. *Global
1583 and Planetary Change*, 21, 31-50.

1584 Newnham, R.M., Lowe, D.J., Alloway, B.V., 1999. Volcanic hazards in Auckland, New Zealand: a preliminary assessment
1585 of the threat posed by central North Island silicic volcanism based on the Quaternary tephrostratigraphical record.
1586 Geological Society, London, Special Publications, 161, 27-45.

1587 Niespolo, E.M., Rutte, D., Deino, A.L., Renne, P.R., 2017. Intercalibration and age of the Alder Creek Sanidine $^{40}\text{Ar}/^{39}\text{Ar}$
1588 standard. *Quaternary Geochronology*, 39, 205-213.

1589 Nomade, S., Bassinot, F., Mariano, M., Simon, Q., Dewilde, F., Maiorano, P., Isguder, G., Blamart, D., Gironi, A., Scao,
1590 V., Pereira, A., Toti, F., Bertini, A., Combourieu-Nebout, N., Peral, M., Bourlès, D.L., Petrosino, P., Gallicchio, S.,
1591 Ciaranfi, N., 2019. High-resolution foraminifer stable isotope record of MIS 19 at Montalbano Jonico, southern Italy: A
1592 window into Mediterranean climatic variability during a low-eccentricity interglacial. *Quaternary Science Reviews*, 205,
1593 106-125.

1594 Nomade, S., Gauthier, A., Guillou, H., Pastre, J.-F., 2010. $^{40}\text{Ar}/^{39}\text{Ar}$ temporal framework for the Alleret maar lacustrine
1595 sequence (French Massif-Central): Volcanological and paleoclimatic implications. *Quaternary Geochronology*, 5:1, 20-
1596 27.

1597 Nomade, S., Muttoni, G., Guillou, H., Robin, E., Scardia, G., 2011. First $^{40}\text{Ar}/^{39}\text{Ar}$ age of the Ceprano man (central Italy).
1598 *Quaternary Geochronology*, 6, 453-457.

1599 Palladino, D.M., Agosta, E., Freda, C., Spaziani, S., Trigila, R., 1994. Geo-petrographic and volcanological study of
1600 Southern Vulsini: the Valentano–Marta–La Rocca sector. *Memorie Descrittive della Carta Geologica d'Italia*, 49, 255–
1601 276.

1602 Palladino, D.M., Simeì, S., Sottili, G., Trigila, R., 2010. Integrated approach for the reconstruction of stratigraphy and
1603 geology of Quaternary volcanic terrains: an application to the Vulsini Volcanoes (central Italy). In: Groppelli, G., Viereck,
1604 e L. (Eds.), *Stratigraphy and Geology in Volcanic Areas*. Geological Society of America Special Paper, 464, 66–84.

1605 Patacca, E., Scandone, P., Di Luzio, E., Cavinato, G.P., Parotto, M., 2008. Structural architecture of the central Apennines:
1606 Interpretation of the CROP 11 seismic profile from the Adriatic coast to the orographic divide. *Tectonics*, 27, TC3006,
1607 doi:10.1029/2005TC001917.

- 1608 Paterne, M., Guichard, F., Duplessy, J.C., Siani, G., Sulpizio, R., Labeyrie, J., 2008. A 90,000-200,000 yrs marine tephra
1609 record of Italian volcanic activity in the Central Mediterranean Sea. *Journal of Volcanology and Geothermal Research*,
1610 177, 187-196.
- 1611 Paterne, M., Guichard, F., Labeyrie, J., 1988. Explosive activity of the south Italian volcanoes during the past 80,000 years
1612 as determined by marine tephrochronology. *Journal of Volcanology and Geothermal Research*, 34, 153-172.
- 1613 Paterne, M., Guichard, F., Labeyrie, J., Gillot, P.Y., Duplessy, J.C., 1986. Tyrrhenian Sea tephrochronology of the oxygen
1614 isotope record for the past 60,000 years. *Marine Geology*, 72, 259-285.
- 1615 Peccerillo, A., 2017. Cenozoic Volcanism in the Tyrrhenian Sea Region. In: IAVCEI, *Advances in Volcanology*, 2 ed.
1616 Springer, p. 400.
- 1617 Pereira, A., Monaco, L., Marra, F., Sébastien, N., Gaeta, M., Leicher, N., Palladino, D.M., Sottili, G., Guillou, H., Scao, V.,
1618 Giaccio, B., 2020. Tephrochronology of the central Mediterranean MIS 11c interglacial (~425-395 ka): New constraints
1619 from the Vico volcano and the Tiber delta, central Italy. *Quaternary Science Reviews*, 243, 106-470.
- 1620 Pereira, A., Nomade, S., Moncel, M.H., Voinchet, P., Bahain, J.J., Biddittu, I., Falgueres, C., Giaccio, B., Manzi, G., Parenti,
1621 F., Scardia, G., Scao, V., Sottili, G., Vietti, A., 2018. Integrated geochronology of Acheulian sites from the southern
1622 Latium (central Italy): insights on human-environment interaction and the technological innovations during the MIS 11-
1623 MIS 10 period. *Quaternary Science Reviews*, 187, 112-129.
- 1624 Perini, G. & Conticelli, S., 2002. Crystallization conditions of leucite-bearing magmas and their implications on the
1625 magmatological evolution of ultrapotassic magmas: the Vico Volcano, central Italy. *Mineralogy and petrology*, 74, 253-
1626 276.
- 1627 Perini, G., Conticelli, S., Francalanci, L., 1997. Inferences on the volcanic history of the Vico volcano, Roman Magmatic
1628 Province, central Italy: stratigraphic, petrographic and geochemical data. *Mineralogica et Petrographica Acta*, 40, 67-
1629 93.
- 1630 Perini, G., Conticelli, S., Francalanci, L., Davidson, J. P., 2000. The relationship between potassic and calc-alkaline post-
1631 orogenic magmatism at Vico volcano, central Italy. *Journal of Volcanology and Geothermal Research*, 95, 243-268.
- 1632 Perini, G., Francalanci, L., Davidson, J.P., Conticelli, S., 2004. Evolution and Genesis of Magmas from Vico Volcano,
1633 Central Italy: Multiple Differentiation Pathways and Variable Parental Magmas. *Journal of Petrology*, 45:1, 139-182.
- 1634 Perini, G., Teplei III, F.-J., Davidson, J.P., Conticelli, S., 2003. The origin of K-feldspar megacrysts hosted in alkaline
1635 potassic rocks from central Italy: a track for low-pressure processes in mafic magmas. *Lithos*, 66, 223-240.
- 1636 Petrosino, P., Arienzo, I., Mazzeo, F.C., Natale, J., Petrelli, M., Milia, A., Perugini, D., D'Antonio, M., 2019. The San
1637 Gregorio Magno lacustrine basin (Campania, southern Italy): improved characterization of the tephrostratigraphic
1638 markers based on trace elements and isotopic data. *Journal of Quaternary Science*, 34, 393-404.
- 1639 Petrosino, P., Jicha, B.R., Mazzeo, F.C., Ciaranfi, N., Girone, A., Maiorano, P., 2015. The Montalbano Jonico marine
1640 succession: An archive for distal tephra layers at the Early-Middle Pleistocene boundary in southern Italy. *Quaternary
1641 International*, 383, 89-103.
- 1642 Petrosino, P., Jicha, B.R., Mazzeo, F.C., Russo Ermolli, E., 2014b. A high-resolution tephrochronological record of MIS
1643 14-12 in the Southern Apennines (Acerno Basin, Italy). *Journal of Volcanology and Geothermal Research*, 274, 34-50.
- 1644 Petrosino, P., Morabito, S., Jicha, B.R., Milia, A., Sprovieri, M., Tamburrino, S., 2016. Multidisciplinary tephrochronological
1645 correlation of marker events in the eastern Tyrrhenian Sea between 48 and 105 ka. *Journal of Volcanology and
1646 Geothermal Research*, 315, 79-99.
- 1647 Petrosino, P., Russo Ermolli, E., Donato, P., Jich, B., Robustelli, G., Sardella, R., 2014a. Using tephrochronology and
1648 palynology to date the MIS 13 lacustrine sediments of the Mercure basin (Southern Apennines - Italy). *Italian Journal
1649 of Geosciences*, 133, 169-186.
- 1650 Ponomareva, V.V., Portnyagin, M., Davies, S.M., 2015. Tephra without borders: far-reaching clues into past explosive
1651 eruptions. *Front. Earth Sci.* 3 (83). <https://doi.org/10.3389/feart.2015.00083>
- 1652 Pouclot, A., Horvat, E., Gabris, G., Juvigné, E., 1999. The Bag tephra, a widespread tephrochronological marker in Middle
1653 Europe: chemical and mineralogical investigations. *Bulletin of Volcanology*, 60, 265-272.
- 1654 R Core Team (2017). R: A Language and Environment for Statistical Computing.
- 1655 Radicati di Brozolo, F., Di Girolamo, P., Turi, B., Oddone, M., 1988. ⁴⁰Ar-³⁹Ar and K-Ar dating of K-rich rocks from the
1656 Roccamonfina Volcano, Roman Comagmatic Region, Italy. *Geochimica et Cosmochimica Acta*, 52, 1435-1441.
- 1657 Regattieri, E., Giaccio, B., Galli, P., Nomade, S., Peronace, E., Messina, P., Sposato, A., Boschi, C., Gemelli, M., 2016. A
1658 multi-proxy record of MIS 11-12 deglaciation and glacial MIS 12 instability from the Sulmona Basin (central Italy).
1659 *Quaternary Science Reviews*, 132, 129-145.
- 1660 Regattieri, E., Giaccio, B., Mannella, G., Zanchetta, G., Nomade, S., Tognarelli, A., Perchiazzi, N., Vogel, H., Boschi, C.,
1661 Drysdale, R.N., Wagner, B., Gemelli, M., Tzedakis, P., 2019. Frequency and dynamics of millennial-scale variability
1662 during marine isotope stage 19: insights from the Sulmona Basin (central Italy). *Quaternary Science Reviews*, 214, 28-
1663 43.
- 1664 Regattieri, E., Giaccio, B., Zanchetta, G., Drysdale, R.N., Galli, P., Nomade, S., Peronace, E., Wulf, S., 2015. Hydrological
1665 variability over the Apennines during the Early Last Glacial precession minimum, as revealed by a stable isotope
1666 record from Sulmona basin, Central Italy. *Journal of Quaternary Science*, 30, 19-31.
- 1667 Renne, P.R., Balco, G., Ludwig, K.R., Mundil, R., Min, K., 2011. Response to the comment by WH Schwarz et al. on "Joint
1668 determination of 40 K decay constants and ⁴⁰Ar/⁴⁰K for the Fish Canyon sanidine standard, and improved accuracy
1669 for ⁴⁰Ar/³⁹Ar geochronology" by PR Renne et al. (2010). *Geochimica et Cosmochimica Acta*, 75, 5097-5100.
- 1670 Renne, P.R., Sprain, C.J., Richards, M.A., Self, S., Vanderkluyzen, L., Pande, K., 2015. State shift in Deccan volcanism
1671 at the Cretaceous Paleogene boundary, possibly induced by impact. *Science*, 350, 76-78.
- 1672 Rolandi, G., Bellucci, F., Heizler, M.T., Belkin, H.E., De Vivo, B., 2003. Tectonic controls on the genesis of ignimbrite from
1673 the Campanian Volcanic Zone, southern Italy. *Mineralogy and Petrology*, 79, 3-31.
- 1674 Rouchon, V., Gillot, P.Y., Quidelleur, X., Chiesa, S., Floris, B., 2008. Temporal evolution of the Roccamonfina volcanic
1675 complex (Pleistocene), Central Italy. *Journal of Volcanology and Geothermal Research*, 177, 500-514.

- 1676 Russo Ermolli, E., Aucelli, P.P.C., Di Rollo, A., Mattei, M., Petrosino, P., Porreca, M., Roszkopf, C.M., 2010. An integrated
1677 stratigraphical approach to the Middle Pleistocene succession of the Sessano Basin (Molise, Italy). *Quaternary*
1678 *International*, 225, 114-127.
- 1679 Sági, T., Kiss, B., Bradák, B., Harangi, S., 2008. Középső-pleisztocén löszben előforduló vulkáni képződmények
1680 Magyarországon: terepi és petrográfiai jellemzők (Middle Pleistocene volcanic sediments in loess in Hungary: field and
1681 petrographical characteristics). *Földtani Közlelöny*, 138, 297-310 (in Hungarian with English abstract).
- 1682 Sagnotti, L., Scardia, G., Giaccio, B., Liddicoat, J.C., Nomade, S., Renne, P.R., Sprain, C.J., 2014. Extremely rapid
1683 directional change during Matuyama-Brunhes geomagnetic polarity reversal. *Geophysical Journal International*, 199,
1684 1110-1124.
- 1685 Satow, C., Gudmundsson, A., Gertisser, R., Ramsey, C. B., Bazargan, M., Pyle, D., Wulf, S., Miles, A., Hardiman, M.,
1686 2021. A sea-level control on the eruptive activity of Santorini volcano, Greece. *Nature Geoscience*.
- 1687 Sbrana, A., Marianelli, P., Pasquini, G., 2018. Volcanology of Ischia (Italy). *Journal of Maps*, 14, 2.
- 1688 Scaillet, S., Vita-Scaillet, G., Guillou, H., 2008. Oldest human footprints dated by Ar/Ar. *Earth and Planetary Science*
1689 *Letters*, 275, 320-325.
- 1690 Simon, Q., Bourlès, D.L., Thouveny, N., Horg, C.-S., Valet, J.-P., Bassinot, F., Choy, S., 2018. Cosmogenic signature of
1691 geomagnetic reversals and excursions from the Réunion event to the Matuyama-Brunhes transition (0.7-2.14 Ma
1692 interval). *Earth and Planetary Science Letters*, 482, 510-524.
- 1693 Smith, V.C., Isaia, R., Pearce, N.J.G., 2011. Tephrostratigraphy and glass compositions of post-15 kyr Campi Flegrei
1694 eruptions: implications for eruption history and chronostratigraphic markers. *Quaternary Science Reviews*, 30, 3638-
1695 3660.
- 1696 Soligo, M. & Tuccimei, P., 2010. Geochronology of Colli Albani volcano. In: Funicello, R., Giordano, G. (eds). *The Colli*
1697 *Albani Volcano*. Geological Society of London, Special IAVCEI Publication, 3:99-106.
- 1698 Sottili, G., Arienzo, I., Castorina, F., Gaeta, M., Giaccio, B., Marra, F., Palladino, D.M., 2019. Time-dependent Sr and Nd
1699 isotope variations during the evolution of ultrapotassic Sabatini Volcanic District (Roman Province, Central Italy).
1700 *Bulletin of Volcanology*, 81:67.
- 1701 Sottili, G., Palladino, D.M., Marra, F., Jicha, B., Karner, D.B., Renne, P., 2010. Geochronology of the most recent activity
1702 in the Sabatini volcanic district, Roman Province, central Italy. *Journal of Volcanology and Geothermal Research*, 196,
1703 20-30.
- 1704 Sottili, G., Palladino, D.M., Zanon, V., 2004. Plinian activity during the early eruptive history of the Sabatini volcanic district,
1705 central Italy. *Journal of Volcanology and Geothermal Research*, 135, 361-379.
- 1706 Tamburrino, S., Insinga, D.D., Sprovieri, M., Petrosino, P., Tiepolo, M., 2012. Major and trace element characterization of
1707 tephra layers offshore Pantelleria Island: insights into the last 200 ka of volcanic activity and contribution to the Med-
1708 iterranean tephrochronology. *Journal of Quaternary Science*, 27, 129-140.
- 1709 Thirlwall, M.F., 1991. Long-term reproducibility of multicollector Sr and Nd isotope ratio analysis. *Chemical Geology*, 94:85-
1710 104.
- 1711 Thorarinnsson, 1981a. Greetings from Iceland. *Geografiska Annaler: Series A, Physical Geography*, 63:3-4, 109-118, DOI:
1712 10.1080/04353676.1981.11880024.
- 1713 Thorarinnsson, 1981b. Tephra studies and tephrochronology: a historical review with special reference to Iceland. In: S.
1714 Self, R.S.J., Sparks (Eds.), *Tephra Studies*, Reidel, Dordrecht (1981), pp. 1-12.
- 1715 Tomlinson, E.L., Albet, P.G., Wulf, S., Brown, R.J., Smith, V.C., Keller, J., Orsi, G., Bourne, A., Menzes, M.A., 2014. Age
1716 and geochemistry of tephra layers from Ischia, Italy: constraints from proximal-distal correlations with Lago Grande di
1717 Monticchio. *Journal of Volcanology and Geothermal Research*, 287, 22-39.
- 1718 Tomlinson, E.L., Arienzo, I., Civetta, L., Wulf, S., Smith, V.C., Hardiman, M., Lane, C.S., Carandente, A., Orsi, G., Rosi,
1719 M., Müller, W., Menzies, M.A., 2012. Geochemistry of the Phlegrean Fields (Italy) proximal sources for major
1720 Mediterranean tephra: Implications for the dispersal of Plinian and co-ignimbritic components of explosive eruptions.
1721 *Geochimica et Cosmochimica Acta*, 93, 102-128.
- 1722 Tomlinson, E.L., Smith, V.C., Albert, P.G., Aydar, E., Civetta, L., Cioni, R., Çubukçu, E., Gertisser, R., Isaia, R., Menzies,
1723 M.A., Orsi, G., Rosi, M., Zanchetta, G., 2015. The major and trace element glass compositions of the productive
1724 Mediterranean volcanic sources: tools for correlating distal tephra layers in and around Europe. *Quaternary Science*
1725 *Reviews*, 118, 48-66.
- 1726 Tomlinson, E.L., Thordarson, T., Muller, W., Thirlwall, M.T., Menzies, M.A., 2010. Microanalysis of tephra by LA-ICP-MS -
1727 strategies, advantages and limitations assessed using the Thorsmork ignimbrite (Southern Iceland). *Chemical Geology*,
1728 279, 73-89.
- 1729 Turbeville, B.N., 1992. ⁴⁰Ar/³⁹Ar ages and Stratigraphy of the Latera caldera, Italy. *Bulletin of Volcanology*, 55, 110-118.
- 1730 Turbeville, B.N., 1993. Petrology and Petrogenesis of the Latera Caldera, Central Italy. *Journal of Petrology*, 34:1, 77-123.
- 1731 Tzedakis, P.C. 2010. The MIS 11–MIS 1 analogy, southern European vegetation, atmospheric methane and the "early
1732 anthropogenic hypothesis". *Climate of the Past*, 6(2), 131-144.
- 1733 Vakhrameeva, P., Koutsodendris, A., Wulf, S., Fletcher, W.J., Appelt, O., Knipping, M., Gertisser, R., Trieloff, M., Pross,
1734 J., 2018. The cryptotephra record of the Marine Isotope Stage 12 to 10 interval (460-335 ka) at Tenaghi Philippon,
1735 Greece: Exploring chronological markers for the Middle Pleistocene of the Mediterranean region. *Quaternary Science*
1736 *Reviews*, 200, 313-333.
- 1737 Vakhrameeva, P., Koutsodendris, A., Wulf, S., Portnyagin, M., Appelt, O., Ludwig, T., Trieloff, M., Pross, J., 2021. Land-
1738 sea correlations in the Eastern Mediterranean region over the past c. 800 kyr based on macro- and cryptotephra from
1739 ODP Site 964 (Ionian Basin). *Quaternary Science Reviews*, 255, 106811.
- 1740 Vakhrameeva, P., Wulf, S., Koutsodendris, A., Tjallingii, R., Fletcher, W.J., Appelt, O., Ludwig, T., Knipping, M., Trieloff,
1741 M., Pross, J., 2019. Eastern Mediterranean volcanism during. Marine isotope stages 9 to 7e (335-235 ka): Insights

1742 based on cryptotephra layers at Tenaghi Philippon, Greece. *Journal of Volcanology and Geothermal Research*, 380,
1743 31-47.

1744 Villa, P., Soriano, S., Grün, R., Marra, F., Nomade, S., Pereira, A., Boschian, G., Pollarolo, L., Fang, F., Bahain, J.J., 2016.
1745 The Acheulian and early Middle Paleolithic in Central Italy: Stability and Innovation. *PLoS ONE* 11, e0160516.
1746 doi:10.1371/journal.pone.0160516.

1747 Wagner, B., Vogel, H., Francke, A., Friederich, T., Donders, T., Lacey, J.H., Leng, M.J., Regattieri, E., Sadori, L., Wilke,
1748 T., Zanchetta, G., Albrecht, C., Bertini, A., Combourieu-Nebout, N., Cvetkoska, A., Giaccio, B., Grazhdani, A., Hauffe,
1749 T., Holtvoeth, J., Joannin, S., Lagoos, M., Leicher, N., Levkov, Z., Lindhorst, K., Masi, A., Melles, M., Mercuri, A.M.,
1750 Nomade, S., Nowaczyk, N., Panagiotopoulos, K., Peyron, O., Reed, J.M., Sagnotti, L., Sinopoli, G., Stellbrink, B.,
1751 Sulpizio, R., Timmermann, A., Tofilovska, S., Torri, P., Wagner-Cremer, F., Wonik, T., Zhang, X., 2019. Mediterranean
1752 winter rainfall in phase with African monsoons during the past 1.36 million years. *Nature*, 573, 256-260.

1753 Washington, H.S., 1906. The Roman comagmatic region. Carnegie Institution of Washington, Publication 57, 199 pp.

1754 Wastergård, S., 2002. Early to middle Holocene silicic tephra horizons from Katlavolcanic system, Iceland: new results
1755 from the Faroe Islands. *Journal of Quaternary Science*, 17:8, 723-730.

1756 Wulf, S., Keller, J., Paterne, M., Mingram, J., Lauterbach, S., Opitz, S., Sottili, G., Giaccio, B., Albert, P.G., Satow, C.,
1757 Tomlinson, E.L., Viccaro, M., Brauer, A., 2012. The 100-133 ka record of Italian explosive volcanism and revised
1758 tephrochronology of Lago Grande di Monticchio. *Quaternary Sciences Reviews*, 58, 104-123.

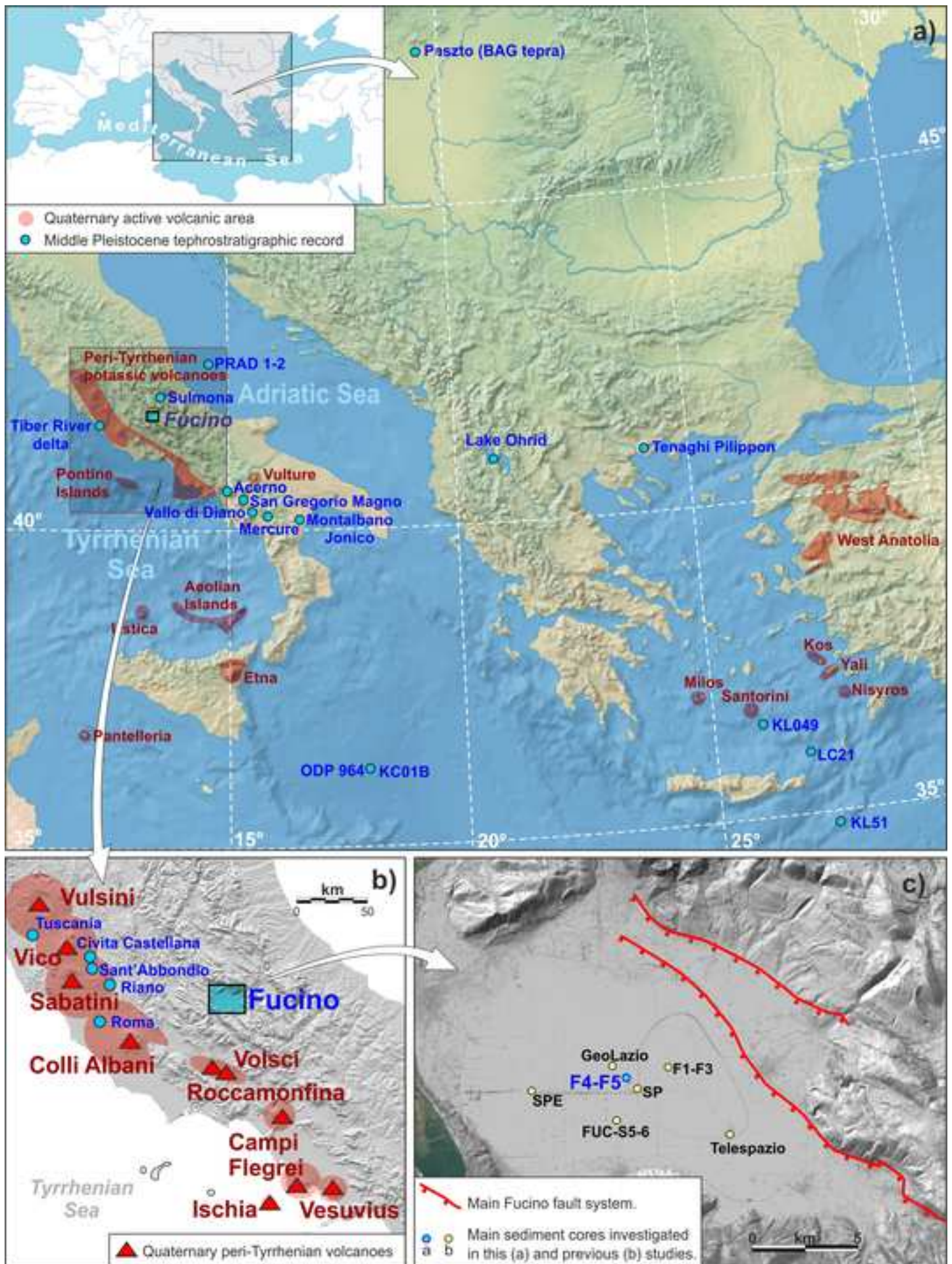
1759 Wulf, S., Keller, J., Satow, C., Gertisser, R., Kraml M., Grant, K.M., Appelt, O., Vakhrameeva, P., Koutsodendris, A.,
1760 Hardiman, M., Schulz, H., Pross, J., 2020. Advancing Santorini's tephrostratigraphy: New glass geochemical data and
1761 improved marine-terrestrial tephra correlations for the past ~360 kyrs. *Earth-Science Reviews*, 200, 102964.

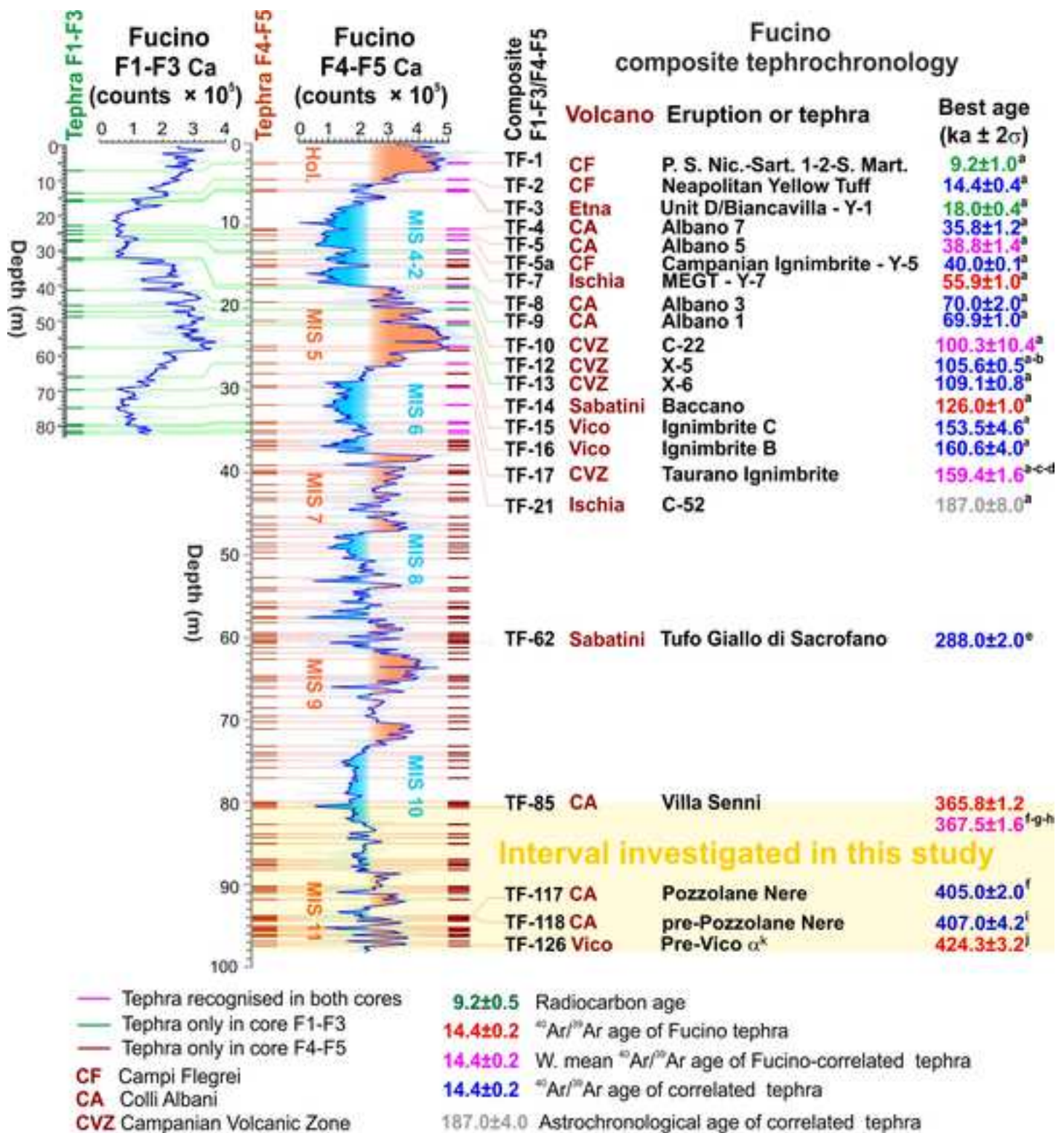
1762 Wulf, S., Kraml, M., Keller, J., 2008. Towards a detailed tephrostratigraphy in the Central Mediterranean: The last 20,000
1763 yrs record of Lago Grande di Monticchio. *Journal of Volcanology and Geothermal Research*, 177, 118-132.

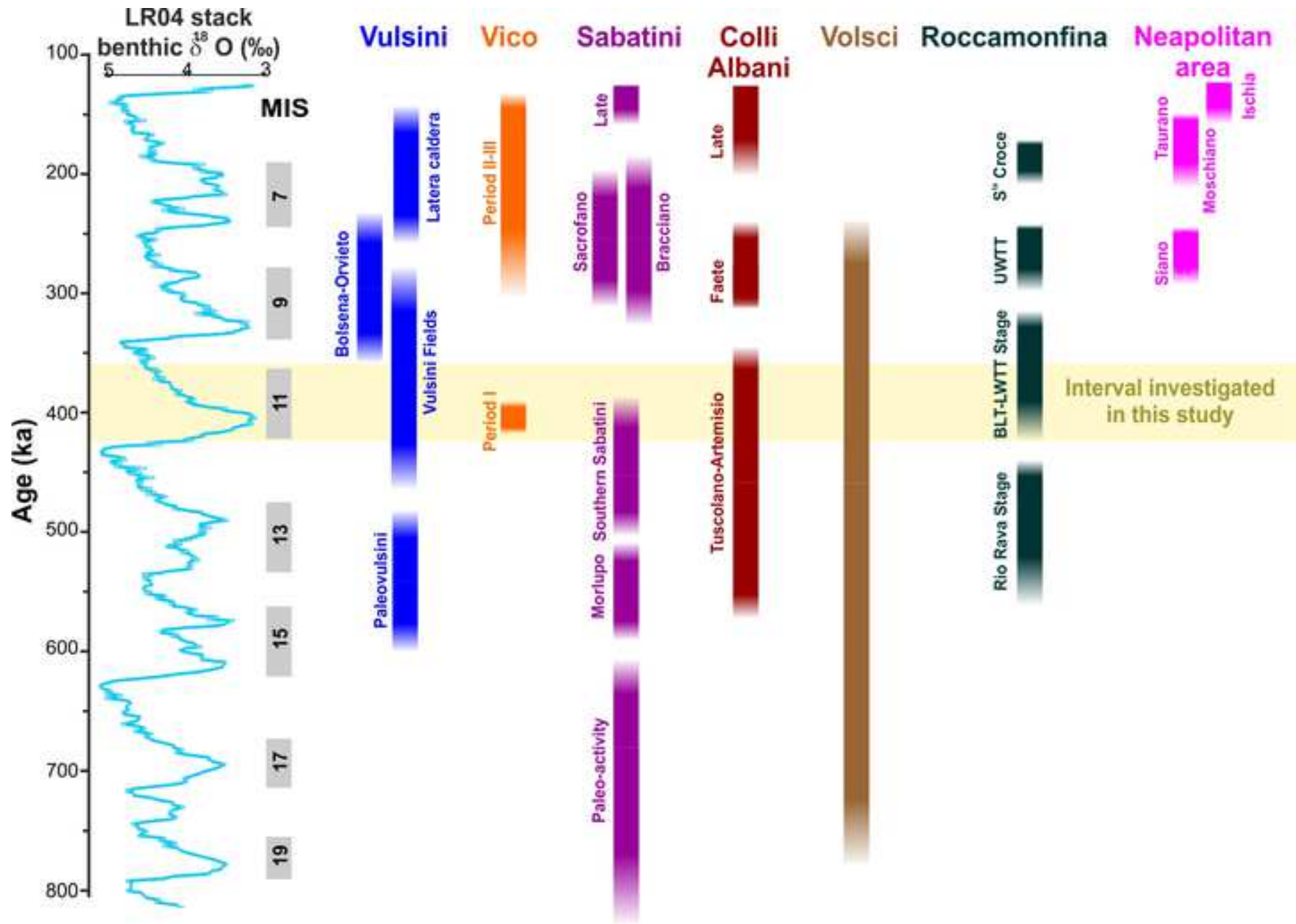
1764 Wulf, S., Kraml, M., Brauer, A., Keller, J., Negendank, J.F.W., 2004. Tephrochronology of the 100 ka lacustrine sediment
1765 record of Lago Grande di Monticchio (Southern Italy). *Quaternary International*, 122, 7-30.

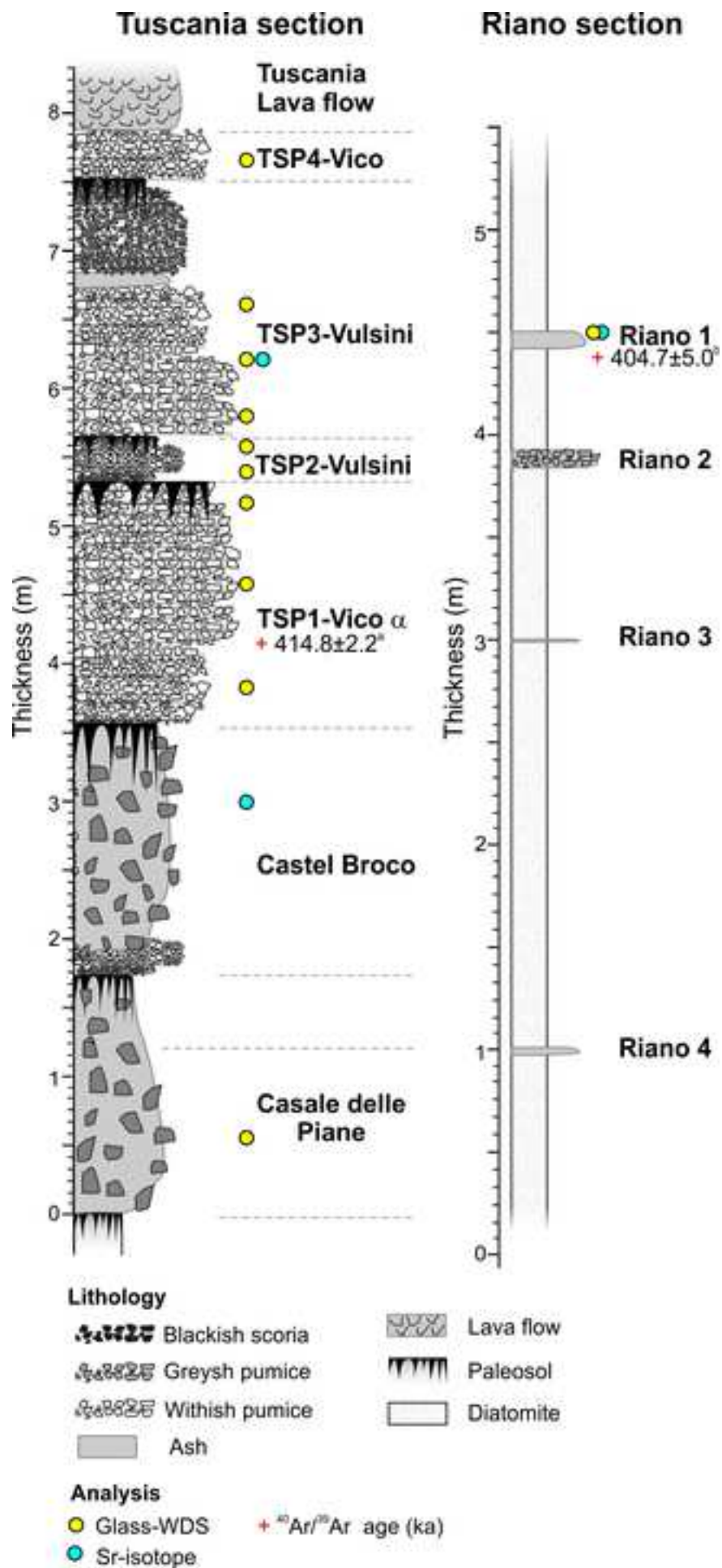
1766 Zanchetta, G., Giaccio, B., Bini, M., Sarti, L., 2018. Tephrostratigraphy of Grotta del Cavallo, Southern Italy: insights of the
1767 chronology of Middle to Upper Paleolithic transition in the Mediterranean. *Quaternary Science Reviews*, 182, 65-77.

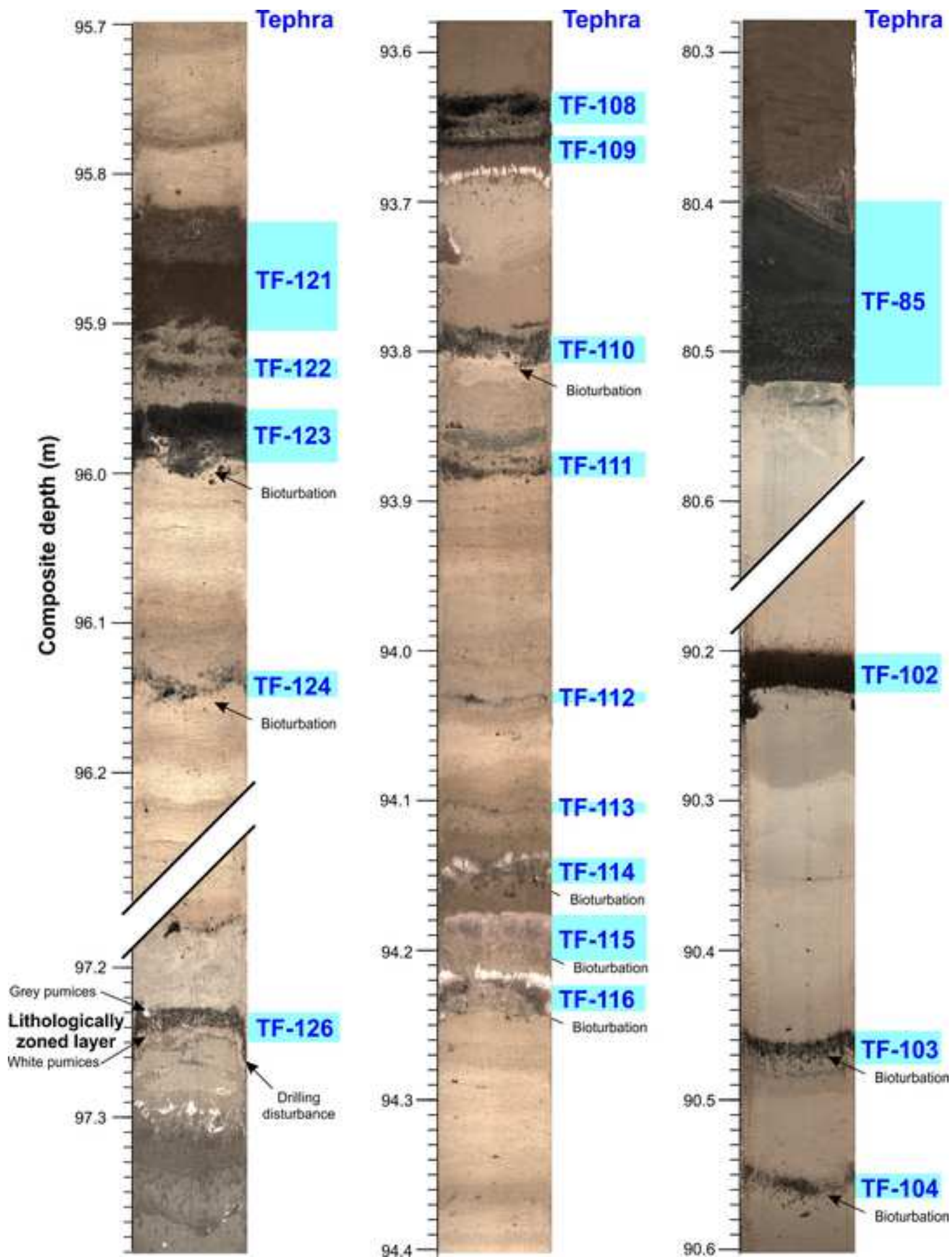
1768
24
25
26
27
28
29
30
31
32
33
34
35
36
37
38
39
40
41
42
43
44
45
46
47
48
49
50
51
52
53
54
55
56
57
58
59
60
61
62
63
64
65

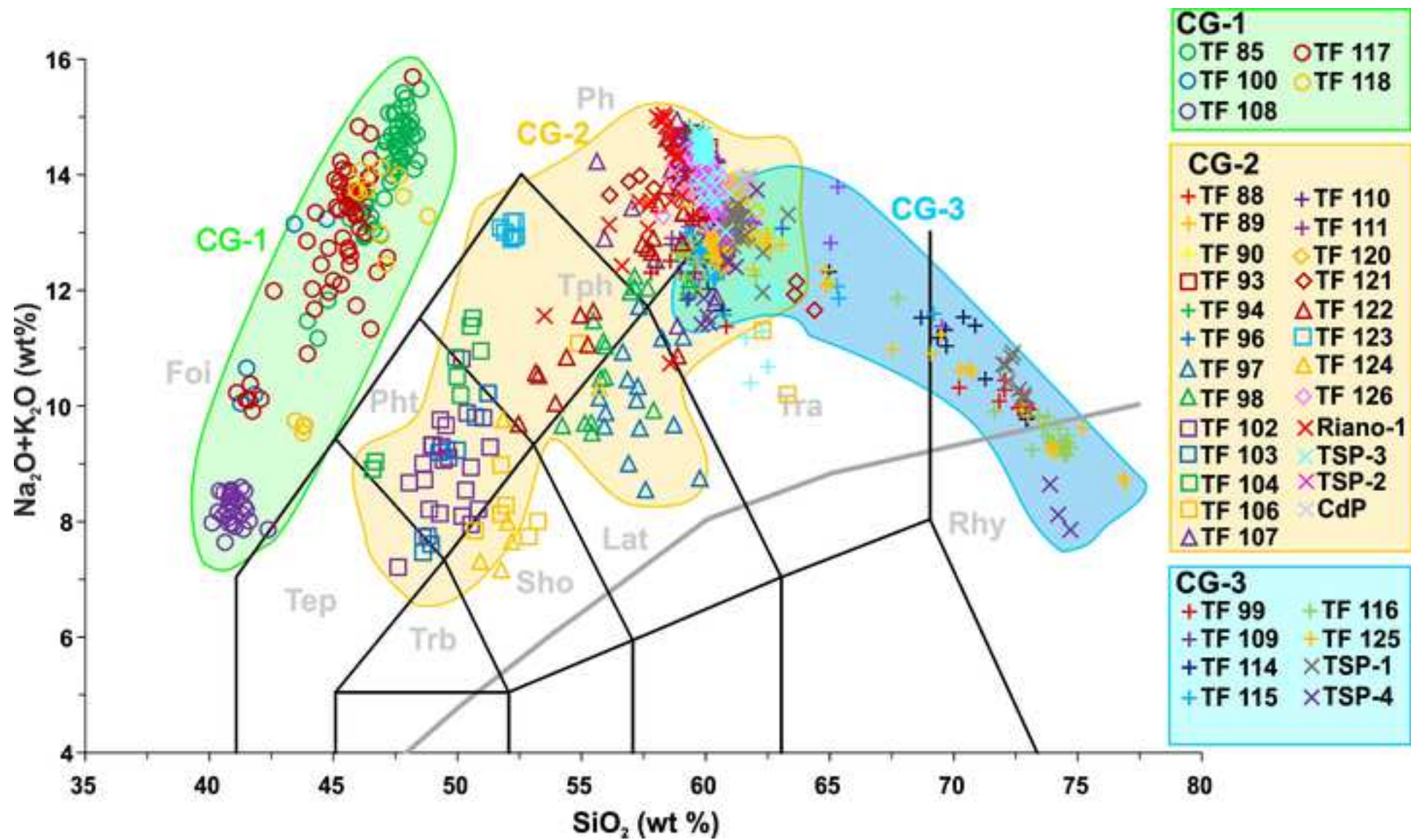


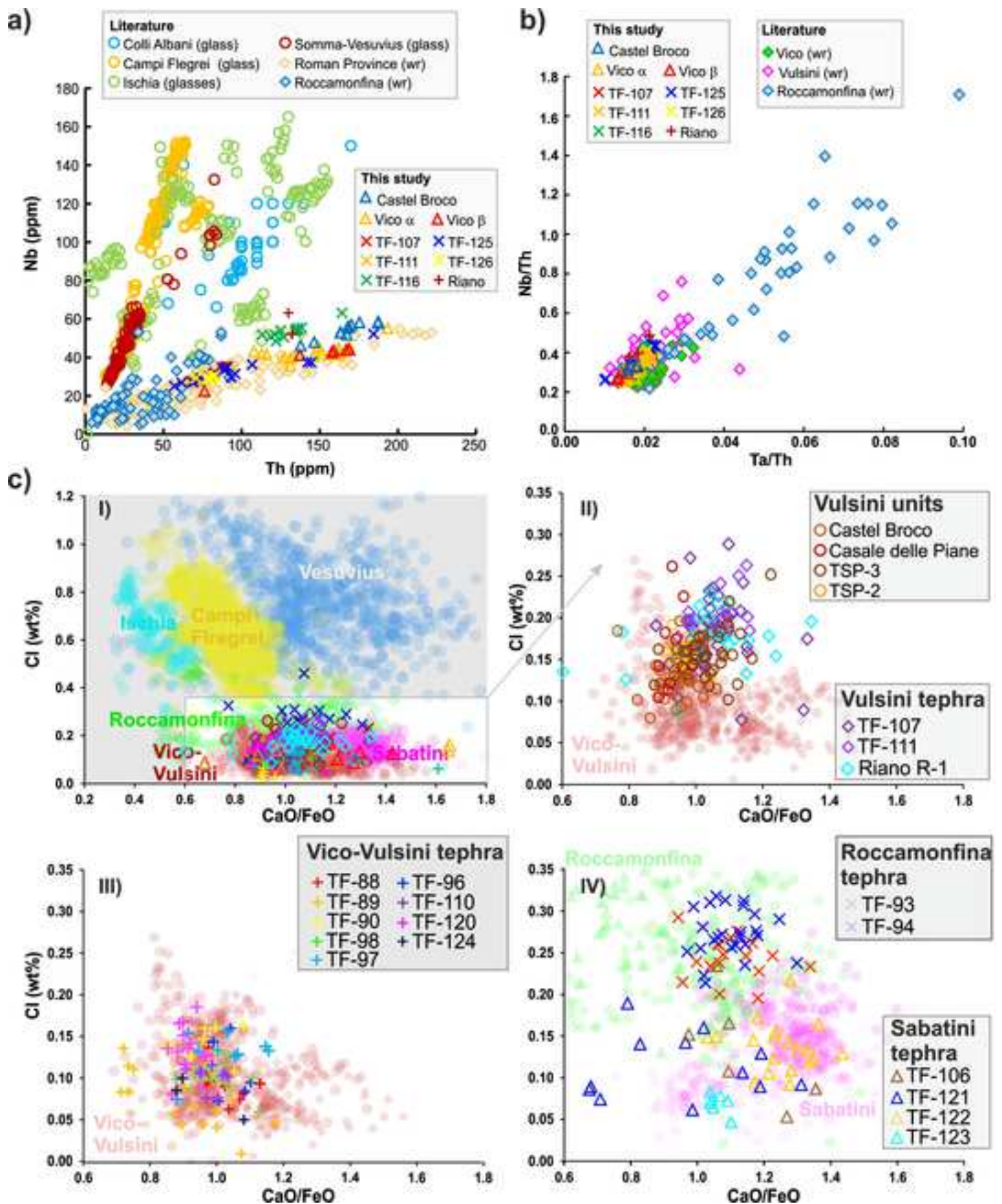


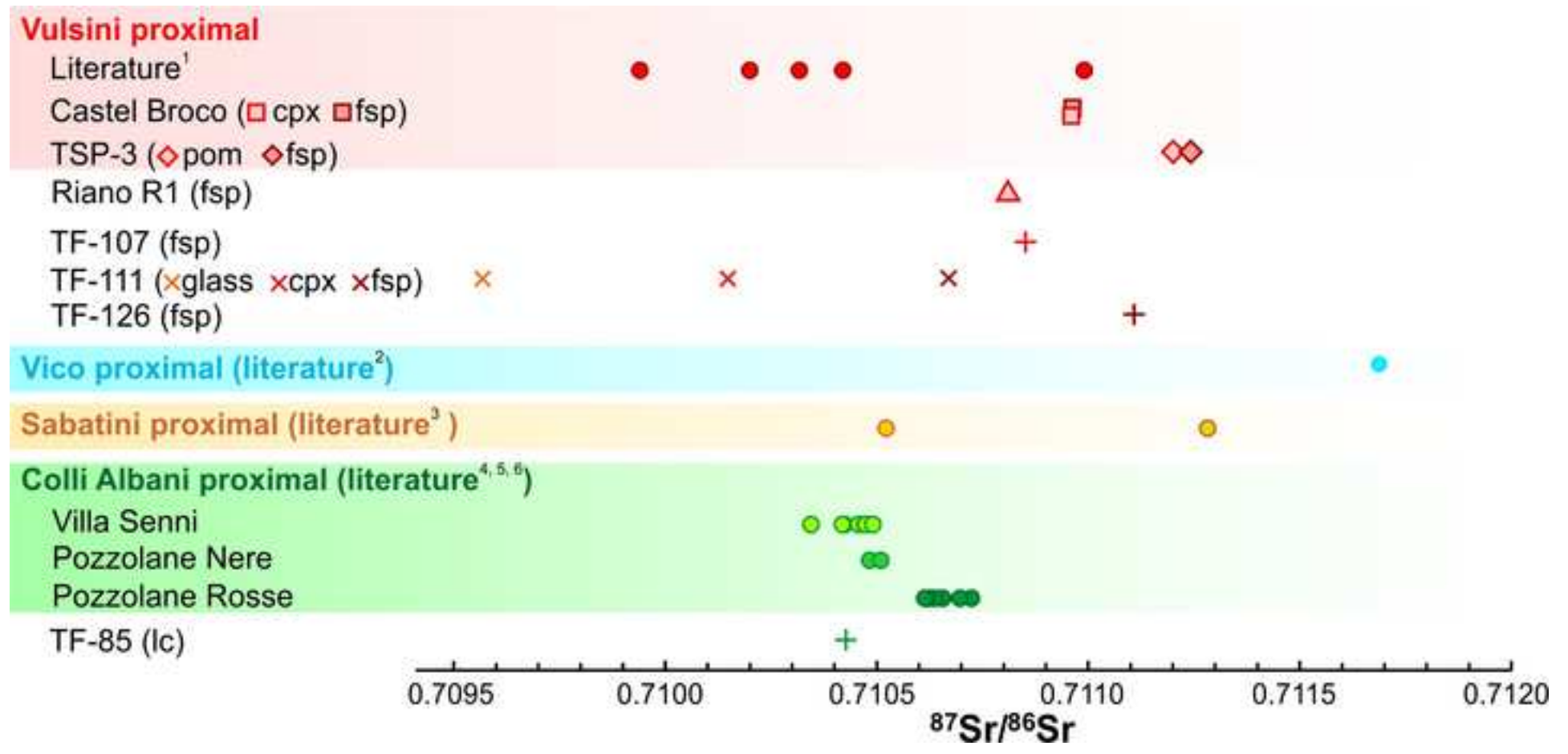


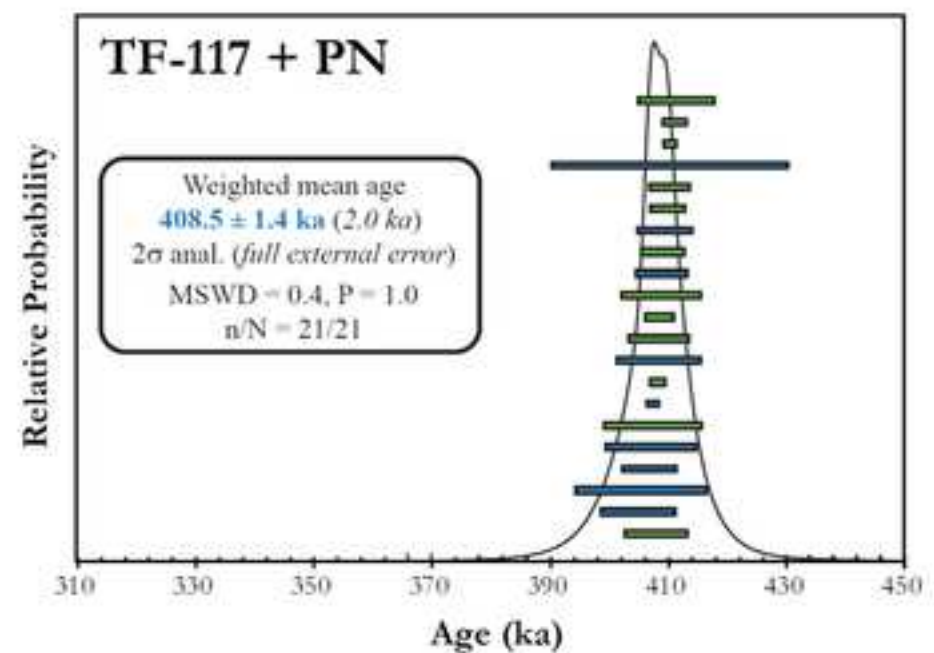
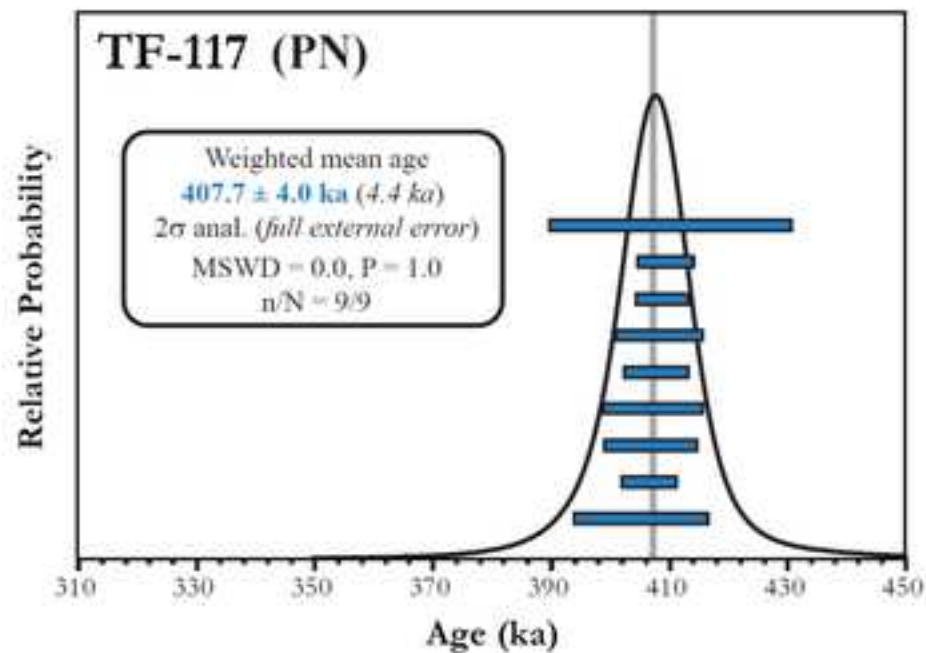
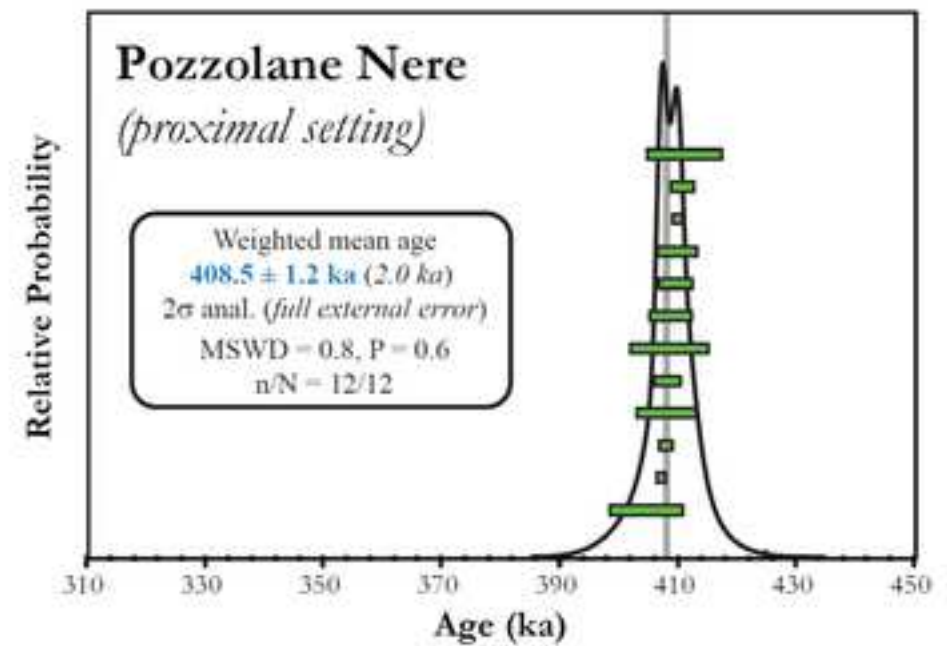
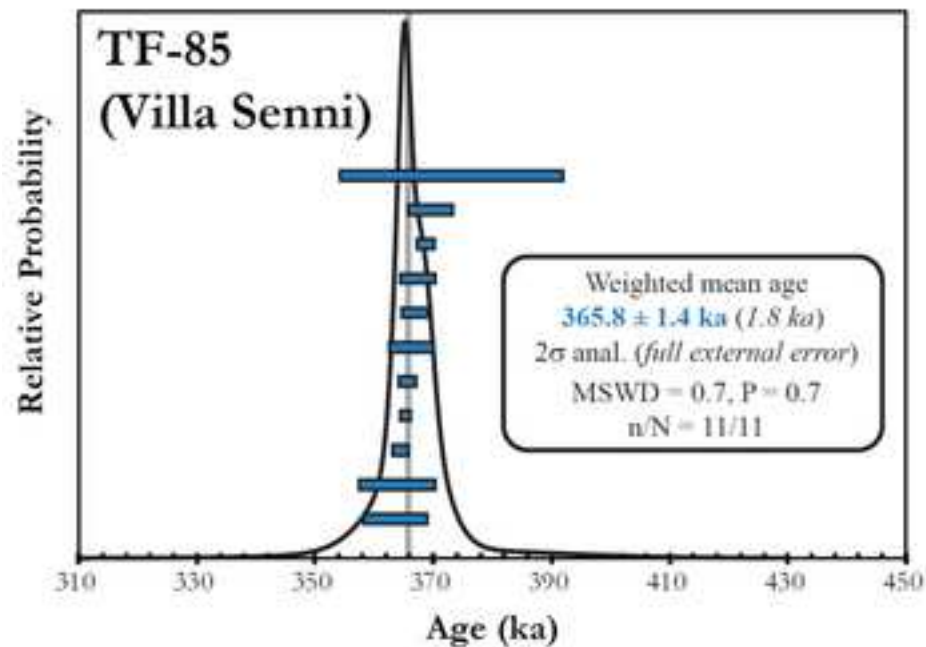




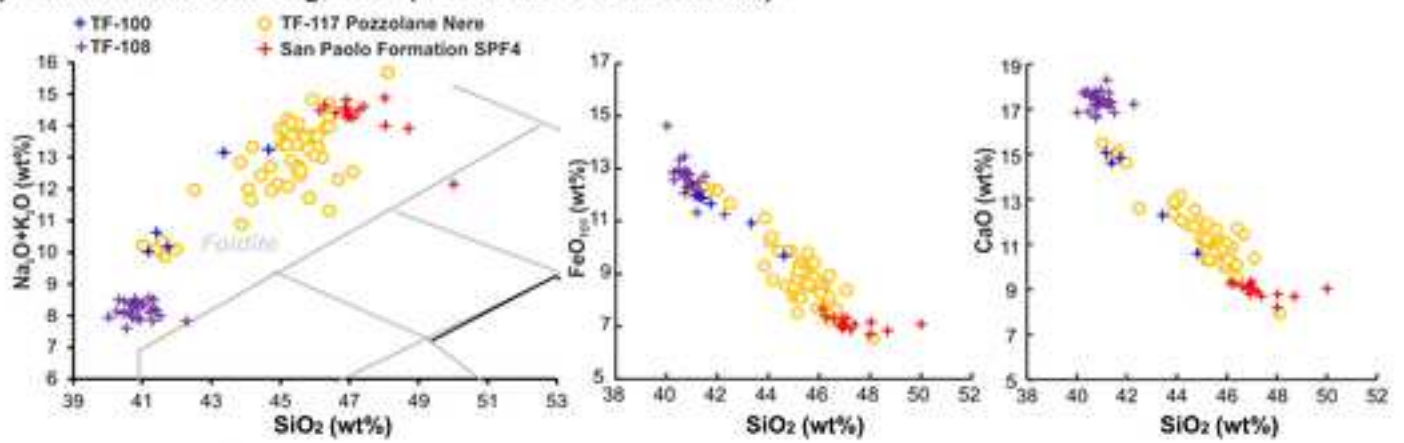




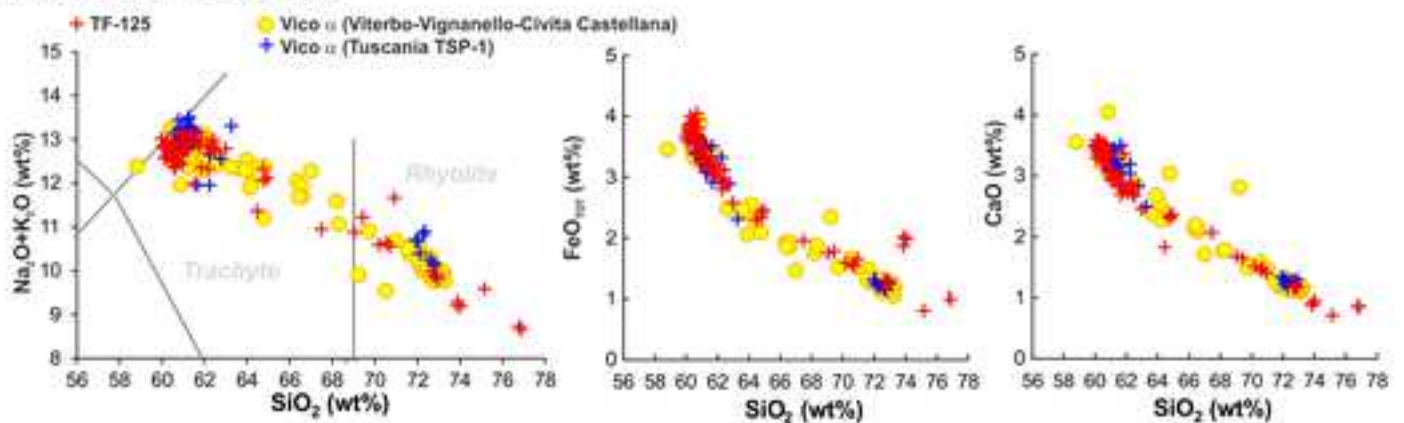




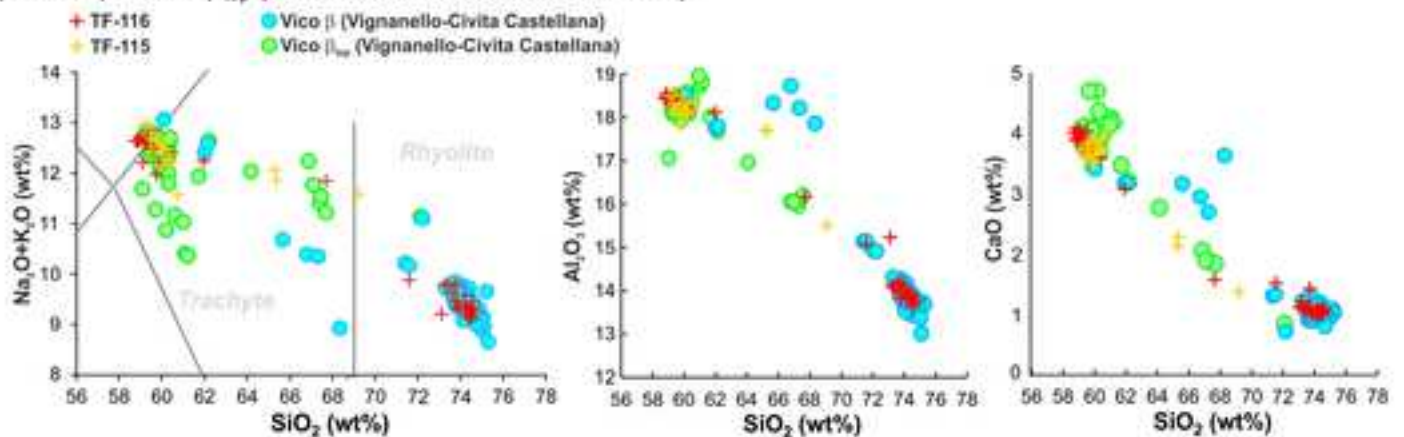
a) Colli Albani Centogocce (402.7±5.0-396.7±5.0 ka)



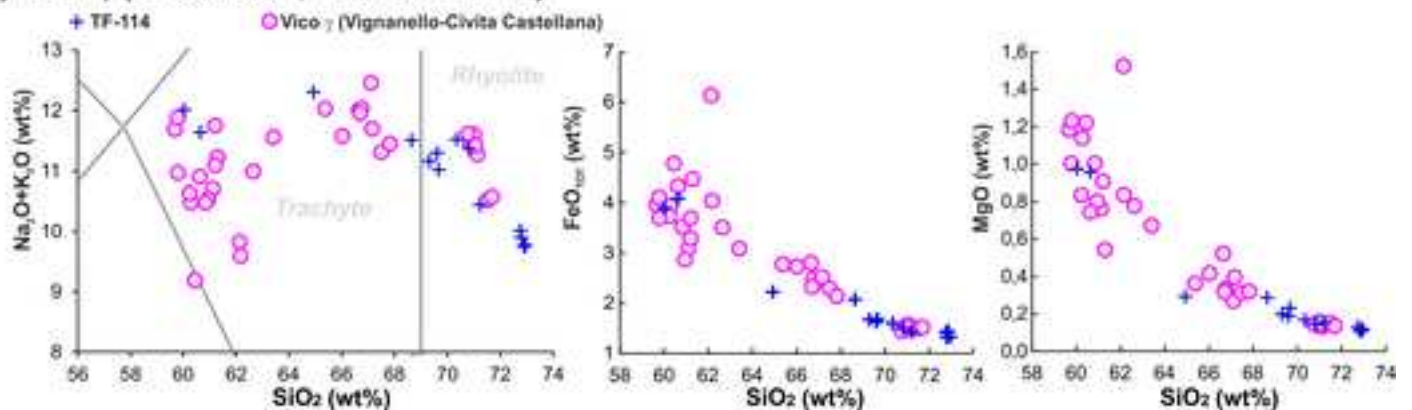
b) Vico α (414.8±2.2 ka)



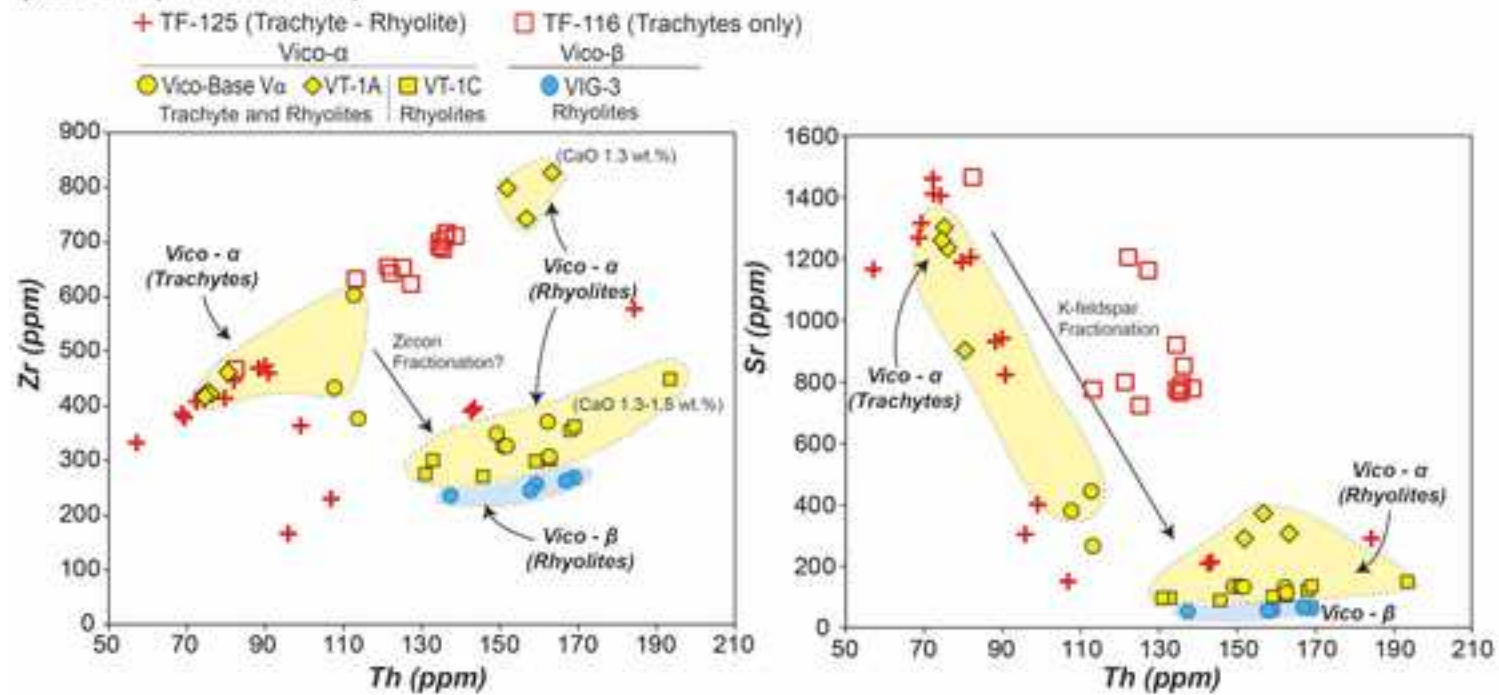
c) Vico β -Vico β_{top} (406.5±2.4 ka - 406.2±2.0 ka)



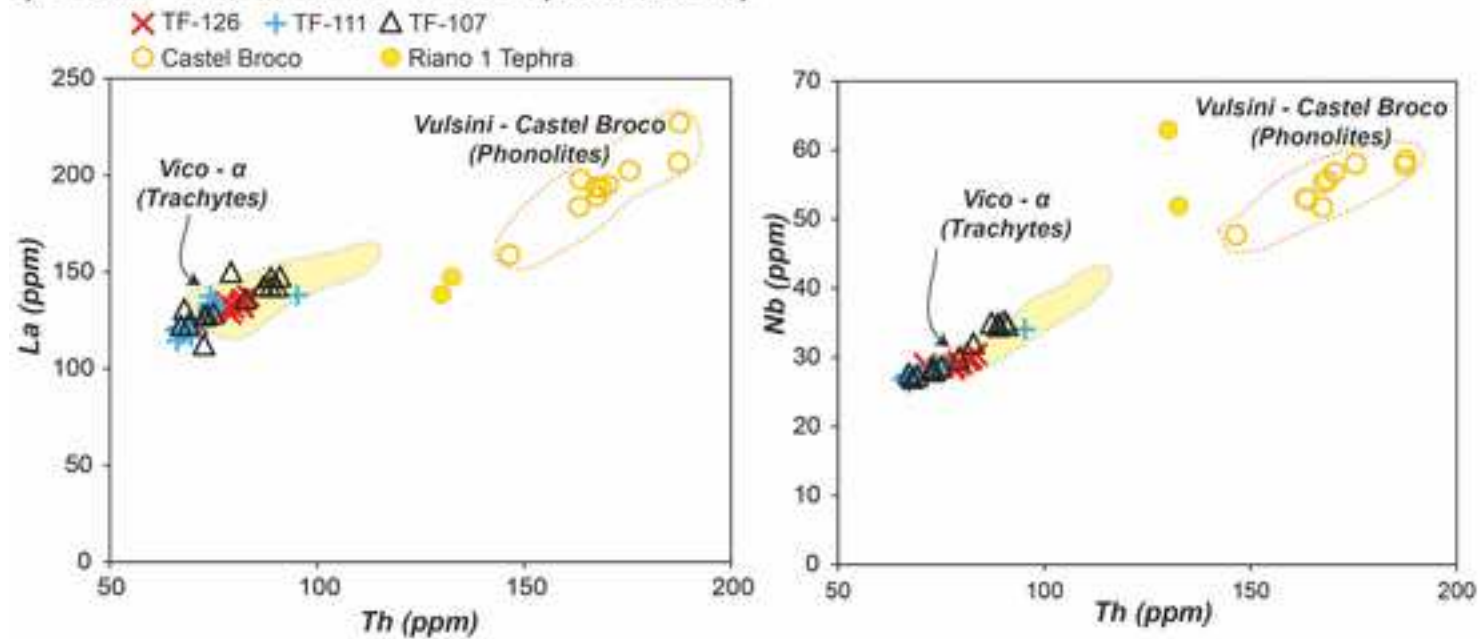
d) Vico γ (>399.7±3.0, < 406.2±2.0 ka)



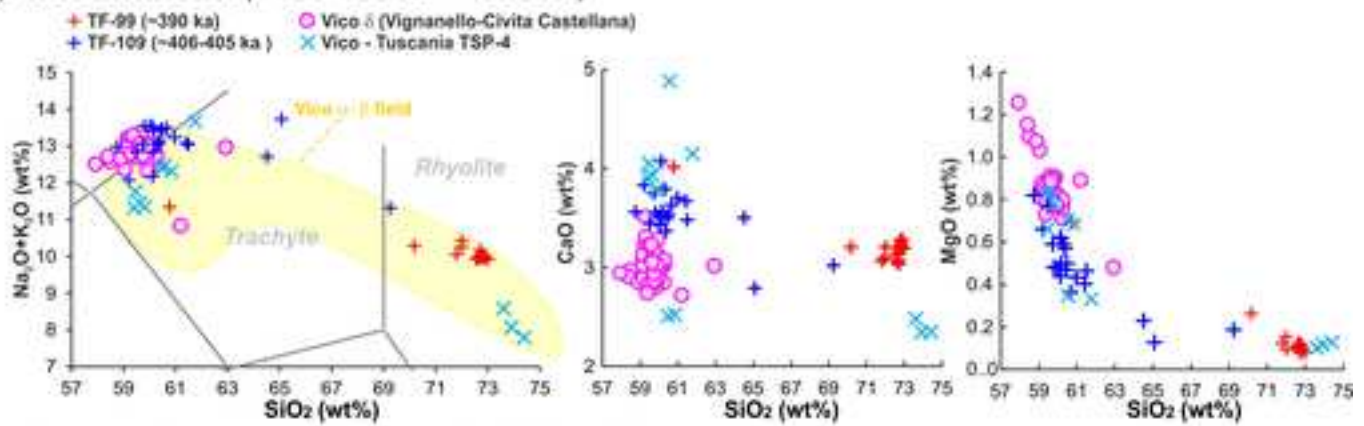
a) *Vico* α (414.8 ± 2.2 ka)



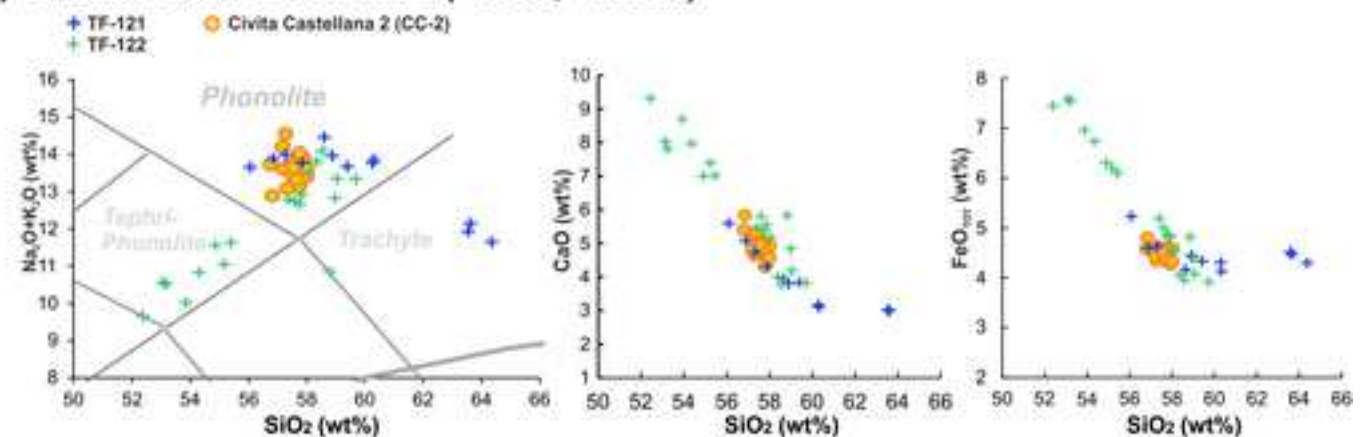
b) *Vulsini - Castel Broco - Riano 1* (404.7 ± 5.0 ka)



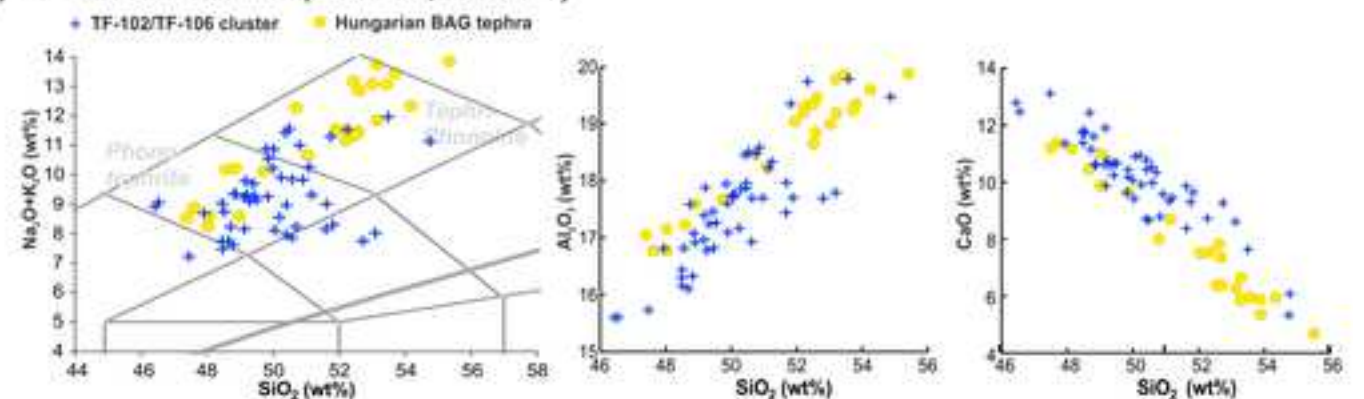
a) Vico unknown (~406-405 ka - ~390 ka)



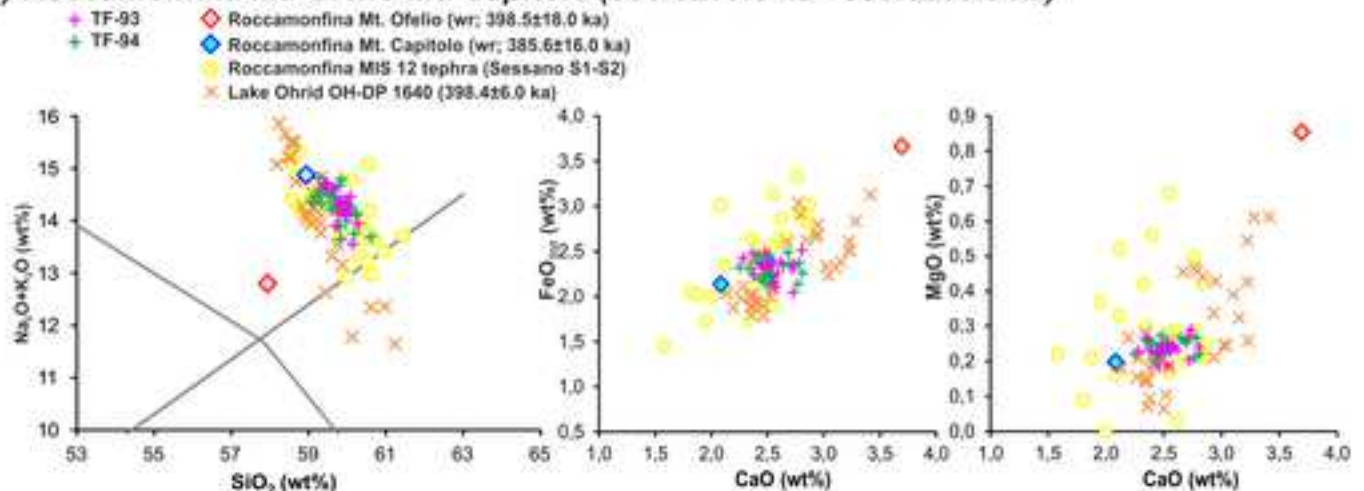
b) Sabatini Civita Castellana 2 (>408.5, <415 ka)



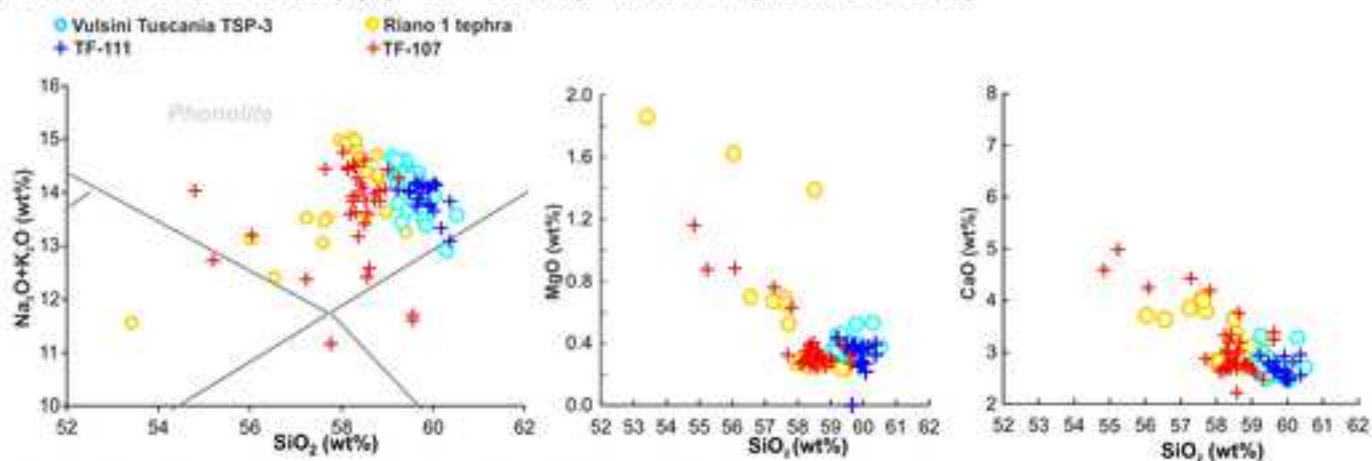
c) Sabatini unknown (>390 ka, <405 ka)



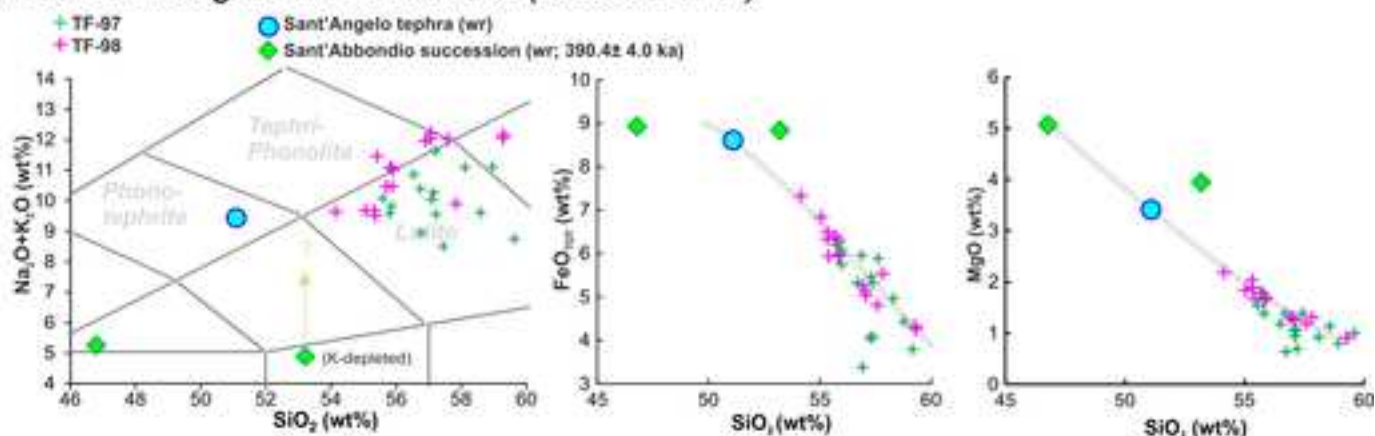
d) Roccamonfina Mt. Ofelio-Mt. Capitolo (398.5±18.0 ka - 385.6±16.0 ka)



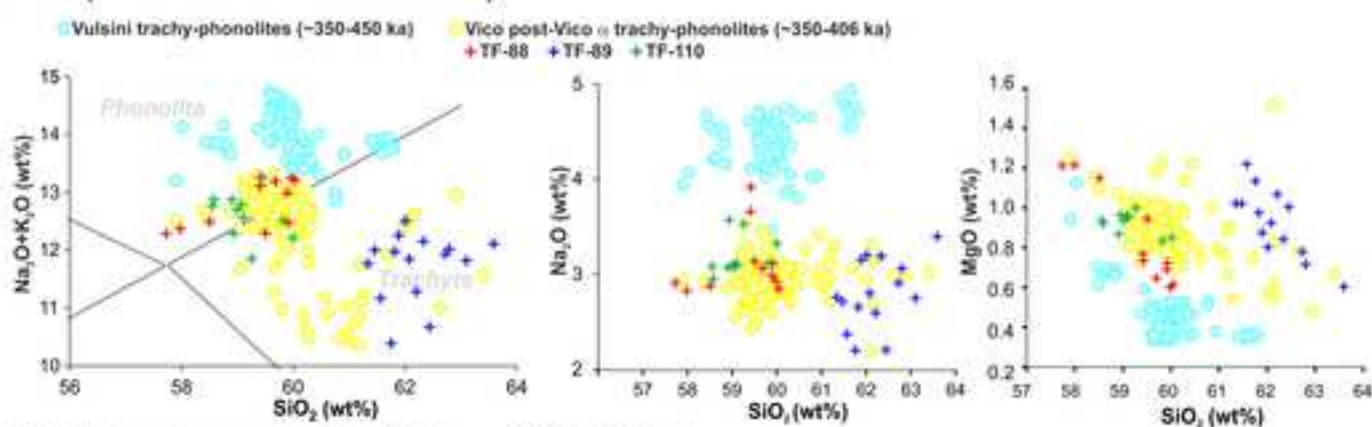
a) Vulsini Pumice Fall 0(?) (~405-406 ka) - Riano 1 (404.7±5.0 ka)



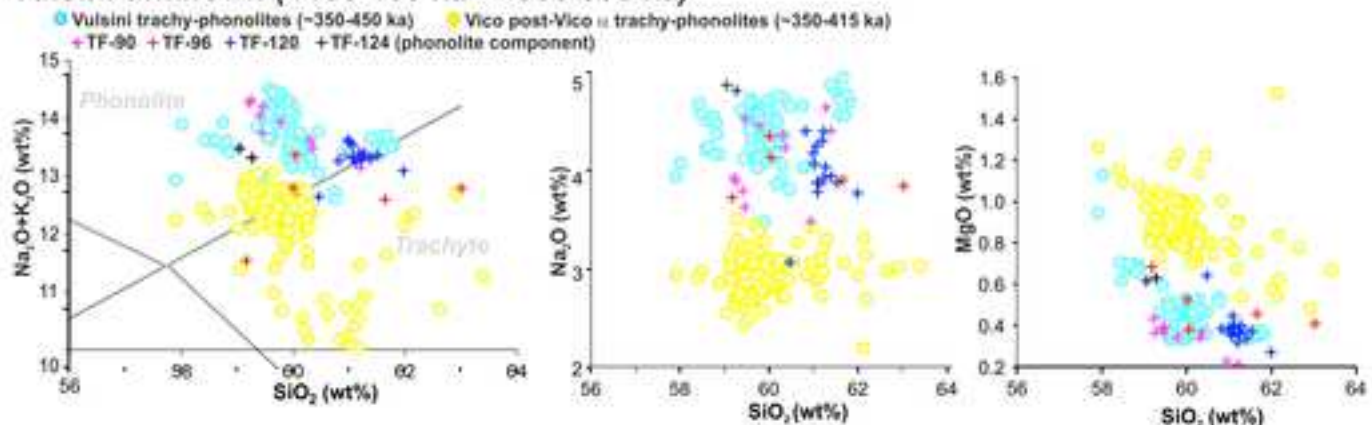
b) Vico Sant'Angelo-Sant'Abbondio (390.4±4.0 ka)

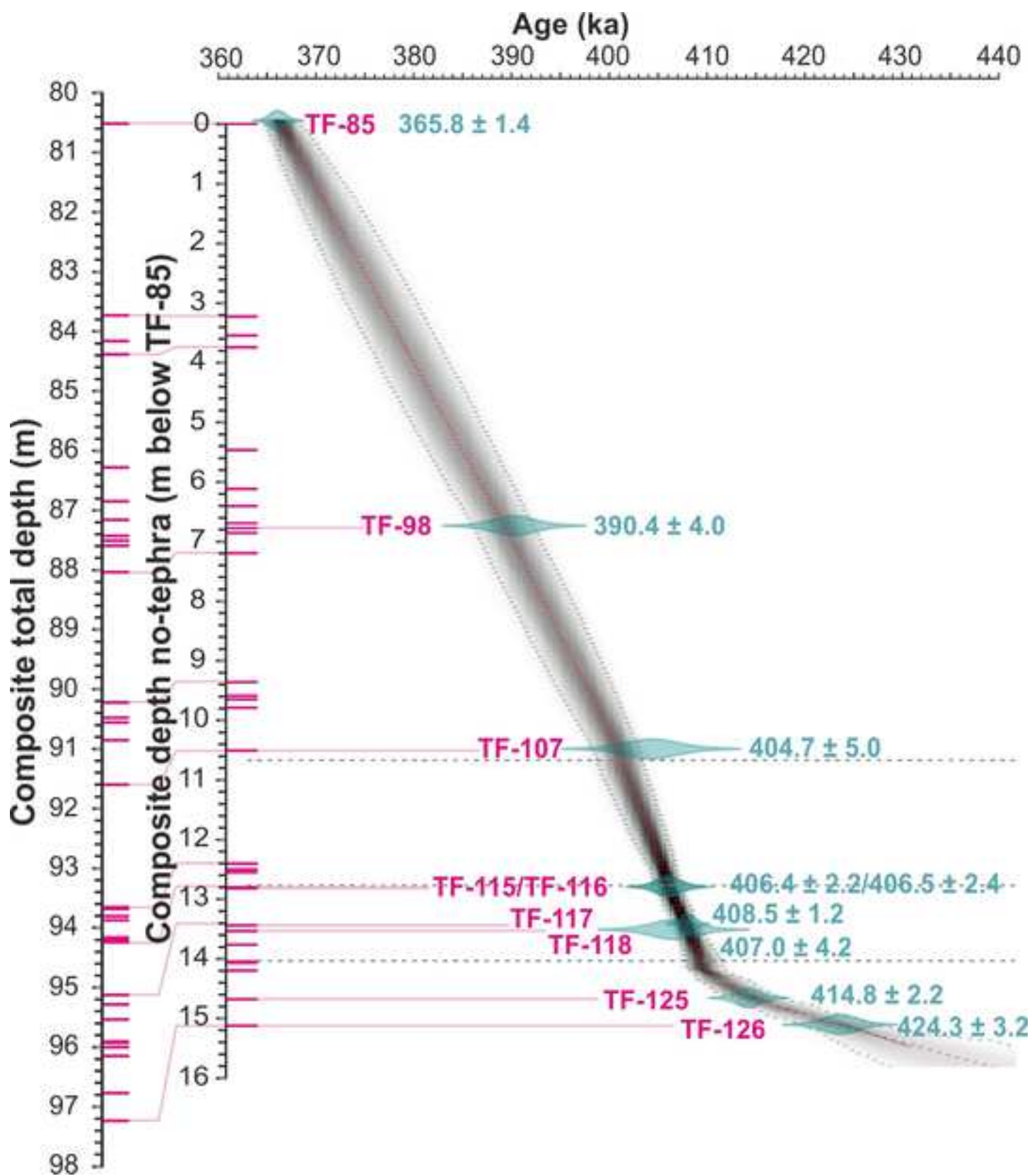


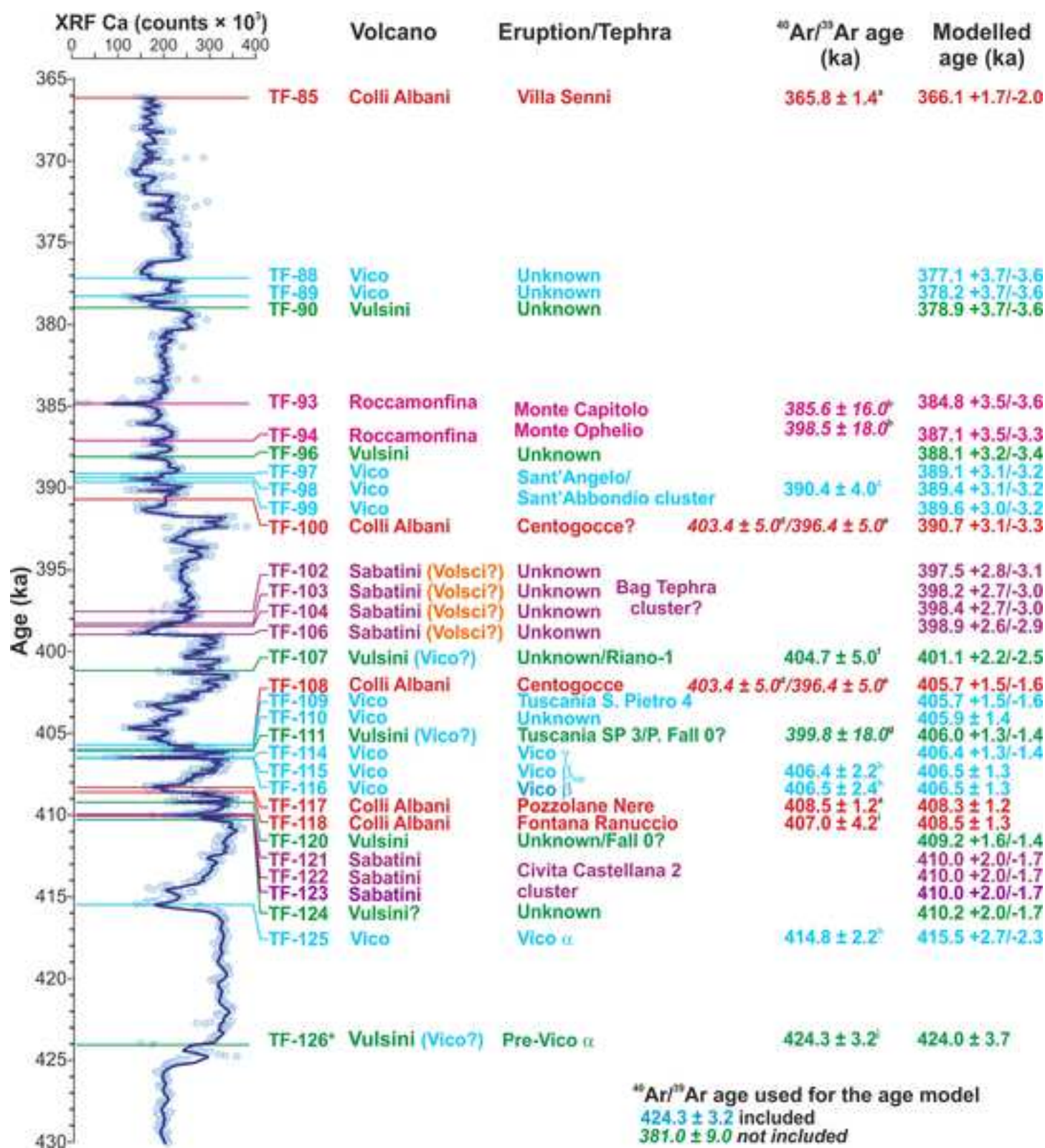
c) Vico (~415-408 ka - ~366-390 ka)

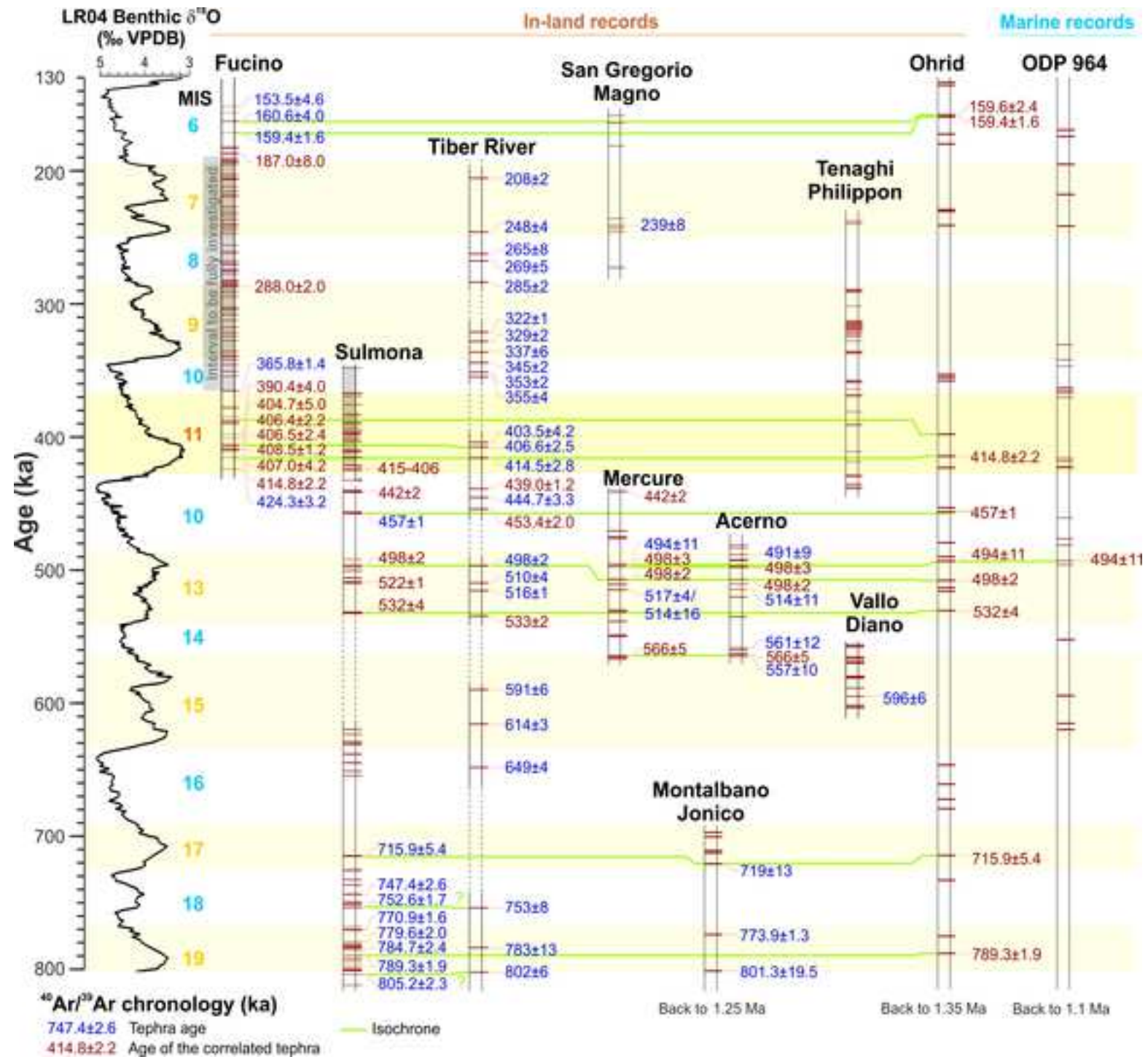


d) Vulsini unknown (~406-405 ka - ~366-390 ka)









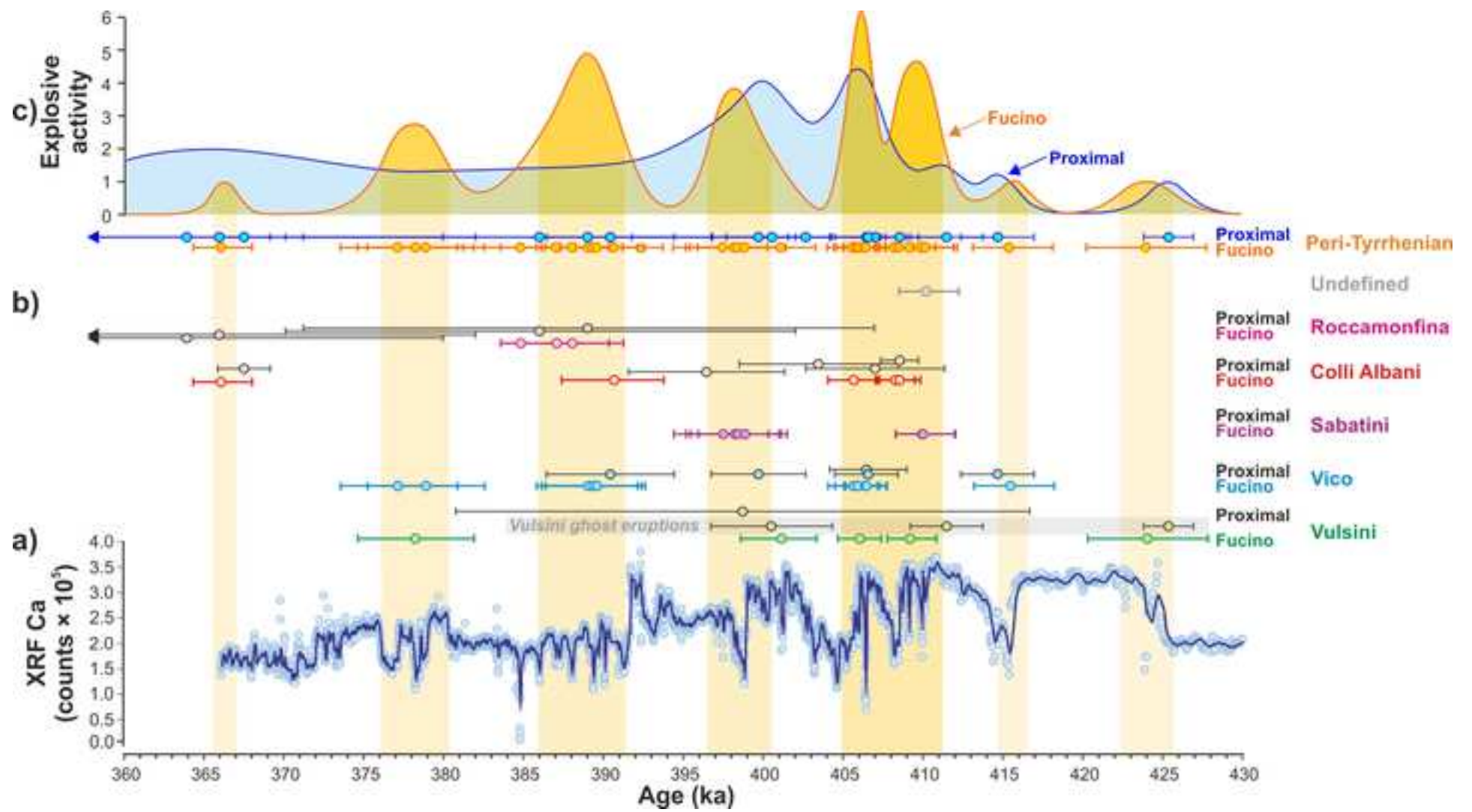


Table 1. Data acquired in this study and available from literature for each investigated Fucino tephra or proximal volcanic unit.

Tephra	Site/Section	Type of analysis			
		Glass-WDS (EMPA)	Trace elements (LA-ICP-MS)	Sr isotopes (TIMS)	⁴⁰ Ar/ ³⁹ Ar
TF-85	F4-F5	Yes ^a	No	Yes ^b	Yes ^b
TF-88	F4-F5	Yes ^b	No	No	No
TF-89	F4-F5	Yes ^b	No	No	No
TF-90	F4-F5	Yes ^b	No	No	No
TF-93	F4-F5	Yes ^b	No	No	No
TF-94	F4-F5	Yes ^b	No	No	No
TF-96	F4-F5	Yes ^b	No	No	No
TF-97	F4-F5	Yes ^b	No	No	No
TF-98	F4-F5	Yes ^b	No	No	No
TF-99	F4-F5	Yes ^b	No	No	No
TF-100	F4-F5	Yes ^b	No	No	No
TF-102	F4-F5	Yes ^b	No	No	No
TF-103	F4-F5	Yes ^b	No	No	No
TF-104	F4-F5	Yes ^b	No	No	No
TF-106	F4-F5	Yes ^b	No	No	No
TF-107	F4-F5	Yes ^b	Yes ^b	Yes ^b	No
TF-108	F4-F5	Yes ^b	No	No	No
TF-109	F4-F5	Yes ^b	No	No	No
TF-110	F4-F5	Yes ^b	No	No	No
TF-111	F4-F5	Yes ^b	Yes ^b	Yes ^b	No
TF-114	F4-F5	Yes ^b	No	No	No
TF-115	F4-F5	Yes ^b	No	No	No
TF-116	F4-F5	Yes ^a	Yes ^b	No	No
TF-117	F4-F5	Yes ^a	No	No	Yes ^b
TF-118	F4-F5	Yes ^b	No	No	No
TF-120	F4-F5	Yes ^b	No	No	No
TF-121	F4-F5	Yes ^b	No	No	No
TF-122	F4-F5	Yes ^b	No	No	No
TF-123	F4-F5	Yes ^b	No	No	No
TF-124	F4-F5	Yes ^b	No	No	No
TF-125	F4-F5	Yes ^b	Yes ^b	No	No
TF-126	F4-F5	Yes ^a	Yes ^b	Yes ^b	Yes ^a
Casale delle Piane	Tuscania	Yes ^b	No	No	No
Castel Broco	Tuscania	Yes ^a	Yes ^b	Yes ^b	No
Vico α (TSP-1)	Tuscania	Yes ^b	No	No	No
TSP-2	Tuscania	Yes ^b	No	No	No
TSP-3	Tuscania	Yes ^b	No	Yes ^b	No
TSP-4	Tuscania	Yes ^b	No	No	No
Riano R-1	Riano	Yes ^b	Yes ^b	Yes ^b	Yes ^c
Pozzolane Nere	Rome	Yes ^d	No	Yes ^f	Yes ^b
Vico β	Vignanello	Yes ^e	Yes ^b	No	Yes ^e
Vico α type locality	Viterbo	Yes ^e	Yes ^b	No	Yes ^e

^a Giaccio et al. (2019); ^b This study; ^c Marra et al. (2018); ^d Marra et al. (2009); ^e Pereira et al. (2020); ^f Gaeta et al. (2006).

Table 2. Comparison between the measured and recommended values of secondary standards employed in this study (Kakanui Augite, Rhyolite RLS132, USGS, MPI-DING glass standards of Jochum et al., 2006, and Lipari obsidian ID3506, Kuehn et al., 2011).

Standard		Lipari (ID3506, Kuehn et al., 2011)											
Oxide	SiO ₂	TiO ₂	Al ₂ O ₃	FeO _{TOT}	MnO	MgO	CaO	Na ₂ O	K ₂ O	P ₂ O ₅	F	Cl	SO ₂
Recommended values	74.94	0.07	13.25	1.57	0.07	0.04	0.74	4.12	5.17	0.01	0.15	0.34	0.01
Measured (mean n 5)	75.43	0.07	12.83	1.61	0.06	0.04	0.75	3.99	5.20	0.01	0.11	0.33	0.01
s.d.	0.47	0.00	-0.43	0.04	0.00	0.00	0.01	-0.13	0.03	0.00	-0.04	-0.02	0.00
Difference %	0.63	-0.36	-3.21	2.86	-2.55	-10.48	1.88	-3.16	0.55	23.51	-27.51	-5.11	-20.51
Standard		ATHO-G (Jochum et al., 2006)											
Oxide	SiO ₂	TiO ₂	Al ₂ O ₃	FeOT	MnO	MgO	CaO	Na ₂ O	K ₂ O	P ₂ O ₅	F	Cl	SO ₂
Recommended values	75.79	0.26	12.23	3.28	0.11	0.10	1.70	3.76	2.65	0.03		0.04	
Measured (mean n. 10)	76.20	0.25	11.89	3.28	0.12	0.10	1.79	3.64	2.70	0.02	0.10	0.04	0.01
s.d.	0.31	0.02	0.13	0.13	0.04	0.01	0.05	0.09	0.07	0.02	0.10	0.01	0.01
Difference %	0.44	-2.27	-2.84	-0.05	13.15	-2.48	4.86	-3.38	2.09	-5.46	-	-9.71	-
Standard		GOR128-G (Jochum et al., 2006)											
Oxide	SiO ₂	TiO ₂	Al ₂ O ₃	FeO _{TOT}	MnO	MgO	CaO	Na ₂ O	K ₂ O	P ₂ O ₅	F	Cl	SO ₂
Recommended values	46.49	0.29	9.99	9.89	0.18	26.22	6.29	0.58	0.04	0.03			
Measured (mean n. 9)	47.02	0.27	9.61	9.86	0.20	26.08	6.32	0.57	0.04	0.03	0.05	0.01	0.00
s.d.	0.57	0.02	0.10	0.33	0.04	0.26	0.09	0.02	0.01	0.03	0.09	0.01	0.01
Difference %	1.13	-6.51	-3.81	-0.30	10.02	-0.54	0.48	-2.21	4.93	25.85	-	-	-
Standard		StHs 6/80-G (Jochum et al., 2006)											
Oxide	SiO ₂	TiO ₂	Al ₂ O ₃	FeO _{TOT}	MnO	MgO	CaO	Na ₂ O	K ₂ O	P ₂ O ₅	F	Cl	SO ₂
Recommended values	63.83	0.70	17.84	4.38	0.08	1.97	5.29	4.45	1.29	0.16	0.03	0.02	
Measured (mean n. 9)	64.27	0.68	17.28	4.32	0.09	1.99	5.39	4.54	1.27	0.16	0.02	0.02	0.01
s.d.	0.46	0.03	0.09	0.18	0.04	0.03	0.10	0.14	0.04	0.03	0.03	0.01	0.01
Difference %	0.69	-3.11	-3.13	-1.45	21.11	0.89	1.84	2.12	-1.37	-2.88	-30.30	-2.26	
Standard		Kakanui Augite (USGS)											

Recommended values	50.56	0.84	8.30	6.52	0.13	16.31	16.03	1.30						
Measured (mean n. 5)	50.99	0.79	8.15	6.42	0.18	16.28	15.85	1.30	0.01	0.02	0.04	0.01	0.02	
sd	0.34	0.02	0.04	0.15	0.04	0.31	0.06	0.04	0.01	0.01	0.04	0.01	0.02	
Difference %	-0.43	0.05	0.15	0.11	-0.05	0.03	0.18	0.00	-0.01	-0.02	-0.04	-0.01	-0.02	
Standard	Rhyolite RLS132 (USGS)													
Recommended values	76.56	0.19	11.58	2.03	0.16	0.08	0.10	4.78	4.50					
Measured (mean n. 15)	76.95	0.19	11.20	2.12	0.15	0.05	0.11	4.70	4.50	0.02	0.18	0.20	0.02	
sd	0.25	0.02	0.13	0.07	0.02	0.02	0.02	0.19	0.06	0.01	0.11	0.02	0.02	
Difference %	0.52	0.64	-3.29	4.17	-5.52	-36.41	5.79	-1.82	-0.02					

Note: Here all values are reported at second decimal digits, but some errors (difference%) are calculated up to the fourth digits, especially for minor elements.

Table 3. Main lithological, mineralogical and geochemical features of the 365-430 ka F4-F5 Fucino tephra.

Tephra	Thickness (cm)	Composite depth (m)	Core section and depth (cm)	CG	Lithology			Rock type
					Juvenile clasts	Minerals	Lithic content	
TF-85*	13.25	80.520	F5-49 74-88	ND	Black-brown scoria	Lc>bmca>cpx	Poor	K-f
TF-88	1.25	83.770	F4-51 131-133/ F5-51 65-66	CG-2	White pumice and grey-brown scoria	Kfs>cpx>bmca	Poor	ph-tr
TF-89	2.00	84.168	F5-51 107-109	CG-2	Grey scoria	Kfs>cpx>bmca	Poor	ph
TF-90	2.00	84.388	F5-51 130-131	CG-2	Black-grey scoria	Kfs>cpx>bmca	Rich	tr
TF-93	0.50	86.140	F4-53 51.3-52.2/ F5-52 149-150	CG-2	White pumice	Kfs>cpx	No	tph-ph
TF-94	0.75	86.853	F4-53 53.6-54.6	CG-2	White pumice	Kfs	No	ph-tr
TF-96	2.00	87.166	F4-53 85-86.2	CG-2	White pumice and grey scoria	Kfs>cpx	Poor	ph
TF-97	2.50	87.470	F4-53 110-112	CG-2	Grey scoria	Kfs>bmca	Poor	lat
TF-98	1.00	87.575	F4-53 119-120	CG-2	Grey scoria and whitish pumice	Kfs>bmca	Poor	lat-tph-ph-tr
TF-99	1.00	87.677	F4-53 128-129	CG-3	Highly vesicular white pumice and brown scoria	Kfs>bmca	Poor	K-tr-rhy
TF-100	6.75	88.045	F5-54 0-4.5	CG-1	Dense black scoria	Lc	Poor	K-f
TF-102	2.00	90.230	F4-55 58-60/ F5-54 125-126	CG-2	Poorly vesicular black scoria	Kfs>Lc>bmca	Poor	t-pht
TF-103	3.00	90.485	F4-55 83-86/ F5-54 133-134.2	CG-2	Poorly vesicular black scoria	Kfs>Lc>bmca	Poor	pht-tph
TF-104	1.25	90.560	F4-55 92-93/ F5-54 142-144	CG-2	Poorly vesicular grey scoria	Kfs>Lc>bmca	Poor	pht-tph
TF-106	1.25	90.860	F4-55 123-124.4	CG-2	Poorly vesicular grey scoria	Kfs>Lc>bmca	Rich	trb-pht-tph-sho
TF-107	2.00	91.620	F4-56 29-31/ F5-55 57.2-59	CG-2	Moderately vesicular whitish pumice and poorly vesicular greyish scoria	Kfs>bmca>cpx	Rich	ph-tr
TF-108	2.75	93.650	F5-56 110-113	CG-1	Dense, leucite-bearing black scoria	Lc	No	K-f
TF-109	2.00	93.690	F5-56 114-117	CG-3	Highly vesicular white pumice and greyish scoria	Kfs>bmca	Poor	K-ph-tr-rhy
TF-110	2.00	93.810	F5-56 126-128	CG-2	Highly vesicular white pumice and greyish scoria	Kfs>bmca	Poor	ph-tr
TF-111	1.50	93.885	F4-57 47-50	CG-2	Highly vesicular white pumice	Kfs>bmca	Very poor	ph-tr
TF-114	2.00	94.166	F4-57 77-79	CG-3	Highly vesicular white pumice and greyish scoria	Kfs>bmca>cpx	Poor	K-tr-rhy
TF-115	2.00	94.211	F4-57 81-83	CG-3	Highly vesicular white pumice	Kfs>bmca>cpx	Poor	K-tr-rhy
TF-116	2.50	94.251	F4-57 85-87	CG-3	Highly vesicular white pumice	Kfs>bmca>cpx	Poor	K-ph-tr-rhy
TF-117*	9.00	95.130	F4-57 151-152/ F5-57 0-7	ND	Poorly vesicular leucite-bearing black scoria	Lc>cpx	Poor	K-f
TF-118*	5.50	95.290	F5-57 16-23	ND	Poorly vesicular leucite-bearing black scoria	Lc	Poor	K-f
TF-120	2.00	95.540	F5-57 45-47	CG-2	Highly vesicular white pumice	Kfs>bmca	Very poor	ph-tr
TF-121	8.00	95.910	F5-57 77-85	CG-2	Poorly vesicular greyish-brownish scoria	bmca>Kfs>Lc	Poor	tph-ph-tr
TF-122	1.00	95.930	F5-57 85-86	CG-2	Dense, leucite-bearing brown scoria	Kfs>bmca>Lc	Poor	tph-ph-lat-tr
TF-123	5.50	96.005	F5-57 87-94	CG-2	Poorly vesicular black scoria	Lc>cpx>Kfs>bmca	Very rich	pht-tph
TF-124	0.75	96.155	F5-57 107-110	CG-2	Poorly vesicular black scoria and whitish pumice	Lc>cpx>bmca	Rich	sho
TF-125	3.50	96.775	F5-58 12-19.5	CG-3	Highly vesicular white pumice	Kfs>bmca>cpx>op	Poor	K-ph-tr-rhy
TF-126*	2.00	97.250	F5-58 64-66	ND	Highly vesicular white (base) and honey (top) pumice	Kfs>bmca>cpx>op	Poor	ph-tr

*=EPMA data in [Giaccio et al. \(2019\)](#); ND=Not determined in this study. Rock type abbreviations: K- = potassium- (suffix); f = foidite; ph = phonolite; tr = trachyte; tph = tephriphonolite; lat = latite; rhy = rhyolite. Mineral abbreviations: Kfs = K-feldspar; bmca = black mica; cpx = clinopyroxene; Lc = leucite; op = opaques. CG = compositional group (see [Fig. 6](#)).

Table 4. Geochemical and mineralogical data summary of the investigated proximal units.

Outcrop/ Location	Coordinates	Unit	Volcanic source	Lithology		Rock type
				Juvenile clasts	Minerals	
Tuscania- San Pietro	42° 24' 43.32" N – 11° 52' 45.13" E	Casale delle Piane	Vulsini	Highly vesicular dark grey, Kfs+bmca-bearing scoria	Kfs>bmca	Ph
		Vico α	Vico	Highly vesicular white, Kfs+bmca- bearing pumice and grey scoria	Kfs>bmca>cpx	K-tr-rhy
		TSP-2	Vulsini	Moderately vesicular grey Kfs- bearing pumice	Kfs>cpx	Ph
		TSP-3 (PF-0?)	Vulsini	Highly vesicular white, Kfs+bmca- bearing pumice	Kfs>bmca>cpx	Ph
		TSP-4	Vico	Reddish (thermally altered) Kfs- bearing pumice	Kfs>cpx	K-tr-rhy
Riano	42° 05' 24.06" N – 12° 31' 57.43" E	Riano R-1	ND (<i>Sabatini?</i>)	Blackish ash	Kfs>cpx>lc	Ph-tph-lat
Rome	41° 50' 44.74" N – 12° 28' 40.56" E	Pozzolane Nere	Colli Albani	Lc-bearing black scoria	Lc>cpx>bmca	K-f

ND=undetermined. Rock type abbreviations: K- = potassium- (suffix); f = foidite; ph = phonolite; tr = trachyte; tph = tephriphonolite; lat = latite; rhy = rhyolite. Mineral abbreviations: Kfs = K-feldspar; bmca = black mica; cpx = clinopyroxene; lc = leucite.

Table 5. $^{87}\text{Sr}/^{86}\text{Sr}$ ratio values of the selected four Fucino tephra and three proximal units.

Tephra/ sample	Setting	Volcano	Glass composition	Analysed material	$^{87}\text{Sr}/^{86}\text{Sr}$	2σ
TF-85	distal	Colli Albani	K-foidite	lc	0.710430	± 0.000007
TF-107	distal	Unknown	phonolite	fsp	0.710851	± 0.000006
TF-111	distal	Vulsini-Vico	phonolite	pum	0.709507	± 0.000006
				fsp	0.710671	± 0.000006
				cpx	0.710149	± 0.000007
TF-126	distal	Vulsini	phonolite	fsp	0.711105	± 0.000007
Castel Broco	proximal	Vulsini	phonolite	cpx	0.710960	± 0.000006
				fsp	0.710965	± 0.000006
TSP-3	proximal	Vulsini	phonolite	pum	0.711199	± 0.000007
				fsp	0.711245	± 0.000006
Riano R-1	mid- proximal	Vulsini	phonolite	K-fsp	0.710810	± 0.000007

Abbreviations: K-fsp=K-feldspar; fsp=feldspar; cpx=clinopyroxene; pum=pumice.

Table 6. Volcanic sources of the investigated Fucino tephra, inferred from glass chemical composition and lithological features.

Volcano	Fucino tephra
Vulsini	TF-107, TF-111
Vico	TF-99, TF-109, TF-114, TF-115, TF-116, TF-125
Vulsini or Vico	TF-88, TF-89, TF-90, TF-96, TF-97, TF-98, TF-110, TF-120, TF-124
Sabatini	TF-102, TF-103, TF-104, TF-106, TF-121, TF-122, TF-123
Colli Albani	TF-100, TF-108
Roccamonfina	TF-93, TF-94

Table 7. Summary of the literature geochronological data for the peri-Tyrrhenian potassic volcanism of central Italy during the MIS 11, or a slightly wider interval. When possible, i.e., if all the all the required analytical data were published, $^{40}\text{Ar}/^{39}\text{Ar}$ ages are recalculated relative to an age of 1.1891 Ma for the Alder Creek sanidine or relative to an age of 28.294 Ma for the Fish Canyon sanidine monitor standards (Niespolo et al., 2017), with the uncertainty expressed at 2σ .

Volcanic source	Volcanic phase	Unit/sample	Type of activity/product	K/Ar and $^{40}\text{Ar}/^{39}\text{Ar}$ age ($ka \pm 2\sigma$)	References									
Vulsini	Bolsena	Ponticello Pumices	Pumice fall	352.0 \pm 4.0	Nappi et al., 1995									
				345.4 \pm 2.1	Marra et al., 2020a									
	Vulsini Field	Fall 0	Pumice fall	Pumice fall	399.8 \pm 18.0	Turbeville, 1992								
					Castel Broco	Pumice fall-pyroclasti flow	n.d.	Marra et al., 2020a						
									Piano della Selva	Pyroclastic flow	n.d.			
												Indirect evidence from xenocrysts age populations	undefined	400.5 \pm 3.7
														411.4 \pm 2.4
425.4 \pm 1.6														
437.6 \pm 2.2														
Vico	Period I	SAAS-bottom	Pumice fall	390.4 \pm 4.0	Marra et al., 2014									
				VICO δ	Pumice fall	399.7 \pm 3.0	Pereira et al., 2020							
				VICO γ	Pumice fall	n.d.								
				VICO β_{top}	Pumice fall	406.4 \pm 2.0								
				VICO β	Pumice fall	406.5 \pm 2.4								
				VICO α	Pumice fall	414.8 \pm 2.2								
Sabatini	Southern Sabatini	CC-2	Pumice fall	n.d.	Pereira et al., 2020									
				La Rosta	Pumice fall	439.1 \pm 1.0	Marra et al., 2020b							
				FALL F	Pumice fall	448.5 \pm 7.0	Marra et al., 2014							
Colli Albani	Villa Senni Eruption Cycle	Madonna degli Angeli succession	Lava dyke	354.5 \pm 6.0	Gaeta et al., 2006 and references therein									
			Lava flow	357.5 \pm 9.0										
			Lava flow	359.5 \pm 6.0	Marra et al 2003									
			Lava flow	359.5 \pm 8.0										

	Pantano Secco hydromagmatic center	Scoria fall	367.6±2.0	
	Madonna degli Angeli succession	Scoria fall	368.6±2.0	
		Lava flow	369.6±3.0	
	Tufo Lionato	Pyroclastic flow	368.6±4.0	
Pozzolane Nere Eruption Cycle	Centogocce succession	Lava flow	396.0±5.0	
		Scoria fall	402.3±5.0	
	Pozzolane Nere	Pyroclastic flow	407±2.0	
Pozzolane Rosse Eruption Cycle	Corcolle succession	Lava flow	439.5±5.0	
		Scoria	440.5±3.0	
	Pozzolane Rosse	Pyroclastic flow	455.5±2.0	
	Vallerano Lava	Lava flow	458.0±8.0	
	Selva Piana	Lava	362.0±11.0	Boari et al., 2009
	Colle Avarone CA- CGT	Reworked volcanic horizon	360.8±6.5	Marra et al., 2021
	Isoletta III	Scoria fall	363.8±8.0	
	Isoletta II	Scoria fall	373.7±4.0	Pereira et al., 2018
	Valcatora	Lava dyke	379.0±8.0	Boari et al., 2009
	Lademagne II	Reworked volcanic horizon	387.7±5.0	Pereira et al., 2018
	Pofi-Colle La Grotta	Phreatomagmatic deposit	391.5±3.6	Marra et al., 2021
	Giuliano di Roma	Lava	394.6±6.0	Boari et al., 2009
	Pofi Scoria cone	Scoria fall	394.4±3.5	Marra et al., 2021
	Cava Pompei	Scoria fall	392.7±3.0	Pereira et al., 2018
	Arnara Scoria cone	Scoria fall	395.8±6.1	Marra et al., 2021
	Isoletta I	Scoria fall	401.7±3.0	
	Lademagne I	Scoria fall	404.0±5.0	Pereira et al., 2018
	Supino	Phreatomagmatic deposit	407.7±2.6	Marra et al., 2021

Volsci volcanic
field

Roccamonfina	Rio Rava-Brown Leucitic Tuff stage	La Tomacella, upper	Pyroclastic rock	410.0±10.0	Boari et al., 2009
		Tecchiena	Lava	416.1±11.0	Boari et al., 2009
		Celleta	Lava	417.1±6.0	
		La Tomacella, lower	Pyroclastic rock	425.2±13.0	Scaillet et al., 2008
		Brown Leucitic Tuff	Pyroclastic flow	343.6±6.0	
				358.2±10.0	Rouchon et al., 2008
				385.0±23.0	Luhr and Giannetti, 1987
		Scipicciano 89X	Lava flow	361.7±10.0	Rouchon et al., 2008
		Fontana-radina RMF7	Lava flow	363.7±16.0	
		SP/R-30	Lava dome	360.0±42.0 (GM)	Giannetti, 2001
				382.0±3.0 (San)	
				390.0±30.0 (San)	
		SP/R-31	Effusive	370.8±3.0	Rouchon et al., 2008
		La Frascara RMF4	Lava flow	373.9±18.0	
		Galluccio RMF3	Lava flow	375.9±16.0	
		Monte Casi	Lava dome	370.0±9.0	Radicati di Brozolo et al., 1988
		LP/R-247	Effusive	378.9±4.0 (San)	Giannetti, 2001
				399.3±12.0 (San)	
				430.0±6.0 (GM)	
		MLT/R-352	Lava flow	374.0±11.0	Rouchon et al., 2008
MLP/R-69	Lava dome	376.0±16.0			
Monte Capitolo RMF6	Pyroclastic	396.2±16.0	Rouchon et al., 2008		
Masseria Robetti	Lava flow	397.0±18.0	Radicati di Brozolo et al., 1988		
MLT/R-290	Lava flow	408.4±9.0	Giannetti, 2001		

Monte Ofelio RMF12	Pyroclastic	409.4±18.0	Rouchon et al., 2008
MLT/R-351	Lava flow	409.4±10.0	Giannetti, 2001
LP/R-104	Lava dome	415.5±18.0	
LP/R-104	Lava dome	416.6±32.0	Radicati di Brozolo et al., 1988
Masseria Robetti	Undefined	421.0±9.0	
LP/T-247	Lava dome	430.0±6.0	Giannetti, 2001
Rio Rava RMF14	Lava flow	446.0±12.0	Rouchon et al., 2008

GM, groundmass; San, sanidine.

Declaration of interests

The authors declare that they have no known competing financial interests or personal relationships that could have appeared to influence the work reported in this paper.

The authors declare the following financial interests/personal relationships which may be considered as potential competing interests:

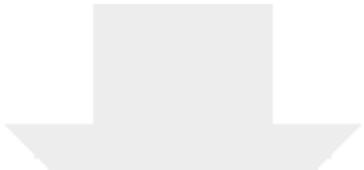


Click here to access/download
Supplementary Material
SD-1_major elements.xlsx





Click here to access/download
Supplementary Material
SD-2_trace elements.xlsx



Click here to access/download
Supplementary Material
SD-3_40Ar_39Ar.pdf

